NTNU
Norwegian University of
Science and Technology

Master's thesis

2019

Anne Hamarsnes

Master's thesis

NTNU
Norwegian University of
Science and Technology
Faculty of Engineering
Department of Mechanical and Industrial Engineering

Anne Hamarsnes

Mechanical Properties of a Welded 6082 Aluminium Alloy with Local Heat Treatments

June 2019

NTNU
Norwegian University of
Science and Technology

NTNU
Norwegian University of
Science and Technology

Mechanical Properties of a Welded 6082 Aluminium Alloy with Local Heat Treatments

Anne Hamarsnes

Mechanical Engineering
Submission date: June 2019
Supervisor: Geir Ringen
Co-supervisor: Trond Furu

Norwegian University of Science and Technology
Department of Mechanical and Industrial Engineering

Preface and Acknowledgements

This master's thesis is written during the spring semester of 2019 as part of the MSc degree in Mechanical Engineering at the Norwegian University of Science and Technology (NTNU) in Trondheim. The project is linked to the NTNU Aluminium Product Innovation Center (NAPIC) and Norsk Hydro together with SINTEF Manufacturing and the Institute for Energy Technology (IFE). The work is a continuation of the specialization project "Mechanical Properties of Welded 6082-T6 Aluminium Alloy with Transverse Cross Welds" carried out during the autumn of 2018, and parts of the theoretical background are reused in this present thesis.

I want to thank my supervisor, Professor Geir Ringen[1], for his guidance and support through the writing of this report. I would also like to thank my co-supervisor Dr. Trond Furu[2] and Dr. Ole Runar Myhr[3] for their encouragement and helpful feedback during this semester. I appreciate the help from Senior Research Scientist Rune Østhus[4] during my visit to SINTEF Manufacturing and throughout this semester.

Anne Hamarsnes
Trondheim, June 2019

---

[1] NTNU, Trondheim
[2] Norsk Hydro, Sunndalsøra
[3] Norsk Hydro, Raufoss
[4] SINTEF Manufacturing, Raufoss

Abstract

This paper investigates three different local heat treatments in combination with an aging process referred to as post weld heat treatment (PWHT) for improving the strength and ductility of welded 6082-T6 aluminium. The three methods aim to manipulate the geometry of the heat affected zone (HAZ) and involves heat introduced locally by cross welds perpendicular to the joining weld, longitudinal laser parallel to the weld and a laser pattern of many short laser lines. The experimental work involves microstructural examination of the weld, extensive hardness testing, and tensile testing using digital image correlation (DIC). Lastly, predictive models are used to predict the temperature response and resulting hardness due to the thermal cycles of welding and laser treatment.

The PWHT increases the strength significantly, and both strength and ductility are affected by the local heat treatments. Cross welds show the most promising results, where all specimens show significant improvements in ductility and an increase in ultimate tensile strength of more than 10 MPa. In combination with PWHT, the cross welds increase the ultimate tensile strength by 47 MPa, and the fracture strain is improved by 120%. The HAZ geometry is highly affected by the cross welds, causing strain to localize at several locations. The longitudinal laser indicates a small increase in strength and ductility, depending on laser powers, and further investigation of this method is required to conclude on the effects. The laser pattern changes the strain distribution and improves ductility slightly, but the laser power is likely too low to increase global strength significantly. Predictions of the peak temperatures are considered adequate, and the hardness predictions show good correspondence with the measured data and estimate the width of the HAZ remarkably precisely.

Sammendrag

Denne oppgaven undersøker tre ulike lokale varmebehandlinger i kombinasjon med en utherdingsprosess etter sveising for å forbedre styrken og duktiliteten til sveiset 6082-T6 aluminium. De tre metodene skal manipulere geometrien til den varmebehandlede sonen og involverer varme introdusert lokalt ved sveiser på tvers av sammenføyningssveisen, langsgående laserlinjer parallelt med sveisen og et lasermønster av mange korte laserlinjer. Det eksperimentelle arbeidet involverer en mikrostrukturanalyse av sveisen, omfattende hardhetstesting, samt strekktesting ved hjelp av DIC-analyse (eng: digital image correlation). Til slutt brukes prediktive modeller til å forutsi temperaturfordelingen og resulterende hardhet som følge av termiske sykluser fra sveising og laserbehandling.

Utherdingsprosessen etter sveising øker styrken betydelig, og både styrke og duktilitet er påvirket av de lokale varmebehandlingene. Tverrsveisene viser mest lovende resultater, hvor alle prøvene viser signifikante forbedringer i duktilitet og en økning i maksimal strekkstyrke på mer enn 10 MPa. I kombinasjon med utherdingen, fører tverrsveisene til en økning på opptil 47 MPa i strekkfasthet, samt en 120 % økning i tøyning ved brudd. Geometrien til den varmepåvirkede sonen er sterkt påvirket av tverrsveisene, noe som gjør at tøyningslokaliseringer oppstår flere steder. Behandlingen med langsgående laser indikerer en liten økning i styrke og duktilitet, avhengig av laserkraften, og det er nødvendig med nærmere undersøkelser av denne metoden. Lasermønsteret endrer tøyningsfordelingen og forbedrer duktiliteten noe, men lasereffekten er sannsynligvis for lav til å gi en betydelig økning i global styrke. Estimeringen av maksimal temperatur anses å være tilstrekkelig, og de simulerte hardhetsverdiene viser god overensstemmelse med de målte dataene og klarer å forutse rekkevidden av varmepåvirket sone veldig nøyaktig.

Contents

Preface and Acknowledgements **i**

Abstract **iii**

Sammendrag **v**

List of Figures **x**

List of Tables **xv**

Abbreviations **xvi**

1 Introduction **1**

1.1 Background and motivation 1

1.2 Objective and scope 2

2 Theory **3**

2.1 Al-Mg-Si Alloys 3

2.1.1 Main alloying elements 3

2.1.2 Thermal history of extruded Al-Mg-Si alloy 4

2.1.3 Precipitation hardening 5

2.1.4 Strengthening mechanisms 6

2.2 Welding of Al-Mg-Si Alloys 8

2.2.1 Gas metal arc welding (GMAW) process 8

2.2.2 The thermal cycle of welding 9

2.3 Softening in the heat affected zone (HAZ) 12

2.3.1 Weld zones 12

2.3.2 Softening causes 13

2.3.3 Post weld heat treatment (PWHT) 14

2.4 Modification of HAZ geometry 15

2.4.1 General concept 15

2.4.2 With welds 15

2.4.3 With laser 16

2.5 Load bearing capacity 17

2.6 Modelling and prediction of properties 18

3 Experimental **21**

3.1 Base material 21

3.2 Specimen preparation 22

3.2.1 Preparation process 22

3.2.2 Welding GMAW of sheets 22

3.2.3 Post weld heat treatment (PWHT) 23

3.2.4 Local heat treatment by cross welds 23

3.2.5 Local heat treatment by longitudinal laser 25

3.2.6 Local heat treatment by laser pattern 26

3.3 Sample preparation, examination and testing 27

3.3.1 Optical microscopy 27
3.3.2 Hardness testing 28
3.3.3 Tensile testing 28
3.3.4 Tensile testing with DIC 29
3.4 Predictions and simulations 30
3.4.1 Temperature calculations 30
3.4.2 Prediction of hardness 31
4 Results **33**
4.1 Characterization of the weld 33
4.1.1 Microstructure 33
4.1.2 Hardness profiles 34
4.2 DIC tensile test results of cross welded specimens 35
4.2.1 Stress-strain behavior 35
4.2.2 Reference specimens 37
4.2.3 Cross weld speed 18 mm/s 38
4.2.4 Cross weld speed 20 mm/s 39
4.2.5 Cross weld speed 22 mm/s 40
4.2.6 Cross weld speed 26 mm/s 42
4.3 Results of longitudinal laser 43
4.3.1 Hardness profiles 43
4.3.2 Tensile test results 46
4.4 Results of laser pattern 49
4.4.1 Hardness profiles 49
4.4.2 DIC tensile test results 50
4.5 Predictions and simulations 52
4.5.1 Thermal cycle of welding 52
4.5.2 Hardness profiles predicted by NaMo 53
5 Discussion **55**
5.1 Introductory remarks 55
5.2 Mechanical properties of the weld 55
5.2.1 Degradation of properties in the HAZ 55
5.2.2 Strength of reference specimens 55
5.3 Effect of local heat treatments 56
5.3.1 Cross welds 56
5.3.2 Longitudinal laser 60
5.3.3 Laser pattern 61
5.4 Predictions and simulations 62
5.4.1 Validation of peak temperature predictions and thermal cycles 62
5.4.2 Evaluation of hardness predictions 64
6 Conclusion **67**

6.1 Summary and conclusions 67
6.2 Recommendations for further work 68

References 69

Appendices I

A Finite element analysis (FEA) results I

B Material certificate II

C Tensile test specimens III

D NaMo inputs IV

E Temperature calculations and corresponding NaMo output VI

F Stress-strain plot of all DIC tensile specimens VII

G Fractured DIC tensile specimens VIII

H Longitudinal laser in HAZ XI

H.1 Tensile results XI
H.2 Fractured tensile specimens XI

I Risk assessment XII

List of Figures

2.1 Equilibrium solid solubility of different alloying elements as a function of temperature. Copied from [1]. 4
2.2 The thermal history of extruded aluminium profiles, including estimated levels of Mg and Si in solid solution from [16]. 4
2.3 Illustration of common flow pattern during extrusion of metals. Copied from [1]. 5
2.4 Schematic illustration of the strength development during artificial and natural aging of Al-Mg-Si alloys (W: solution heat-treated condition; T6: peak-aged condition; O: fully annealed condition; T4: naturally aged condition). Copied from [19] 6
2.5 Illustration showing the strengthening contributions of solid solution hardening, σ_{ss} and precipitation hardening, σ_p. Copied from [23] . . 7
2.6 Illustration of the GMAW process with basic features such as the electrode, arc and shielding gas indicated. Copied from [26]. 8
2.7 Schematic representation of Rosenthal thick plate solution showing a moving point source. Copied from [27]. 9
2.8 Schematic representation of Rosenthal thin plate solution showing a moving line source on a thin sheet. Copied from [27]. 10
2.9 The real and imaginary point sources on a plate of finite thickness, d, assumed for the Rosenthal medium thick plate solution. Copied from [27]. 11
2.10 Measured thermal cycles during welding of aluminium compared to weld thermal cycle predicted by the medium thick plate solution for fixed peak temperatures. Copied from [27] 12
2.11 Illustration showing the resulting zones in the cross-section of Al–Mg–Si alloy fusion welds. The outer boundary of the HAZ is indicated by the grey lines. 13
2.12 Illustration showing the evolution of the microstructure during artificial aging (AA) (a), welding (W) (b) and post weld heat treatment (PWHT) (c) of Al–Mg–Si alloys. The outer boundary of the HAZ is indicated by the semicircles in the diagrams. Copied from [29] . . 13
2.13 Hardness distribution after welding (a) following dissolution of $\beta''(Mg_2Si)$ particles and (b) after prolonged natural aging. Copied from [7]. . . 14
2.14 Finite element analysis of the modified HAZ geometry showing plastic strain of (a) bulged HAZ and (b) straight HAZ. Copied from [30]. 16
2.15 Illustration of loading conditions perpendicular to the weld. Copied from [9]. 18
3.1 Illustration showing the process of cutting, welding and application of local heat treatments. 22
3.2 The pattern of the applied GMA cross welds. 24
3.3 Illustration showing the process of applying the cross welds and PWHT. 24

3.4 Illustration showing the position of the longitudinal laser treatment, indicated by blue lines. The laser treatment was applied to both surfaces of the sheet. 25
3.5 Illustration showing where the specimens for hardness and tensile testing were extracted. (a) shows the reference specimens and (b) shows the specimens with longitudinal laser treatment indicated by blue lines. 25
3.6 Illustration showing the pattern of the laser treatment indicated by blue lines. The same pattern was applied to both surfaces of the sheet. 26
3.7 Illustration showing the tensile and hardness specimens of the welded sheet with laser pattern. 27
3.8 Set-up showing one of the cameras, (a), and post processing with mesh and virtual extensometer, (b), of tensile testing with DIC. . . . 30
3.9 Example of input and corresponding output using the software for calculating heat distribution with Rosenthal medium thick plate solution. 31
3.10 Diagrams showing (a) a realistic and (b) a simplified temperature history of extruded 6082 alloys subjected to artificial aging, welding, laser and PWHT/natural aging at room temperature (RT) (O.R. Myhr, Personal communication, 2019). 32
4.1 Optical micrographs of (a) the base material perpendicular to the extrusion direction and (b) the weld cross-section of welding speed 16 mm/s. The base material shows a fibrous grain structure, while the weld shows the recrystallized fusion zone. 33
4.2 Optical micrographs of weld cross-section of weld speed (a) 14 mm/s and (b) 18 mm/s showing the recrystallized fusion zone. 34
4.3 Hardness profiles of the weld cross-section for single-sided GMA joining weld at 16 mm/s welding speed. The extent of the HAZ is indicated with dashed lines. 35
4.4 Hardness profiles of the cross-sections of single-sided gas metal arc joining welds at weld speeds of (a) 14 mm/s and (b) 18 mm/s. The extent of the HAZ is indicated with dashed lines. 35
4.5 Stress-strain curves of specimens with cross welds and without PWHT. 36
4.6 Stress-strain curves of specimens with cross welds and PWHT. . . . 36
4.7 Evolution of principal strain localization during tensile testing of reference specimens (a) without PWHT and (b) with PWHT. 37
4.8 Evolution of principal strain localization during tensile testing of specimens with cross weld speed 18 mm/s (a) without PWHT and (b) with PWHT. 38
4.9 Fracture of specimen with cross weld speed 18 mm/s, without PWHT. 38
4.10 Fracture of specimen with cross weld speed 18 mm/s, with PWHT. . 39
4.11 Evolution of principal strain localization during tensile testing of specimens with cross weld speed 20 mm/s (a) without PWHT and (b) with PWHT. 39
4.12 Fracture of specimen with cross weld speed 20 mm/s, without PWHT. 40

4.13 Fracture of specimen with cross weld speed 20 mm/s, with PWHT. . 40
4.14 Evolution of principal strain localization during tensile testing of specimens with cross weld speed 22 mm/s (a) without PWHT and (b) with PWHT. 41
4.15 Fracture of specimen with cross weld speed 22 mm/s, without PWHT. 41
4.16 Fracture of specimen with cross weld speed 22 mm/s, with PWHT. . 42
4.17 Evolution of principal strain localization during tensile testing of specimens with cross weld speed 26 mm/s (a) without PWHT and (b) with PWHT. 42
4.18 Fracture of specimen with cross weld speed 26 mm/s, without PWHT. 43
4.19 Fracture of specimen with cross weld speed 26 mm/s, with PWHT. . 43
4.20 Hardness profiles at positions beneath the surface of (a) 0.8 mm and (b) 1.8 mm of specimens with 2000 W longitudinal laser. 44
4.21 Hardness profiles at positions beneath the surface of (a) 0.8 mm and (b) 1.8 mm of specimens with 2200 W longitudinal laser. 45
4.22 Hardness profiles at positions beneath the surface of (a) 0.8 mm and (b) 1.8 mm of specimens with 2600 W longitudinal laser. 45
4.23 Stress-strain curve of reference specimens with and without PWHT, where there are four specimens of each. 46
4.24 Stress-strain curve of specimens with 2000 W longitudinal laser treatment in HAZ. 47
4.25 Stress-strain curve of specimens with 2200 W longitudinal laser treatment in HAZ. 47
4.26 Stress-strain curve of specimens with 2600 W longitudinal laser treatment in HAZ. 48
4.27 Hardness profiles of specimens with laser pattern, where (a) is without PWHT and (b) is with PWHT. 49
4.28 Stress-strain curves of specimens with laser pattern. 50
4.29 Evolution of principal strain localization during tensile testing of specimens with laser pattern, where (a) is without PWHT and (b) is with PWHT. 51
4.30 Crack propagation during tensile testing of specimens with laser pattern, where (a) is without PWHT and (b) is with PWHT. 51
4.31 Predicted and measured thermal cycles for single pass GMA weld with $v = 10$ mm/s and $q_0 = 3221$ W at different distances form the weld center. 52
4.32 Predicted peak temperatures with several efficiency factors plotted together with measured thermocouple data. 53
4.33 Comparison of measured and predicted hardness profiles of welded specimens, where (a) is without PWHT and (b) is with PWHT. . . . 53
4.34 Comparison of measured and predicted hardness profiles welded specimens with 2200 W longitudinal laser treatment in HAZ, where (a) is without PWHT and (b) is with PWHT. 54

5.1 Comparison of the ultimate tensile strengths of the reference specimens from the two different tensile test set-ups. The value for the reference for laser is based on an average of four specimens. 56
5.2 Comparison of yield strength for specimens for cross welds of different welding speeds with or without post weld heat treatment (PWHT). 57
5.3 Comparison of ultimate tensile strength for specimens for cross welds of different welding speeds with or without post weld heat treatment (PWHT). 58
5.4 Comparison of percent elongation at fracture for specimens for cross welds of different welding speeds with or without post weld heat treatment (PWHT). 58
5.5 Illustration showing the HAZ and minimum hardness level due to the welds, where A, B, and C indicate locations of crack initiation. . 59
5.6 Comparison of ultimate tensile strength of specimens with longitudinal laser. 60
5.7 Percent elongation at fracture for specimens with laser pattern compared to reference specimens. 62
5.8 Ultimate tensile strength for specimens with laser pattern compared to reference specimens. 62
5.9 Comparison between the measured and predicted (η=0.7) peak temperatures during welding. The grey line shows where measured temperatures are equal predicted temperatures. 63
5.10 Measured hardness profile from welding process and corresponding peak temperatures. 64
5.11 Comparison between the measured and predicted hardness of welded specimens with 2200 W longitudinal laser. The grey line shows where measured temperatures are equal predicted temperatures. 64
A.1 Table summarizing the results from finite element simulataions of straight and bulged HAZ shape, where stress and elongation are presented for two different plate thicknesses and HAZ yield strength values. Copied from [31] I
B.1 Material certificate II
C.1 Specimen for DIC tensile testing of sheets with cross welds. III
C.2 Specimen for tensile test of sheets with longitudinal laser in minimum level HAZ. III
C.3 Specimen for DIC tensile testing of sheets laser pattern. III
D.1 NaMo input for hardness predictions (a) before simplification and (b) after simplification of the thermal history. IV
D.2 NaMo input for hardness predictions of welded sheet 9 mm from weld center at the upper surface (through thickness depth = 0). . . . IV
D.3 NaMo input for hardness predictions of welded sheet with 2200 W laser 9 mm from weld center 0.8 mm from the upper surface (through thickness depth = 0.8), where (a) is without PWHT and (b) is with PWHT of 220°C/15min. V
F.1 Stress-strain curves of all specimens tested with DIC. VII

G.1 Fractured reference specimen, without PWHT. VIII
G.2 Fractured reference specimen, with PWHT. VIII
G.3 Fractured specimen with cross weld speed 18 mm/s, without PWHT.VIII
G.4 Fractured specimen with cross weld speed 18 mm/s, with PWHT. .VIII
G.5 Fractured specimen with cross weld speed 20 mm/s, without PWHT. IX
G.6 Fractured specimen with cross weld speed 20 mm/s, with PWHT. . IX
G.7 Fractured specimen with cross weld speed 22 mm/s, without PWHT. IX
G.8 Fractured specimen with cross weld speed 22 mm/s, with PWHT. . IX
G.9 Fractured specimen with cross weld speed 26 mm/s, without PWHT. X
G.10 Fractured specimen with cross weld speed 26 mm/s, with PWHT. . X
G.11 Fractured specimen with laser pattern, without PWHT. X
G.12 Fractured specimen with laser pattern, with PWHT. X
H.1 Fractured specimens with longitudinal laser of 2600 W, without PWHT. XI

List of Tables

1 Chemical composition of base material EN AW-6082. 21
2 Parameters for the homogenization process of base material EN AW-6082. 21
3 Parameters for the extrusion process of the base material EN AW-6082. 21
4 Welding parameters of robotic GMAW process 23
5 Relevant values from the stress-strain curves presented above, and the cross weld (CW) speed is indicated in the description. 37
6 The average ultimate tensile strength, R_{UTS}, of specimens with laser treatment in HAZ. 49
7 Predicted temperatures for NaMo inputs. VI
8 Tensile properties from tensile testing of samples with laser in HAZ. Yield strength are excluded for the samples with laser as they were tested without extensometers. XI

Abbreviations

β	Equilibrium phase (Mg_2Si)
β'	Hardening precipitate in Al-Mg-Si alloys (semi-coherent rods)
β''	Hardening precipitate in Al-Mg-Si alloys (semi-coherent needles)
Al-Mg-Si	Aluminium-Magnesium-Silicon
DIC	Digital image correlation
FEA	Finite element analysis
FSW	Friction stir welding
FZ	Fusion zone
GMAW	Gas metal arc welding
GP-zones	Meta-stable Guinier–Preston zones
HAZ	Heat affected zone
HV	Hardness Vickers
IFE	Institute of Energy Technology
NaMo	Nanostructure Model
NTNU	Norwegian University of Science and Technology
MTP	Department of Mechanical and Industrial Engineering
PWHT	Post weld heat treatment
RT	Room temperature
SEM	Scanning electron microscope
SSSS	Super-saturated solid solution
T6	Alloy solution-treated and artificially aged to peak strength

1 Introduction

1.1 Background and motivation

Aluminium is a widely used metal and is favorable in a variety of applications within industries such as building and construction, food and drug, and transportation. Aluminium alloys generally provide high strength to weight ratio, good corrosion resistance, excellent machinability, pleasing physical appearance, and good formability [1]. Due to their lightweight, high strength advantage and good formability, aluminium alloys have replaced heavier metals such as steels for many applications [2]. The demand for aluminium alloys in the automotive industry is increasing due to the sustainability and recycling potential, along with decreased CO2-emissions and better performance due to weight savings resulting in environmental and safety benefits [3].

The Al-Mg-Si alloys, also known as the 6xxx series, are commercially attractive due to their physical properties, and they are frequently produced as extrusions for structural applications in buildings [1]. Good formability, adequate mechanical properties, excellent corrosion resistance, exceptional surface properties and good weldability are characteristic properties for these alloys [4, 5]. Al-Mg-Si alloys are age hardenable and frequently artificially aged to the T6 temper to obtain the highest achievable strength while other mechanical properties remain acceptable [6].

Even though the Al-Mg-Si alloys are considered weldable, they experience a deterioration of mechanical properties in a region close to the weld, called the heat affected zone (HAZ) [1]. Alloys in the T6 temper are especially prone to this softening effect, as the heat cycle of welding causes the growth of the strengthening particles that were obtained during aging [7]. The degree of strength reduction and the extent of the HAZ depends on the amount of heat generated in the welding process [1]. The deterioration of mechanical properties due to welding needs to be accounted for in the design of welded components and structures. Both the extent of the HAZ and the minimum strength level in the HAZ affects the load-bearing capacity of the weld [8]. For loads perpendicular to the weld, the design stress is limited to the minimum strength level in the HAZ [9]. Hence, the minimum level of HAZ strength is an important consideration in engineering design.

Regaining some of the lost strength in the HAZ is beneficial as it allows for higher design stresses, thus reducing the weight and cost of welded applications. Some studies involving manipulation of the HAZ geometry of welded 6082-T6 alloy have been conducted with varying results. Gjertsen [10] studied the effects of a laser pattern in the HAZ, concluding that melting due to high laser powers caused a reduction in strength rather than an increase. The results did, however, show promising results regarding the elongation of the specimens with laser treatment.

In the preceding specialization project to this current master thesis, the effects of transverse weld strings over the joining weld, referred to as "cross welds", were studied [11]. Cross welds made by gas metal arc welding (GMAW) and friction stir welding (FSW) showed the most promising results with a slight increase in tensile strength and significant improvements regarding elongation. Further research on methods for improving mechanical properties of welded aluminium is of interest, and manipulation of the HAZ indicates promising results.

1.2 Objective and scope

The objective of this study is to investigate the effects of local heat treatment methods according to the mechanical properties strength and ductility of welded 6082-T6 aluminium alloy.

This work is limited to tests on extruded 6082-T6 aluminium sheets welded by gas metal arc welding (GMAW), with three different local heat treatments:

1. Cross welds perpendicular to the joining weld
2. Local heating longitudinally in the HAZ made by laser
3. Local heating of the HAZ in a distinct pattern made by laser

Extensive mechanical testing, including hardness evaluation of the weld cross-section and tensile testing perpendicular to the weld, is carried out. Digital image correlation (DIC) is used to assess deformation behavior during tensile testing, and microstructural analysis with optical microscopy of the weld is conducted. The thermal program during welding and heat treatments are estimated by analytical models, and these results are further applied to a predictive model for estimating the resulting hardness. Comparison with experimental data is made in order to evaluate the accountability of these models for future predictive optimization of local heat treatments and manipulation of HAZ geometry.

2 Theory

The theoretical background for the work regarding this thesis is presented in this chapter. A description of the alloy and heat treatments are given, along with detailed descriptions regarding welding of the Al-Mg-Si alloys with focus on the weld thermal cycle and softening causes. Lastly, a predictive model for predicting the hardness response from a given thermal history is presented.

2.1 Al-Mg-Si Alloys

The 6xxx series are wrought, age hardenable aluminium alloys where magnesium and silicon are the primary alloying elements. To obtain sufficient strength, the alloys are often strengthened by precipitation hardening to the T6 temper [6]. They have moderately high strength and show good machinability, formability, weldability and resistance to corrosion [1]. Good formability means they are suitable for extrusion, and they are often utilized for structural applications such as architectural extrusions [1].

2.1.1 Main alloying elements

Magnesium and silicon are the main alloying elements of Al-Mg-Si alloys, where the concentration of magnesium is about 0.5-1.3 wt%, and the silicon concentration is 0.4-1.4 wt%. Manganese (Mn), chromium (Cr) and copper (Cu) are usually added in small quantities as well to enhance the properties of the alloy [12]. Figure 2.1 shows the equilibrium solid solubility of different alloying elements as a function of temperature. Magnesium increases the work-hardening potential and resistance to corrosion, while silicon contributes to increased strength and ductility. Both reduce the melting point, and together they make precipitation hardening possible [13]. Magnesium and silicone are added in the approximate ratio of 1.73/1 that allows for the formation of GP-zones and fine Mg_2Si-precipitates, which increases the strength of the material [1]. This is explained in more detail in Section 2.1.3.

Adding copper can help to increase the strength further during artificial aging [1]. A fibrous structure is desired as it can help corrosion resistance [14]. Both manganese and chromium are added to Al-Mg-Si alloys to control the grain structure and prevent recrystallization from occurring during hot working, e.g., extrusion, and heat treatments, which helps the formation of a fibrous structure after extrusion [1].

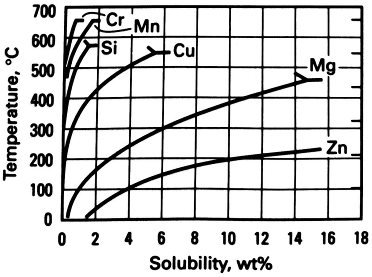

Figure 2.1: *Equilibrium solid solubility of different alloying elements as a function of temperature. Copied from [1].*

2.1.2 Thermal history of extruded Al-Mg-Si alloy

Figure 2.2 shows a simplified history of the thermal processes of extruded Al-Mg-Si alloy. After casting, the extrusion ingot is heated and soaked at approximately 560-585°C for several hours and then cooled down rapidly at a rate of 300-500°C/h [15]. This is favored above quenching for extrusion ingots as quenching will result in higher flow stresses for further processing. Too slow cooling will result in coarsening of precipitates and can cause eutectic melting when the ingot is reheated for extrusion causing surface defects on the extruded profile [15].

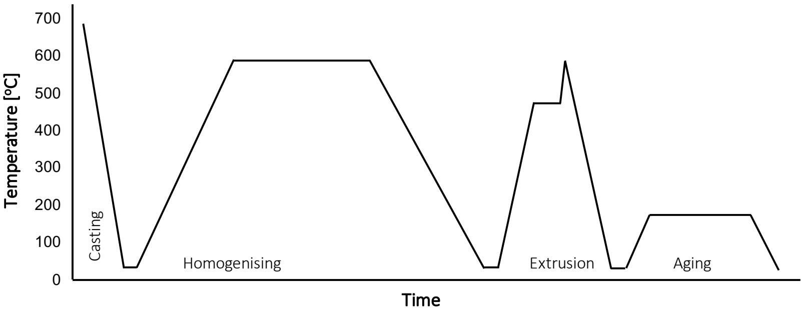

Figure 2.2: *The thermal history of extruded aluminium profiles, including estimated levels of Mg and Si in solid solution from [16].*

The ingots are preheated to about 440-500°C before extrusion [16]. Then, the preheated billet is forced through a die opening with the same cross-section as the final profile. In this process, the material flows by internal shear which is dependent on the material, interface friction between the material and the die as well as the die opening shape [1]. For extrusion of most aluminum alloys, there is friction between the material and the die and between the material and the container wall, which results in a flow pattern similar to the one illustrated by Figure 2.3. The shear deformation can extend from the outer region of the billet towards the center, which can lead to contaminated material with impurities mixing with the surface of the final profile [1]. The extrusion process could result in a temperature up to 600°C in the profile depending on the extrusion speed and reduction ratio [16].

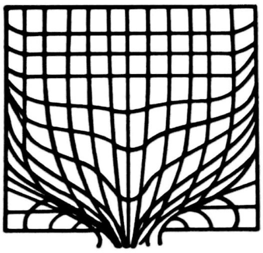

Figure 2.3: *Illustration of common flow pattern during extrusion of metals. Copied from [1].*

2.1.3 Precipitation hardening

Precipitation hardening, or age hardening, is often applied to the Al-Mg-Si alloys to improve mechanical properties such as strength and hardness [1]. The T6 temper, achieved by artificial aging, generally obtains the highest achievable strength while other mechanical properties remain adequate [1].

The aging process consists of several heat treatment steps where the temperature and time are important parameters to obtain the desired mechanical properties [1]. The heat treatment sequence starts with a solution heat treatment at a high temperature to maximize the solubility of the alloying elements, followed by rapid cooling to a lower temperature so that a supersaturated solid solution (SSSS) with solute elements is obtained [1]. Lastly, an aging heat treatment is done to increase the strength by forming finely distributed precipitates in the matrix. This can either be obtained by natural aging at room temperature (RT) or artificial aging at an elevated temperature (typically $150 - 200\,^{\circ}\mathrm{C}$ [16]) for several hours [1].

The generic precipitation sequence of Al-Mg-Si alloys can be considered as [4, 6, 16, 17]:

$$SSSS \rightarrow Atomic\ clusters \rightarrow GP - zones \rightarrow \beta'' \rightarrow \beta' \rightarrow \beta(Mg_2Si)$$

Precipitation starts from the supersaturated solid solution (SSSS), then clusters of the solute elements and GP-zones are formed during the first part of the process.

GP-zones are the first precipitates formed in the process and are fully coherent [18]. Then, semi-coherent β'' particles are formed. The needle-shaped β'' precipitates are aligned along the $\langle 100 \rangle-$directions. They are fully coherent along the needle axis, but not coherent in the matrix [12, 18]. The β'' precipitates will contribute to the hardening and strengthening of the metal and are associated with peak-aged T6 state [4, 18]. The coarser β' particles will form subsequently. These are rod-shaped and usually associated with the overaged state [18], but they can contribute to the hardening if they are finely dispersed in the matrix [12]. Lastly the stable equilibrium $\beta(Mg_2Si)$ plate-like precipitates are formed [18].

During the artificial aging process, the strength and hardness will increase with time during the aging process until a peak value is reached. This is the peak age T6 stage where metastable β'' and β' particles are the strength contributors [19]. Further soaking beyond this point will lead to an overaged state (T7 temper) with reduced strength [20]. Overaging can also be a result of higher aging temperatures than what is used to obtain the T6 temper of the same alloy [1]. Figure 2.4 shows a schematic diagram of how the strength develops during artificial aging, where the aging time is plotted on a logarithmic scale. The figure also shows how the alloy can naturally age at room temperature.

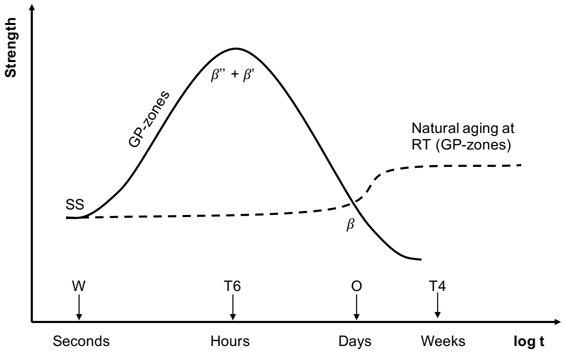

Figure 2.4: *Schematic illustration of the strength development during artificial and natural aging of Al-Mg-Si alloys (W: solution heat-treated condition; T6: peak-aged condition; O: fully annealed condition; T4: naturally aged condition). Copied from [19]*

2.1.4 Strengthening mechanisms

The materials' strength is dependent on several strengthening mechanisms that makes it harder for dislocations to move. These dislocation barriers could be grain boundaries, dislocations and particles in solid solutions as well as shearable and non-shearable particles [21]. The most important strengthening mechanisms for age hardened Al-Mg-Si alloys are solid-solution hardening and precipitation hardening giving the strength contributions σ_{SS} and σ_p respectively. This along with the yield strength of pure aluminium, σ_i, gives an expression for the total yield strength, σ_y, of the alloy [22]:

$$\sigma_y = \sigma_i + \sigma_{ss} + \sigma_p \tag{2.1}$$

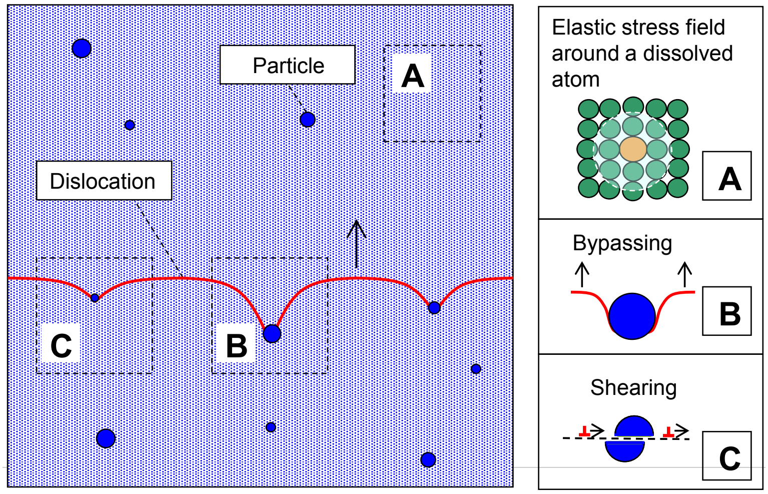

Figure 2.5: *Illustration showing the strengthening contributions of solid solution hardening, σ_{ss} and precipitation hardening, σ_p. Copied from [23]*

The solid solution strengthening involves the strength contribution of the alloying elements Si and Mg [22]. These elements are in solid solution as substitutional solutes, which have a different size than the matrix atom. This causes a misfit in the crystal lattice, and the solute atoms interact with the stress fields around the edge dislocations, as shown in Figure 2.5A, which strengthens the alloy [24]. The yield strength increases with the concentration of solutes [21].

Precipitation hardening of Al-Mg-Si involves precipitation from a supersaturated solid solution, as explained in the preceding section (Section 2.1.3). The precipitate particles can interact with the dislocations either by shearing or bypassing of particles [22]. Particles that are coherent or semi-coherent in the matrix can be cut by dislocations [24]. This shearing of a particle is illustrated in Figure 2.5 B. Incoherent particles are non-shearable particles that can only be bypassed by the Orowan mechanism [24], which is shown in illustration C in Figure 2.5. The particles serve as pinning points for the dislocations, which have to bow out between the particles. The segments of the dislocation that meet on the other side of the particle will annihilate, resulting in a dislocation loop (Orowan loop) around the particle along with a free dislocation that can continue the motion [24]. The strength contribution due to these particles depends on the spacing between them, which again is related to the size and the volume fraction [24].

2.2 Welding of Al-Mg-Si Alloys

2.2.1 Gas metal arc welding (GMAW) process

Gas metal arc welding (GMAW), illustrated in Figure 2.6, is a fusion welding method that offers good penetration, does not require flux and has very few limitations when it comes to welding positions [25]. It is a high-speed arc welding process that is highly applicable for automatic and robotic operations [1]. The process offers good control of the welding parameters such as welding speed, current, voltage, and wire feed speed. GMAW uses a consumable electrode, that also serves as filler metal, and is connected to the positive pole of the direct current power supply. This provides a continuous cleaning action to remove the oxide layer, and the arc is concentrated to ensure rapid melting [1, 26]. The filler wire is automatically and continuously fed through the nozzle of the weld gun [25], and the plasma arc of inert gas (usually argon) protects the weld pool [26]. Typical filler metals for welding of aluminum are Al-Si or Al-Mg alloys [7]. Specific alloys such as 5356, 5183 and 4042 are recommended for welding of AA6082 [12, 13].

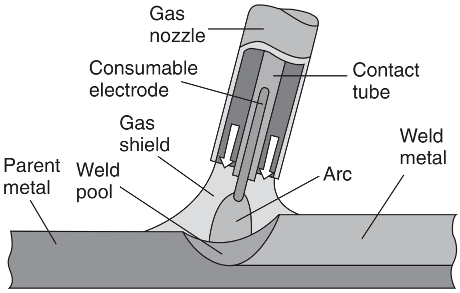

Figure 2.6: *Illustration of the GMAW process with basic features such as the electrode, arc and shielding gas indicated. Copied from [26].*

Typical problems related to welding of Al-Mg-Si alloys are reduced HAZ strength level, solidification cracking and hot cracking [7]. Solidification cracking and hot cracking both occur intergranular and is related to eutectic liquid at the grain boundaries together with stresses caused by shrinkage during solidification. While solidification cracks form in the weld metal, hot cracks are linked to high peak regions of the HAZ [7]. Precipitation hardened alloys usually experience softening in the HAZ due to the reversion of precipitates. This is explained in more detail later in Section 2.3.2.

2.2.2 The thermal cycle of welding

Information about the weld thermal cycle is important to understand the metallurgical reactions of welding [7]. Based on this information, it is possible to predict the characteristics of the weld, especially the reduced strength in the HAZ, by physical models [27], which is further explained in Section 2.6. During arc welding, a concentrated energy source is required to minimize the loss of heat to the surroundings [12]. For gas metal arc welding (GMAW), the typical arc power, q, is between 500-5000 W/mm^2, and the heat loss is usually accounted for by the arc efficiency factor [12]. For the GMAW process on aluminium the arc efficiency factor is 0.7-0.85 according to Christensen et al. [28].

Analytical models for predicting the heat flow and temperature distribution in arc welding are considered to offer sufficient accuracy despite simplifying assumptions [27]. Rosenthal's equations assume pseudo-steady state where the temperature does not change with time when observed from a point inside the heat source and can describe the temperature field around the heat source [7].

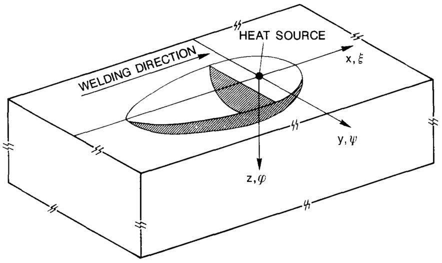

Figure 2.7: *Schematic representation of Rosenthal thick plate solution showing a moving point source. Copied from [27].*

The three-dimensional heat source of Rosenthal thick plate solution is illustrated in Figure 2.7 and given by equation:

$$T - T_0 = \frac{q_0}{2\pi\lambda}\frac{1}{R}\exp\left(-\frac{v}{2a}\left(R + x\right)\right) \tag{2.2}$$

where

$$R = \sqrt{x^2 + y^2 + z^2} \tag{2.3}$$

The thick plate solution (Eq. 2.2) assumes an isotropic semi-infinite body with initial temperature, T_0, and that thermal properties are independent of temperature [27]. Heat losses due to radiation and convection are ignored, thus no heat loss from the surface. Conduction of heat is assumed in all three directions which requires the assumption of infinitely large specimen [12]. q_0 is the arc power received by the weld and is dependent on the welding current and arc voltage. v is the travel speed, λ is the thermal conductivity of the material and x is the welding direction [27].

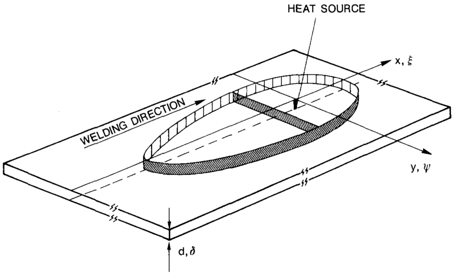

Figure 2.8: *Schematic representation of Rosenthal thin plate solution showing a moving line source on a thin sheet. Copied from [27].*

A thin plate solution is applicable assuming that full through thickness penetration is attained by one pass of the heat source. Similar assumptions as for the thick plate solution, except it assumes two-dimensional heat conduction with a fixed plate thickness, d, as oppose to an infinitely thick plate. Rather than assuming a point heat source, a line source is considered for this model as illustrated in Figure 2.8. The equation for the thin plate solution is given by [12]:

$$T - T_0 = \frac{q_0/d}{2\pi\lambda} \exp\left(-\frac{vx}{2a}\right) K_0\left(\frac{vr}{2a}\right) \tag{2.4}$$

where

$$r = \sqrt{x^2 + y^2} \tag{2.5}$$

The assumptions of the thick plate solution and the thin plate solution does not apply to most practical welding cases, as variable temperature gradients in the through thickness directions does not comply with the assumption of either three-dimensional or two-dimensional heat flow [7]. This problem is solved by placing imaginary reflecting heat sources at symmetrical distances from the surface of the plate, as shown in Figure 2.9. This is done in order to maintain a zero net flux of heat through the two surfaces of the plate [27]. This is the basis for Rosenthal medium thick plate solution, where the heat source is considered a point similar to the thick plate solution, but the plate has a fixed thickness, d. The contributions from all imaginary sources are included in a convergent series, and the temperature distribution of the process is given by equation (2.6) [7]:

$$T - T_0 = \frac{q_0}{2\pi\lambda} \exp\left(-\frac{vx}{2a}\right) \left[\sum_{i=-\infty}^{i=+\infty} \left(\frac{1}{R_i}\right) \exp\left(-\frac{v}{2a} R_i\right)\right] \tag{2.6}$$

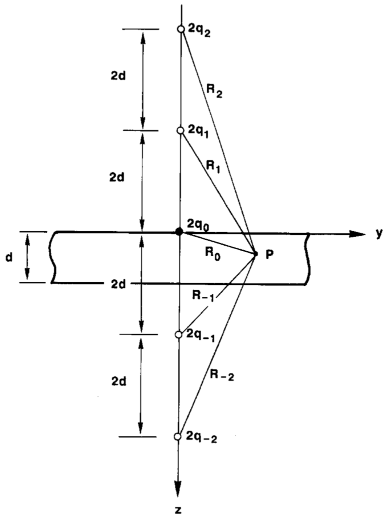

Figure 2.9: *The real and imaginary point sources on a plate of finite thickness, d, assumed for the Rosenthal medium thick plate solution. Copied from [27].*

where

$$r = \sqrt{x^2 + y^2 + (z - 2id)^2} \tag{2.7}$$

Close to the source, the medium thick plate solution (Eq. 2.6) is the summation of the thick plate solution (Eq. 2.2) for each imaginary heat source which gives a good estimation of the temperature close to the weld center [27]. Far away from the source, the equation converges to the thin plate solution (Eq. 2.4). The part in between these regions, the thermal conditions are best described by the medium thick plate solution [12]. Due to variable temperature gradients in the through-thickness direction of the plate within this "transition" region, the other two solutions (eq 2.2 and 2.4) will deviate notably from experimental results [27]. The medium thick plate solution usually gives the best approximation of the thermal cycle of aluminum welding, due to the high thermal conductivity of aluminium [12]. Figure 2.10 shows a comparison of measured thermal cycles during GMA welding of aluminium compared to the weld thermal cycle predicted by the medium thick plate solution for fixed peak temperatures. This suggests that the equation is able to give satisfactory predictions of the thermal cycles during welding [27].

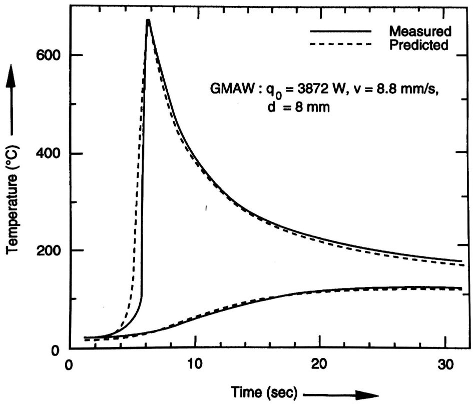

Figure 2.10: *Measured thermal cycles during welding of aluminium compared to weld thermal cycle predicted by the medium thick plate solution for fixed peak temperatures. Copied from [27]*

2.3 Softening in the heat affected zone (HAZ)

2.3.1 Weld zones

Figure 2.11 shows the different zones of welded Al-Mg-Si alloys. The material distant from the weld, which is not affected by heat generated in the welding processes, is referred to as the base material or unaffected material [1]. For a fusion welding process such as GMAW, there are two distinct zones of interest; the fusion zone (FZ) and the heat affected zone (HAZ). The FZ is a combination of base metal and filler metal and has an as-cast microstructure [26]. Several factors affect the properties of this zone, such as the composition of the added filler metal, quality of the welding process, and solidification rate[26]. The HAZ is outside the fusion zone, and the age hardened alloys experience a reduction in strength and hardness in this region. The width of the HAZ and the degradation of properties depends on the temperature distribution during welding [12].

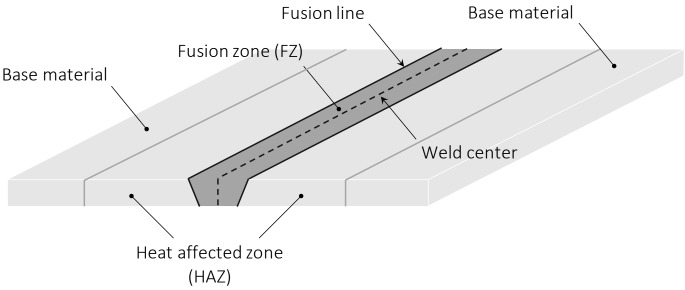
Fusion line
Base material
Fusion zone (FZ)
Base material
Weld center
Heat affected zone
(HAZ)

Figure 2.11: *Illustration showing the resulting zones in the cross-section of Al–Mg–Si alloy fusion welds. The outer boundary of the HAZ is indicated by the grey lines.*

2.3.2 Softening causes

Al-Mg-Si alloys in the T6 temper are particularly prone to softening in the HAZ, as the heat generated by the weld cycle affects the precipitation hardened structure [1]. This causes the hardness and strength to be significantly lower than the base material in this region.

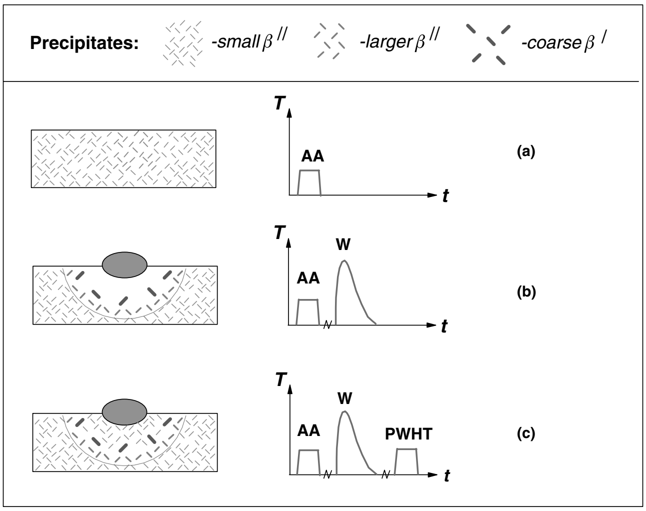
Precipitates:
-small β''
-larger β''
-coarse β'
T
AA
t
(a)
T
W
AA
t
(b)
T
W
AA
PWHT
t
(c)

Figure 2.12: *Illustration showing the evolution of the microstructure during artificial aging (AA) (a), welding (W) (b) and post weld heat treatment (PWHT) (c) of Al–Mg–Si alloys. The outer boundary of the HAZ is indicated by the semicircles in the diagrams. Copied from [29]*

Dissolution, coarsening and transformation of β'' particles are the main contributors to significant hardness reduction and is the cause of softening in the HAZ [8]. The process is described in Figure 2.12. After precipitation hardening, there are many small β'' particles evenly distributed in the matrix, and these are the main contributors to the strengthening [29], as illustrated in Figure 2.12(a). During welding, the microstructure in the HAZ will change, which is apparent from Figure 2.12(b). Where the temperature has reached a temp of approximately 250°C, dissolution of the smallest β'' particles will occur while the larger β'' particles will start to grow [29]. In the region where the temperature has reached between 250-480°C, the β'' particles will grow further, and the β'' phase will transform into β' phase. The β' phase in the region closest to the fusion zone will dissolve which means full reversion of the β'' particles is attained [8, 29]. This results in solid solution hardening [8]. Immediately after welding, this will be the zone of lowest hardness and is illustrated in Figure 2.13a [12]. Room temperature aging (natural aging) will occur after a period of 5 to 7 days close to the fusion line where the alloying elements are in solid solution after welding [7]. Some strength recovery is observed due to this, as illustrated in Figure 2.13b. However, where the temperature has been about 430 °C, this does not occur to the same extent, and this is the region of lowest hardness along the cross-section as shown in Figure 2.13b.

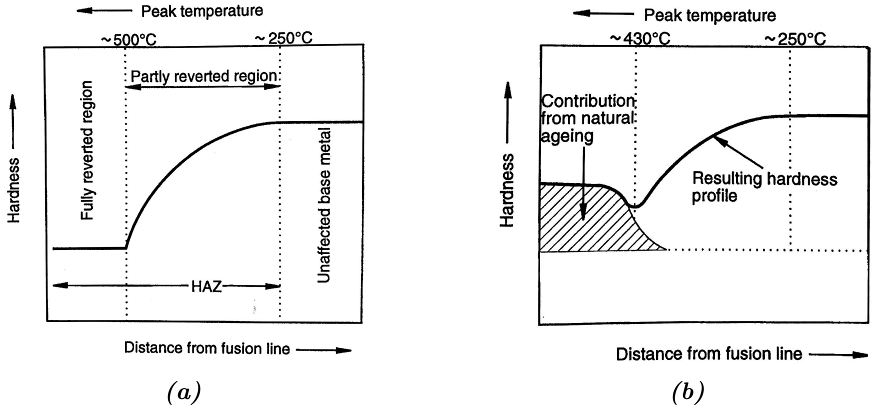
Peak temperature
~500°C
~250°C
Partly reverted region
Fully reverted region
Unaffected base metal
Hardness
HAZ
Distance from fusion line
Peak temperature
~430°C
~250°C
Contribution from natural ageing
Resulting hardness profile
Hardness
Distance from fusion line

(a) *(b)*

Figure 2.13: *Hardness distribution after welding (a) following dissolution of $\beta''(Mg_2Si)$ particles and (b) after prolonged natural aging. Copied from [7].*

2.3.3 Post weld heat treatment (PWHT)

Natural aging can regain some strength, and heat treatment after welding can be used to recover even more of the lost strength in the HAZ [12]. The process can include solution heat treatment and aging or solely aging of the welded component [1]. The artificial aging after welding is denoted "PWHT" (post weld heat treatment) in this thesis.

The PWHT causes reprecipitation of β'' particles in the region where there is a high content of Mg and Si in solid solution [29], as can be seen in Figure 2.12(c). This is the region close to the weld where reversion of β'' particles was the prevailing softening effect. This will not occur to the same extent in the regions further from the weld where there is not sufficient solute for reprecipitation to occur [29]. That means there will be a region in the HAZ with permanent low hardness even after PWHT. Furthermore, the PWHT of an alloy in the T6 temper can result in reduced hardness of the base material due to overaging in this region [1].

2.4 Modification of HAZ geometry

2.4.1 General concept

Artificial aging of a welded component (PWHT) can regain strength in the HAZ and increase the load-bearing capacity of the welded component. However, PWHT is not always applicable e.g., large welded specimens or parts welded on-site attached to larger structures. A concept of modifying the geometry of the HAZ with a local heat treatment has been proposed by Fjær. Finite element analysis has indicated increased global properties such as strength and ductility [30]. Hydro, SINTEF, and IFE have initiated a project to investigate this possibility further.

Modification of the HAZ geometry is based on introducing heat locally to specific regions in the HAZ. As described in Section 2.3.2, this region suffer from a severe strength loss due to the thermal weld cycle. The idea of the local heat treatment is to reheat this region with a temperature sufficient to cause reversion of the particles, which allows for strength recovery by natural or artificial aging (PWHT) after welding [31]. Manipulating the geometry of the HAZ is investigated by applying heat locally in a pattern or parallel to the weld string in the minimum strength HAZ.

2.4.2 With welds

With the use of GMAW, heat is introduced locally by welds applied transverse to the longitudinal joining weld in a specific pattern. The heat input should cause the dissolution of β'' particles, and improve the aging potential under and close to the transverse welds [31]. This local strength increase should affect the geometry of the HAZ, causing strain to localize differently than in a straight line parallel to the HAZ. Finite element analysis (FEA) conducted by H. G. Fjær [31] show that the load-bearing capacity of the weld can be increased if the minimum strength HAZ is positioned between regions of higher strength [31]. This is analogy is simulated by a bulged HAZ and compared to a straight HAZ, as shown in Figure 2.14 where the strain fields of the two cases are presented. An increase in both strength and elongation is observed, and the results are presented in Figure A.1 in Appendix A. The cross welds are expected to have a similar influence on the strength and elongation of the welded component. Added cross-section area from weld beads could also contribute to an additional strength increase [31]. This was partly confirmed in the project thesis preceding this master thesis, where cross welds showed a large increase in elongation, but not significant improvements regarding strength [11].

Note that the descriptions "transverse welds" or "cross welds" are used in this thesis to describe the local heat treatment by adding welds across the joining weld.

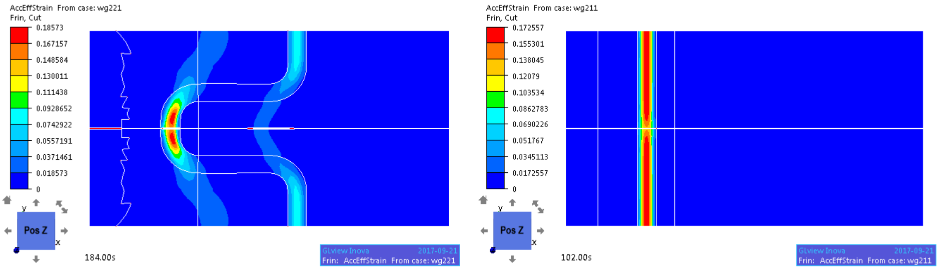

(a) ***(b)***

Figure 2.14: *Finite element analysis of the modified HAZ geometry showing plastic strain of (a) bulged HAZ and (b) straight HAZ. Copied from [30].*

2.4.3 With laser

O. R. Myhr and R. Østhus have proposed local heat treatment of the minimum strength level in HAZ. The idea is to introduce enough heat in the soft HAZ region to facilitate reprecipitation by aging (O.R. Myhr and R. Østhus, Personal communication, 2019). Introducing heat locally by a laser (Light Amplification by Stimulated Emission of Radiation) enables the possibility of tailoring the treatment to a greater extent than adding cross welds. For instance, solid-state lasers are considered the most versatile laser system and can provide a wide range of output powers [32].

Local heat treatments to modify the mechanical properties of aluminium, has been investigated for different purposes, such as increasing the formability of blanks prior to a forming process [33]. This method is referred to as Tailored Heat Treated Blanks (THTB). In the study by Geiger et al. [34], a robot controlled laser was used to introduce heat locally with the aim of increasing the grain size (recrystallization), decrease the dislocation density (annealing) and dissolve MgSi precipitates (modifying precipitation structure). The latter is of interest in this thesis. As opposed to the TBHT study where the objective was to soften the material, the reasoning is that the particle dissolution will result in solid solution and allow for reprecipitation by aging which can give similar strength increase as observed in the HAZ region closer to the weld.

2.5 Load bearing capacity

There is a connection between the peak temperature during welding of 6082-T6 aluminium alloy and the resulting hardness and strength in the HAZ, which is related to the growth and reversion of β'' particles [35] as described in Section 2.3.2. The reduced hardness and strength in the HAZ need to be accounted for in the design of welded components and structures. There are several design codes such as British Standard BS 8118 and Eurocode 9 that can account for this reduction, where the latter is more conservative and will be briefly presented in this section [9].

Eurocode 9 requires predominantly static loads of components, a welding procedure resulting in normal quality of the weld and the use of the recommended parent and filler metal combinations [13]. Based on these assumptions, a softening factor, ρ_{HAZ}, of 0.65 is suggested for the Al-Mg-Si alloys in the T6 temper. For forces acting perpendicular to the weld, the following design stress of the HAZ is suggested [13]:

$$\sigma_{HAZ} = \frac{f_{a,HAZ}}{\gamma_M} \tag{2.8}$$

where

$$f_{a,HAZ} = \rho_{HAZ} f_u \tag{2.9}$$

ρ_{HAZ} is the softening factor, f_u is the ultimate tensile strength of the base material, and γ_M is a partial safety factor, which is γ_{M2}=1.25 for welded connections [13].

When considering load-bearing capacity perpendicular to the weld as illustrated in Figure 2.15, the nominal stress, $\sigma_\perp$, of the welded sheet is given by [9]:

$$\sigma_\perp = \frac{P}{A} = \frac{P}{dW} \tag{2.10}$$

where P is the applied force, tensile or compressive, A is the cross-section area of the joint defined as the sheet thickness, t times the width, w, not considering the protrusion of the weld bead. For design purposes, the nominal stress, $\sigma_\perp$, must be less or equal to the minimum strength of the HAZ, σ_{min} ($\sigma_\perp \leq \sigma_{min}$) [9]. σ_{HAZ} given in Eq. 2.8 should be used as σ_{min} for design purposes to be in accordance with Eurocode 9.

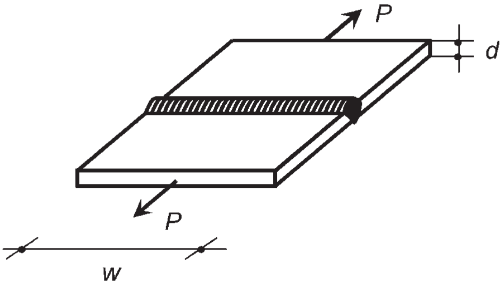

Figure 2.15: *Illustration of loading conditions perpendicular to the weld. Copied from [9].*

Equations 2.11 and 2.12 can convert the hardness values in the HAZ to yield or ultimate tensile strength at equivalent positions for Al-Mg-Si alloys [7, 36]. These regression formulas can be used to calculate the yield or tensile strength along the HAZ based on measured hardness values.

$$R_{p0.2}(MPa) = 3.0HV - 48.1 \tag{2.11}$$

and

$$R_{UTS}(MPa) = 2.6HV + 39.8 \tag{2.12}$$

2.6 Modelling and prediction of properties

Hydro (T. Furu and O. R. Myhr) has developed a methodology which aims to optimize the production of aluminum alloys [37]. Material-, mechanical-, cost-, and sustainability models, are used to predict and optimize the resulting properties of the aluminum product, as well as the production costs and environmental impact of production. A software called PRO$^{3\,TM}$ (Profit generation through Product and Process Optimization) combines these models in an iterative process involving all models in the process chain until the predefined requirements are met [38]. Different models are utilized through the process of casting, homogenization, extrusion, and aging to predict different mechanical properties based on the thermal and mechanical history [38].

NaMo (Nano-structure Model) [22, 39, 40, 41] is a physically based model developed by O. R. Myhr and Ø. Grong. The model is a combined precipitation-, yield strength-, and work hardening model and can account for the coupled effect of nucleation, growth, and coarsening of particles [23]. Modeling results have been compared to experimental data and is considered a sufficient guiding tool for predicting the strength of a certain alloy with a given thermal history [40]. The model has shown the ability to reproduce both the age hardening response and the reduced strength of welds [41]. In order to predict the response of the material, mathematical models are utilized along with the assumption of spherical particles. Although the particles are needle and rod-shaped for Al-Mg-Si alloys [12, 18], this simplifying assumption has proven to be adequate for this purpose and give similar results [41]. A microstructure model considers the nucleation of particles and determines whether a particle will grow or dissolve due to the applied thermal cycles [40]. A strength model considers the strengthening effects caused by precipitation (Orowan looping and shearing of particles) and solid solution [40]. These strengthening effects are added linearly as in Eq. 2.1, to get an expression of the overall yield strength. Furthermore, Eq. 2.11 is used to convert the yield strength to Vickers hardness (HV).

3 Experimental

Detailed descriptions of the experimental work are given in this chapter, explaining the welding and heat treatment processes. Sample preparation and different test set-ups are explained, and descriptions of the simulations and predictions are given.

3.1 Base material

The aluminium alloy used for the experimental work in this thesis is EN AW-6082. The extrusion ingot was delivered by Hydro Karmøy with the chemical composition presented in Table 1. The materials certificate is listed in Appendix B Figure B.1. The parameters of the homogenization process are given in Table 2.

Table 1: *Chemical composition of base material EN AW-6082.*

Alloying element [wt%]									
Si	Fe	Cu	Mn	Mg	Cr	Zn	Ti	Cd	Al
0.99	0.2	0.01	0.54	0.66	0.01	0.00	0.02	0.00	97.56

Table 2: *Parameters for the homogenization process of base material EN AW-6082.*

Holding temp. [°C]	Holding time [h]	Heating rate [°C/h]	Cooling rate [°C/h]
555	3	200	350

The ingot was extruded at Hydal Aluminium Profiler AS at Raufoss, and the parameters of the extrusion process are given in Table 3. The extruded profile was aged at 185°C for 5 hours at SINTEF Manufacturing AS at Raufoss to achieve the T6 temper condition.

Table 3: *Parameters for the extrusion process of the base material EN AW-6082.*

T_{billet} [°C]	v_{max} [m/min]	v_{avg} [m/min]	Pmax [bar]
480	8.14	5.87	158

3.2 Specimen preparation

3.2.1 Preparation process

The extruded profile with thickness of 3.6 mm was cut into sheets of approximately 300 mm x 150 mm. Two sheets were welded together by gas metal arc welding (GMAW) before three different local heat treatments (cross welds, longitudinal laser, and laser pattern) were applied. This process is illustrated in Figure 3.1. GMA weld strings were applied across the joining weld, and these welds are referred to as "cross welds" in this thesis. The laser treatment was applied in two different ways: in longitudinally in the HAZ parallel to the weld string or in a pattern of several shorter laser lines, both at the upper and lower surface of the sheet.

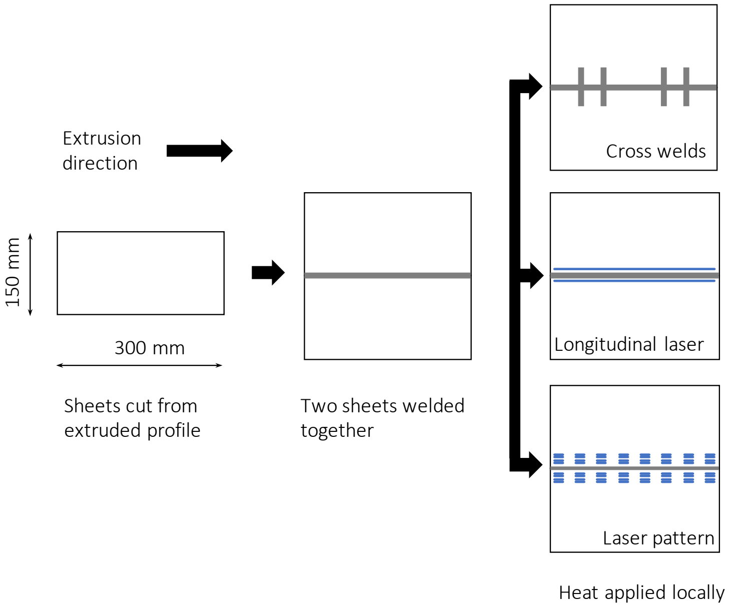
Extrusion direction
150 mm
300 mm
Sheets cut from extruded profile
Two sheets welded together
Cross welds
Longitudinal laser
Laser pattern
Heat applied locally

Figure 3.1: *Illustration showing the process of cutting, welding and application of local heat treatments.*

3.2.2 Welding GMAW of sheets

The gas metal arc welding (GMAW), was conducted at Bentler Automotive Raufoss AS. Two sheets were clamped onto a stainless-steel backing and joined with single pass square butt weld by an automatic welding robot. An Aluminium – Magnesium alloy, AlMg5Cr(A) (5356), with a diameter of 1.2 mm was used as filler metal. The welding parameters are presented in Table 4, and welding speed, current, voltage, and wire feed speed were constant during the process. Three different welding speeds of 14 mm/s, 16 mm/s and 18 mm/s were tested, and 16 mm/s was chosen for the joining welds. Thermocouples were used to measure and log the temperature during welding at certain distances from the weld center. The distances were measured with a ruler of measuring intervals of 1 mm. Thus the accuracy of the positions are accordingly and likely within ±0.5 mm.

Table 4: *Welding parameters of robotic GMAW process*

Welding speed [mm/s]	Current [A]	Voltage [V]	Wirefeed speed [m/min]
16	177	18.2	10.2

3.2.3 Post weld heat treatment (PWHT)

The post weld heat treatment (PWHT) that selected specimens are subjected to, involves a heat treatment at a temperature of 220 °C for 15 minutes after welding. This process was conducted separately for all the three different specimens (cross welds, longitudinal laser and laser pattern), hence deviations regarding the process can occur. The PWHT of the cross welded specimens and the specimens with longitudinal laser was carried out at Sintef Manufacturing at Raufoss, while the laser pattern specimens were heat treated at a laboratory at NTNU Gløshaugen.

3.2.4 Local heat treatment by cross welds

Transverse welds were applied over and perpendicular to the existing GMA joining weld in a pattern as described in Figure 3.2 as proposed by Fjær [31]. This is the same pattern as for the specimens tested in the specialization project preceding this masters thesis [11]. The cross welds were obtained by different welding speeds of 18, 20, 22 and 26 mm/s along with the remaining parameters in Table 4. The welds made by 18 mm/s and 20 mm/s welding speed melted through the plate and were visible at the opposite surface. The specimen with cross weld speed of 22 mm/s was the first specimen where this did not occur, and for the specimens with 26 mm/s weld speed, the cross welds were barely visible at the opposite surface. A PWHT was applied to one of each distinct specimen, and the process of adding cross welds, splitting of sheets and PWHT is shown in Figure 3.3.

The specimens for tensile testing were cut by a water jet at "Finmekanisk verksted" at NTNU Gløshaugen in accordance with measurements Figure C.1 given in Appendix C, where the welds were centered in the specimen. The specimen geometry was chosen based on the amount of material available while including the pattern of the cross welds. The HAZ extends about 15-20 mm from the weld center

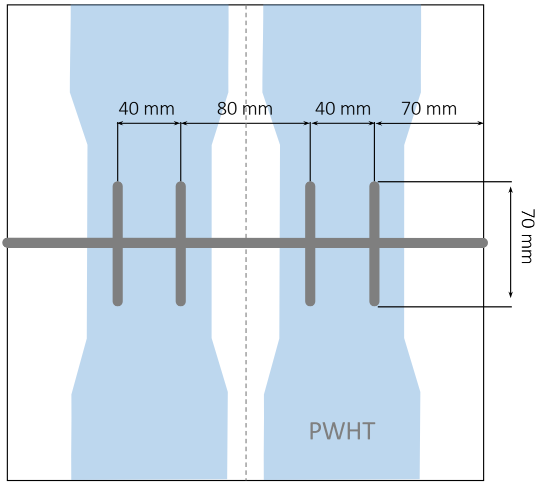
40 mm
80 mm
40 mm
70 mm
70 mm
PWHT

Figure 3.2: *The pattern of the applied GMA cross welds.*

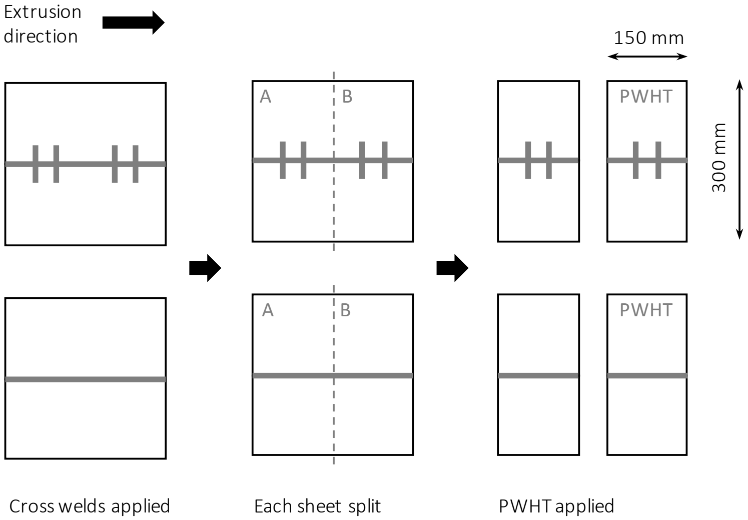
Extrusion direction
150 mm
300 mm
A
B
A
B
PWHT
PWHT
Cross welds applied
Each sheet split
PWHT applied

Figure 3.3: *Illustration showing the process of applying the cross welds and PWHT.*

for these specific welding parameters and material according to hardness measurements conducted for similar weld and base material [11]. Based on this, the width of the specimens is sufficiently large to cover the HAZ and not be affected by the cross welds at the edges. The specimens were cut out from the sheets at positions where weld defects related to start and stop of the welding process were less likely to reduce the load bearing capacity.

3.2.5 Local heat treatment by longitudinal laser

A TruLaser Cell 3000 laser was used to introduce heat locally to the HAZ of the welded sheets. The sheets were brushed with a steel brush and cleaned prior to the laser treatment. A laser with spot diameter of 3 mm was run over the surface at a speed of 10 mm/s with different effects of 2000, 2200 and 2600, W. The longitudinal laser lines were applied at a distance of 8.5 mm from the weld center on both sides of the weld as illustrated in Figure 3.4. This was again done at the lower surface of the sheet, making a total of four lines of laser on each sheet. The position was based on the lowest hardness value according to hardness measurements of the weld cross-section given in Chapter 4. This local heat treatment is denoted as "longitudinal laser" in this thesis. Lastly, a PWHT was applied to one of each kind.

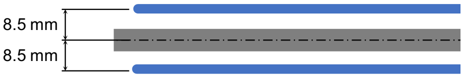

Figure 3.4: *Illustration showing the position of the longitudinal laser treatment, indicated by blue lines. The laser treatment was applied to both surfaces of the sheet.*

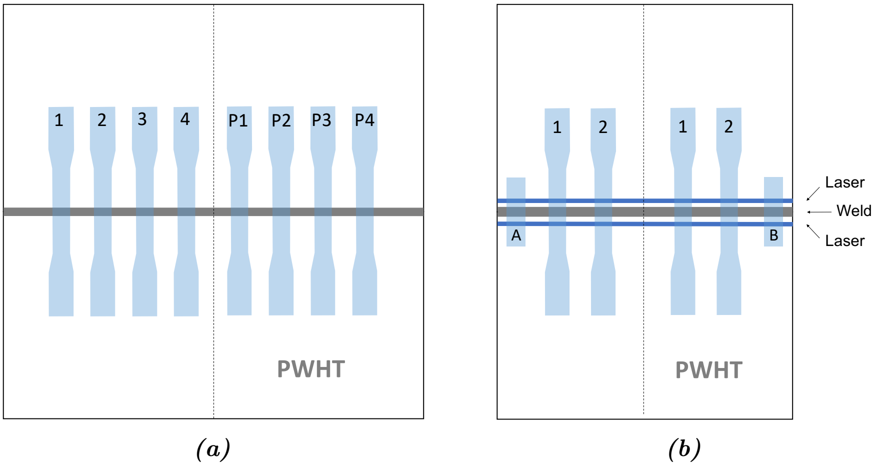

(a) *(b)*

Figure 3.5: *Illustration showing where the specimens for hardness and tensile testing were extracted. (a) shows the reference specimens and (b) shows the specimens with longitudinal laser treatment indicated by blue lines.*

Figure 3.5 shows where the different specimens for tensile testing and hardness measuring were taken, for both the reference specimens and the laser treated specimens. Two tensile specimens and one hardness specimen were extracted from each sheet with laser, while four untreated specimens and four with PWHT was extracted for reference. The specimens were taken at a distance from the edge of the sheet to avoid areas such as the start or stop of the weld and laser where defects are more likely. This was to minimize the possibilities of defects compromising the strength of the joint and obscure the effects of the laser treatment. The dimensions of the tensile test specimens are given in Figure C.2.

3.2.6 Local heat treatment by laser pattern

A laser was run in a pattern across the surface of the sheet in order to modify the HAZ geometry. The sheet was brushed with a steel brush and cleaned prior to the laser treatment. A TruLaser Cell 3000 laser with an effect of 2000 W and a spot size of 3 mm was applied in a pattern according to Figure 3.6. The first laser line was applied 8.5 mm from the weld center which approximately comply with the point of lowest hardness and strength in the HAZ. Then, three more laser lines were applied outward from that with 4 mm spacing. The laser speed was set to 10 mm/s and the laser power was "on" for 15 mm and "off" for 20 mm, resulting in lines of length 15 mm with 20 mm spacing in the direction parallel to the weld. Then, the same process was repeated at the opposite surface of the sheet.

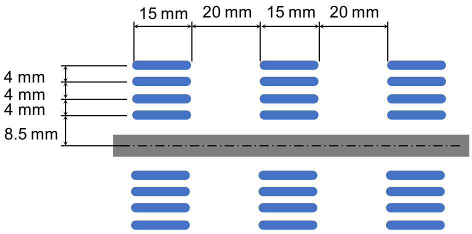

Figure 3.6: *Illustration showing the pattern of the laser treatment indicated by blue lines. The same pattern was applied to both surfaces of the sheet.*

The specimens for hardness and tensile testing were extracted from the welded and laser treated sheet as shown in Figure 3.7. The width of the specimen for tensile testing is large enough to cover two of the laser pattern regions as can be seen in the Figure, and specific dimensions are presented in Figure C.3 in Appendix C. A post weld heat treatment (PWHT) was applied to one of each tensile and hardness specimen for comparison.

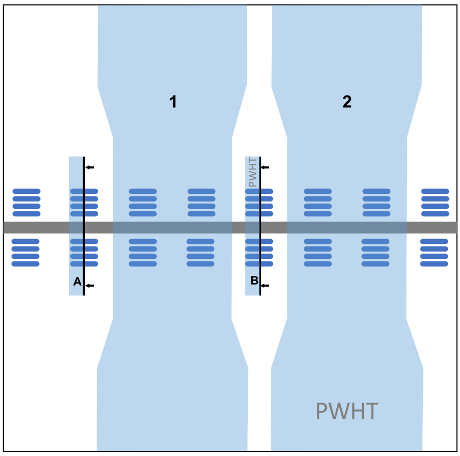

__Figure 3.7:__ Illustration showing the tensile and hardness specimens of the welded sheet with laser pattern.

3.3 Sample preparation, examination and testing

3.3.1 Optical microscopy

Samples for optical microscopy were cut with a water-cooled cutting machine with a SiC cut-off wheel. To ensure adequate adhesion between the sample and the resin, the sample were cleaned with aceton before they were cold mounted in Epoxy resin and set for curing at room temp for 12 hours. A process of grinding, polishing and anodizing was needed to prepare for optical microscopy.

The samples were ground by hand using SiC grinding papers of decreasing roughness. The following sequence of P80, P120, P220, P500, P1000, and P4000 was used for all samples. Each step was repeated until no grinding groves from the previous step were visible to the naked eye. The samples were rinsed in water and alcohol and between each operation. After grinding, the samples were polished with 3 μm disk with DiaPro Mol suspension and lastly 1 μm disk with OP-S suspension. Before each polishing steps, the samples were cleaned in an ultrasonic bath to ensure all particle from previous operations were removed. In order to analyze the samples under polarized light in an optical microscope, an anodized layer needed to be formed on the polished surface. This was obtained by electrolytic etching, with an electrolyte composed of 5% HBF_4 and 95% H_2O. A potential of 20 V and a max allowed current of 1 A was set before the samples were immersed in the electrolyte for 90 seconds. The samples were immersed in water immediately after the process before being cleaned with ethanol and dried with a dryer.

A Leica MeF4M optical microscope with a lens of 2.5x magnification was used to examine the samples. In order to see the grain structure, polarization contrast was used. The images were assembled in Microsoft PowerPoint to make an overview image of the cross-section.

3.3.2 Hardness testing

The hardness was measured over the cross-sections of the GMAW welds in order to find the hardness profiles and determine the impact of the different local heat treatments. All samples were grinded with SiC grinding papers until smooth and free of scratches before the hardness was measured. The measurements were taken with a Mitutoyo Micro Vickers Hardness testing machine (HM-200 series), using an impression force of 1 kg and dwell time of 10 sec to obtain the Vickers hardness (HV). To find the hardness profiles over the weld and HAZ, indents were made from the center of the weld cross-section and spaced 1 mm apart until the hardness reached the base material hardness.

The hardness of the welded cross-sections was measured 1.8 mm beneath the surface, i.e., the center of the thickness of the welded sheets to determine the hardness profile of the HAZ. The hardness of the samples with laser was measured at several locations along the cross-section, to examine the effect of the laser throughout the thickness of the sheet. The laser treatment was not excepted to affect the properties through the entire thickness, which is why the hardness was measured at different positions. These were chosen to be 0.8 mm and 1.8 mm below the surface of the 3.6 mm thick sheet.

All measurements were conducted more than a week after welding or laser treatment in order to include the strength recovery by natural aging. However, the measurements were taken over a period of two months. This can affect the base material hardness slightly, as the natural aging process continues after the first week, although not to the same extent as the first few days.

3.3.3 Tensile testing

The specimens with longitudinal laser were statically tested in an MTS Landmark Servohydraulic test machine in the Laboratory for mechanical testing at MTP. The specimens were strained until fracture while logging the force and displacement of the load cell. A displacement rate of 1 mm/min was used for the testing, along with a sampling rate of 50 Hz for logging of the data. The stress is calculated by using the original area of 12.5x3.6 mm^2 for all the specimens, although the exact dimensions of the different specimens may vary slightly. This could affect the accuracy of the stress and strain results but is considered sufficient for the comparison purpose of these tensile tests. The strain is calculated based on the parallel length of the specimens. By using the parallel length as gauge length, there is uncertainty regarding the strain values. Assuming uniform deformation along the gauge length does not take into account that the transition to the wider area, and the unclamped region of the wider area, could deform slightly as well. This is, however, considered adequate for this purpose, as the main objective of these tests is to evaluate the relative strength effect of the different laser powers. The specimens used as references for the laser treated specimens were tested at SINTEF Manufacturing at Raufoss. Extensometers were used for logging the elongation, and the tests were carried out in accordance with the NS-EN ISO6892-1:2016 B standard.

3.3.4 Tensile testing with DIC

Digital image correlation (DIC) was used for the tensile testing of the specimens with cross welds and laser pattern. The static tensile tests were carried out at Sintef Industri at Gløshaugen in a Dartec 500 kN hydraulic testing machine. Two cameras in mono set-up was used to obtain the 2D strain fields on both the front and back side of each specimen. Figure 3.8a shows a tensile specimen in the machine along with the camera in position. Additional lighting was necessary for the camera to focus. A displacement speed of 3.6 mm/min was used for the testing of all specimens. Maximum load and maximum displacement was set to 200 kN and 100 mm respectively. Both cameras was set to a frame-rate of 4 Hz.

A program called eCorr was used for the post-processing of the data from the tensile testing. A mesh of quadratic elements of 20x20 pixels was applied to the parallel region of the specimens, as shown in Figure 3.8b, before running the DIC analyses in eCorr. Three virtual extensometers were placed over the parallel region to obtain the global strains of the specimens, which corresponds to the percent elongation of the vectors, during testing. For each strain value, an average of the three virtual extensometers were used. In order to visualize the strain distribution and localization during testing, field maps of principal strains in the tensile direction were added. This gives the possibility of showing where the strain is most substantial during deformation of the specimens.

The strain evolution of each specimen was evaluated at one surface, more specifically the one with applied cross welds. The second camera in the set-up logged the other surface of the specimen and was mainly for back-up. Since there was only one of each specific specimen, this was very important as lost camera data would mean that the affected specimen was useless for comparison.

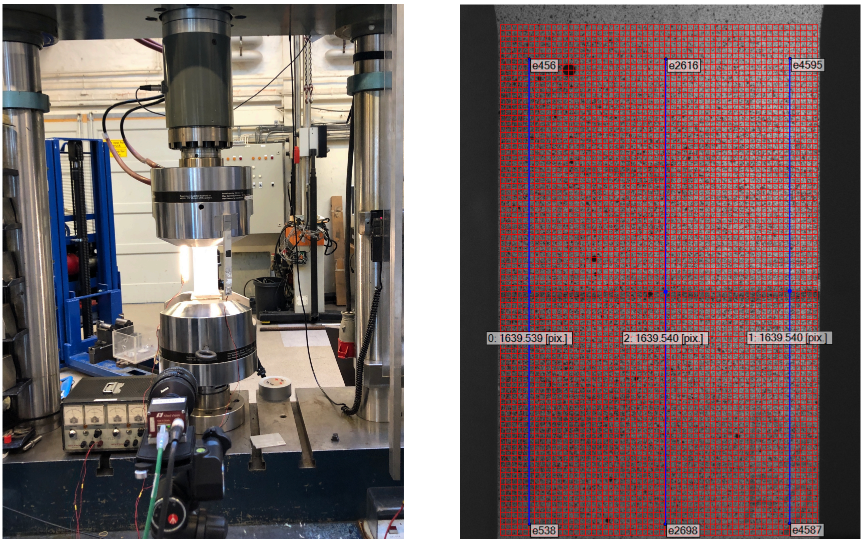

(a) *(b)*

Figure 3.8: *Set-up showing one of the cameras, (a), and post processing with mesh and virtual extensometer, (b), of tensile testing with DIC.*

3.4 Predictions and simulations

3.4.1 Temperature calculations

In this thesis, the Rosenthal medium thick plate solution (Eq. 2.6) is used for estimating the temperature cycle and peak temperatures, due to the weld and laser processes. A software developed by O. R. Myhr allows for easy input of the different parameters of the equation and gives the predicted peak temperature in that given point along with the behavior of the thermal cycle. Parameters such as the current, voltage, speed and efficiency factor of the welding process need to be defined, as well as plate thickness, through thickness depth and distance from the heat source to define the position where the temperature is preferred. The maximum temperature during the welding cycle can be calculated at any point in the cross-section. Figure 3.9 shows an example of input and the corresponding output.

Peak temperatures for both the welding procedure and the laser treatments are calculated. Firstly, the equation was used to estimate the temperature for the GMAW process during the joining of the sheets. The temperature-time cycle and the maximum temperature at several distances from the weld center were calculated. All parameters except the arc efficiency factor of the process were known. During

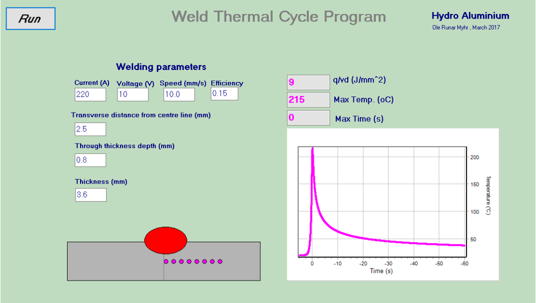

Current (A) 220
Voltage (V) 10
Speed (mm/s) 10.0
Efficiency 0.15
Transverse distance from centre line (mm) 2.5
Through thickness depth (mm) 0.8
Thickness (mm) 3.6
9 q/vd (J/mm^2)
215 Max Temp. (oC)
0 Max Time (s)

Figure 3.9: *Example of input and corresponding output using the software for calculating heat distribution with Rosenthal medium thick plate solution.*

welding, the temperature was measured at several distances from the weld center by thermocouples, as explained in Section 3.2.2. These measurements were used to approximate the efficiency factor by trial and error using Rosenthal medium thick plate solution. The maximum temperatures at the same positions as the thermocouple measurements were estimated for several efficiency factors, and the one that fits best with the measured data was chosen for further temperature estimations in this thesis.

3.4.2 Prediction of hardness

Temperature inputs for the NaMo-simulations regarding welding and laser was calculated using Rosenthal medium thick plate solution. Several simplifications were made in order to simulate the entire temperature history of the material in NaMo. In the current version of NaMo there is a maximum of nine temperature inputs, which is not enough to include the entire temperature history. Figure 3.10a shows a realistic temperature history of extruded 6082 alloys subjected to artificial aging, welding, laser treatment, and post weld heat treatment (PWHT). In order to include the entire thermal history in the NaMo-simulation, several simplifications are required. Dr. Ole Runar Myhr proposed the simplification presented in Figure 3.10b (O.R. Myhr, Personal communication, 2019). The natural aging after extrusion is not included in the simplification, which should be acceptable since the alloy is artificially aged. The cooldown to room temperature from artificial aging temperature is not crucial for the resulting strength as the temperature during aging is too low to cause microstructural changes during cooldown. Therefore, skipping these steps should not affect the results significantly. The same applies to the stages at room temperature between the other elevated temperature steps. The cooldown from the PWHT is also neglected due to the same reasoning. These simplifications were tested for a few simulations as shown in Figure D.1 in Appendix D with a difference in hardness of only 0.8 HV.

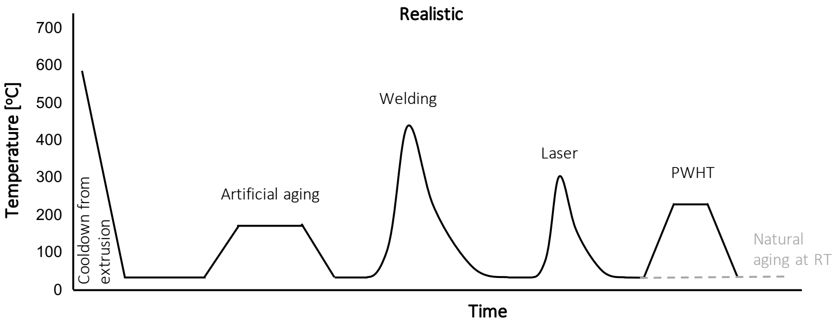

(a)

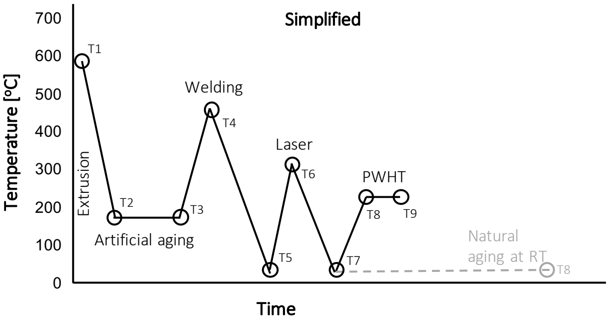

(b)

Figure 3.10: *Diagrams showing (a) a realistic and (b) a simplified temperature history of extruded 6082 alloys subjected to artificial aging, welding, laser and PWHT/natural aging at room temperature (RT) (O.R. Myhr, Personal communication, 2019).*

The predicted peak temperature from both weld and laser needed to be calculated for each point along the cross-section, to predict the resulting strength and hardness. Since the laser position is at 8.5 mm from weld center, a distance 6 mm from the weld center would correspond to 2.5 mm from the laser center. All peak temperature estimations due to the weld and the laser are given in Table 7 in Appendix E.

4 Results

The results of the characterization, mechanical testing, and predictions are all presented in this chapter. Optical micrographs and hardness profiles of the GMA weld are presented before the results from tensile testing regarding the different local heat treatments are given. These results are presented in the same order as in the preceding chapter; cross welds, longitudinal laser in HAZ and laser pattern (see Figure 3.1 in Section 3.2.1). The notation PWHT indicates that the specimens have been subjected to a post weld heat treatment at 220 °C for 15 minutes. Lastly, the predicted peak temperatures and hardness simulations are presented.

4.1 Characterization of the weld

4.1.1 Microstructure

A cross-section of the base material is shown in Figure 4.1a, where the extrusion direction is along the horizontal axis. The grain structure is fibrous in most of the cross-section area, which is expected for extruded profiles of this alloy. The microstructure close to and along the surfaces of the sheet are not fibrous which indicates recrystallization has occurred.

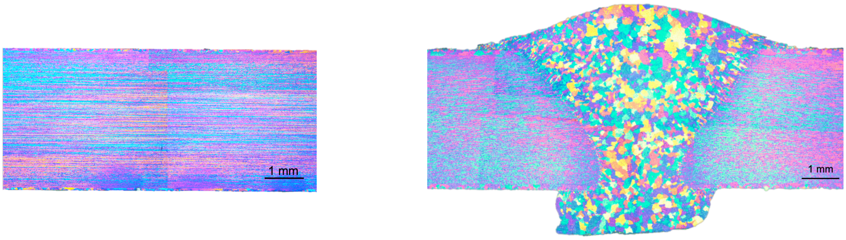

(a) *(b)*

Figure 4.1: *Optical micrographs of (a) the base material perpendicular to the extrusion direction and (b) the weld cross-section of welding speed 16 mm/s. The base material shows a fibrous grain structure, while the weld shows the recrystallized fusion zone.*

Figure 4.1b, 4.2a and 4.2b shows the microstructure of the cross-section of welds produced by three different welding speeds: 16 mm/min, 14 mm/min and 18 mm/min respectively. All welds have a grain structure similar to an as-cast state in the fusion zone, and the grains along the fusion line are slightly equiaxed and extends into the fibrous structure of the parent material. The cross-sections are perpendicular to the fibrous structure as the extrusion direction is out-of-plane.

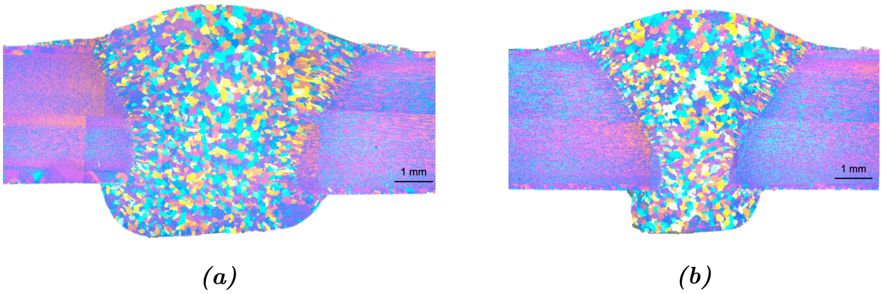

(a) (b)

Figure 4.2: *Optical micrographs of weld cross-section of weld speed (a) 14 mm/s and (b) 18 mm/s showing the recrystallized fusion zone.*

The size of the fusion zone differs for the three welds, where higher speed resulted in a smaller fusion zone, but the grain size is similar.

4.1.2 Hardness profiles

Hardness profiles are given in this section, and illustrations below the graphs show where in the cross-section the measurements were made. The hardness profiles of the GMA weld produced with a welding speed of 16 mm/s are plotted in Figure 4.3. Hardness measurements are taken of similar welds both with and without a PWHT. The grey curve shows the hardness profile of the weld without PWHT where the minimum hardness of the HAZ can be found at about 8-9 mm from the weld center. The lowest hardness is observed in the weld metal, while the minimum hardness values in the HAZ are 65.9 and 65.2 HV. In the region between the fusion zone and the hardness drop in the HAZ, the hardness is increased. The base material hardness is reached at approximately 17 mm from weld center, which defines the width of the HAZ. The blue hardness profile in Figure 4.3 is the hardness profile of a similar weld with 16 mm/s weld speed, but with a PWHT. It is similar to the one of the weld without PWHT, but experience a more significant increase in hardness close to the weld, and the base material hardness is lower due to overaging.

Figures 4.4a and 4.4b show the hardness profiles of sheets welded by GMAW at 14 mm/s and 18 mm/s weld speed, respectively. The lowest measured hardness in the HAZ is relatively similar for the two cases, but the width of the HAZ is significantly smaller for the faster weld speed. The HAZ extends about 18 mm for the weld of 14 mm/s compared to 13 mm for the 18 mm/s weld.

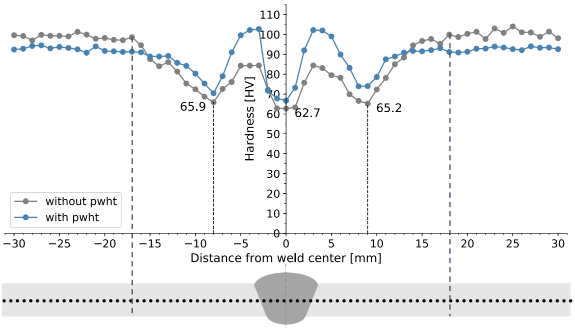

Figure 4.3: *Hardness profiles of the weld cross-section for single-sided GMA joining weld at 16 mm/s welding speed. The extent of the HAZ is indicated with dashed lines.*

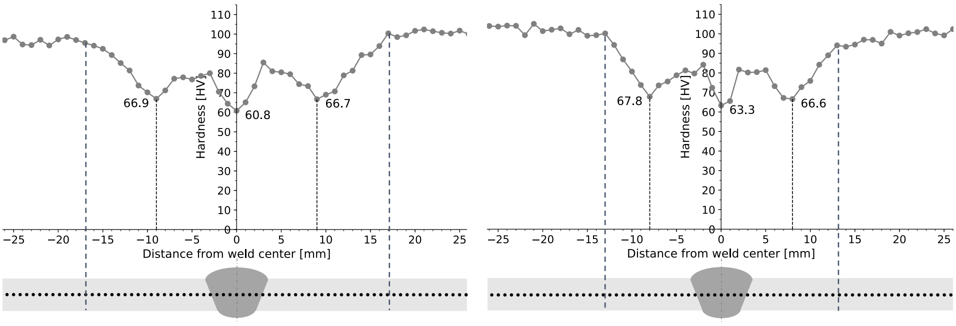

(a) ***(b)***

Figure 4.4: *Hardness profiles of the cross-sections of single-sided gas metal arc joining welds at weld speeds of (a) 14 mm/s and (b) 18 mm/s. The extent of the HAZ is indicated with dashed lines.*

4.2 DIC tensile test results of cross welded specimens

4.2.1 Stress-strain behavior

The results from the tensile testing of the cross welded specimens are presented here and in the following sections. The stress-strain curves for the specimens without PWHT are plotted in Figure 4.5, while Figure 4.6 presents the curves for the specimens with PWHT. The stress-strain curves are obtained by the calculated engineering stress based on the logged force and initial area and the percent elongation of the virtual extensometers applied in the DIC post-processing. The evolution of the strain distribution during the tensile test are given by field maps of principal strains obtained by the DIC software. All the fractured specimens tested with DIC are given in Appendix G.

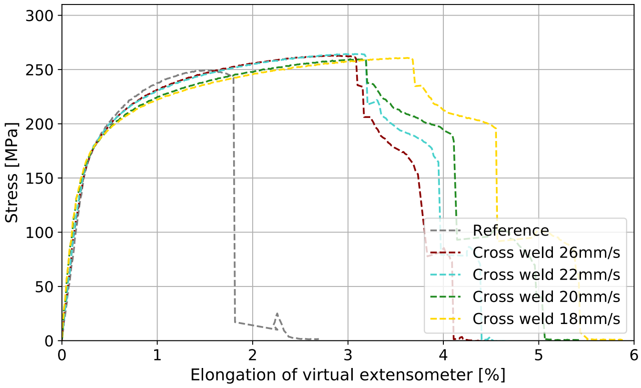

Figure 4.5: *Stress-strain curves of specimens with cross welds and without PWHT.*

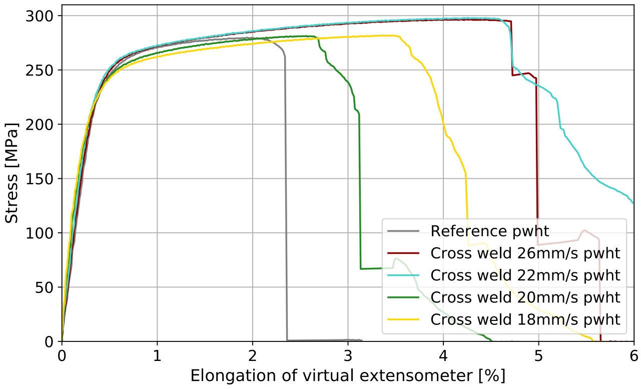

Figure 4.6: *Stress-strain curves of specimens with cross welds and PWHT.*

A summary of the properties obtained by the stress-strain curves is given in Table 5. The calculated 0.2 % proof strength (referred to as the yield strength in this thesis), $R_{p0.2}$, ultimate tensile strength, R_{UTS}, and strain (percent elongation) at fracture, e_f, are presented for each specimen with cross welds along with the reference specimens.

Table 5: *Relevant values from the stress-strain curves presented above, and the cross weld (CW) speed is indicated in the description.*

Description		Yield strength, $R_{p0.2}$ $[MPa]$	Tensile strength, R_{UTS} $[MPa]$	Strain at fracture, e_f [%]
Reference	No PWHT	200.5	249.5	1.8
	PWHT	252.0	279.7	2.34
18 mm/s CW	No PWHT	191.2	260.9	3.68
	PWHT	245.3	281.8	3.57
20 mm/s CW	No PWHT	193.2	259.6	3.19
	PWHT	246.9	281.3	2.7
22 mm/s CW	No PWHT	198.8	264.4	3.18
	PWHT	255.6	298.2	4.7
26 mm/s CW	No PWHT	199.0	262.9	3.08
	PWHT	256.1	296.6	4.7

4.2.2 Reference specimens

Figures 4.7a and 4.7b shows the evolution of the principal strain for the reference specimens without and with PWHT. Both specimens deform in a similar matter, where strain localization occurs in the HAZ on both sides of the weld and causes necking, before further deformation continuous on one side until rupture occurs. The specimen with PWHT has an ultimate tensile strength of 279.7 MPa compared to 249.5 MPa for the specimen without PWHT. The reference with PWHT fractures at 1.8 %, while the specimen without fractures at 2.34 %.

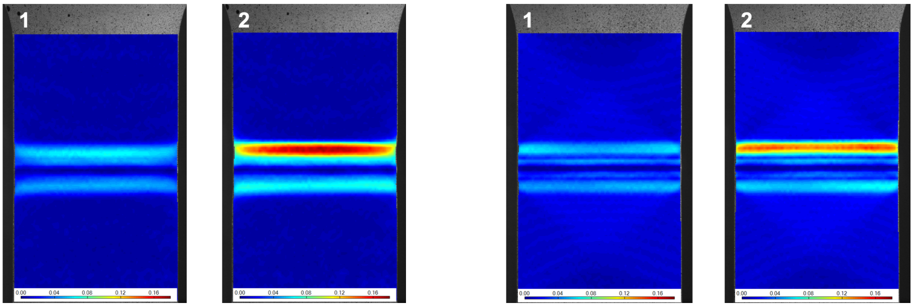

(a) *(b)*

Figure 4.7: *Evolution of principal strain localization during tensile testing of reference specimens (a) without PWHT and (b) with PWHT.*

4.2.3 Cross weld speed 18 mm/s

The stress-strain curves of the specimens with cross weld speed of 18 mm/s are plotted in Figures 4.5 and 4.6. Compared to the reference specimens, the cross welded specimen without PWHT exhibit a lower yield strength, but about 11 MPa higher ultimate tensile strength. The specimen with PWHT shows similar decrease in yield strength and only 2 MPas increase in tensile strength. The plastic deformation prior to fracture is significantly larger for both specimens at 3.68 % and 3.57 % for the one with and without PWHT respectively.

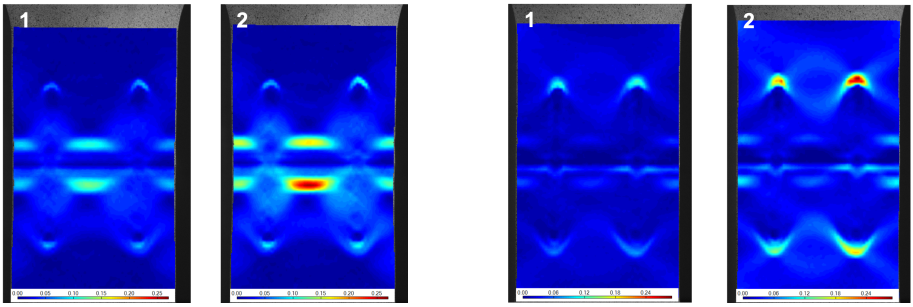

(a) *(b)*

Figure 4.8: *Evolution of principal strain localization during tensile testing of specimens with cross weld speed 18 mm/s (a) without PWHT and (b) with PWHT.*

Figure 4.8 shows how the localization of principal strain develops during deformation. For the specimen without PWHT, the strain localizes in the HAZ on both sides between the two cross welds, and fracture occurs along the HAZ. Figure 4.9 shows how the crack propagates after the first crack is initiated where the strain localized.

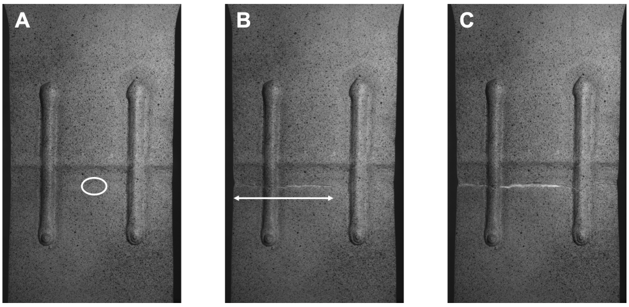

Figure 4.9: *Fracture of specimen with cross weld speed 18 mm/s, without PWHT.*

The specimen with PWHT hardly experience any deformation in the minimum strength HAZ, as can be seen in Figure 4.8b. The strain localized outside the tips/ends of the cross welds, 35-40 mm from the weld center, thus outside of the HAZ. Figure 4.10 shows that the crack is initiated at the tip of one cross weld and propagates horizontally towards the other cross weld before reaching the edges and final rupture occurs.

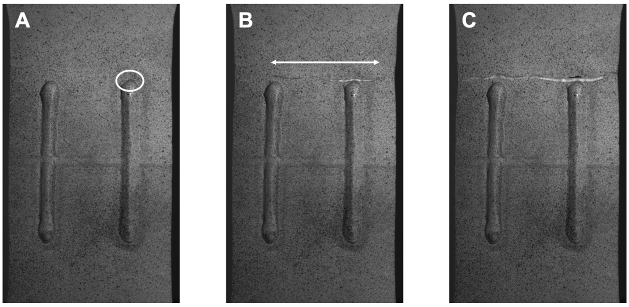

Figure 4.10: *Fracture of specimen with cross weld speed 18 mm/s, with PWHT.*

4.2.4 Cross weld speed 20 mm/s

The behavior of the specimens with 20 mm/s cross welds are similar to the specimens with 18 mm/s cross welds. Compared to the reference specimens, a decrease in yield strength and an increase in ultimate tensile strength is observable. The specimens with and without PWHT fracture at strains of 2.7 % and 3.19 % respectively.

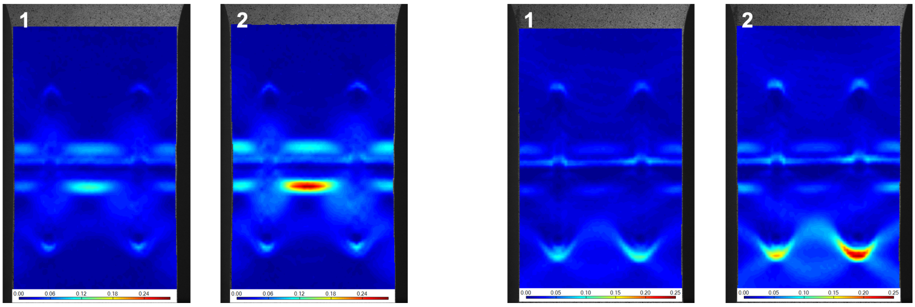

(a) *(b)*

Figure 4.11: *Evolution of principal strain localization during tensile testing of specimens with cross weld speed 20 mm/s (a) without PWHT and (b) with PWHT.*

The strain localizes in similar locations as for the specimens with 18 mm/s cross welds (Figure 4.11), and the cracks are initiated and propagating in the same manner, as can be seen in Figure 4.12 and 4.13.

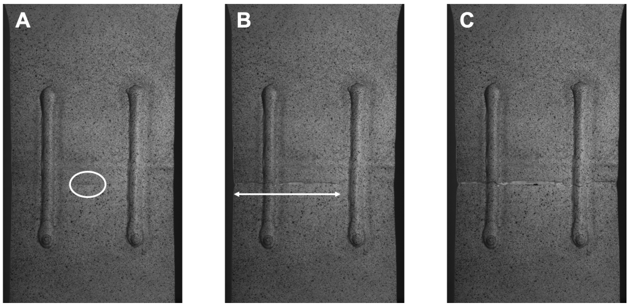

Figure 4.12: *Fracture of specimen with cross weld speed 20 mm/s, without PWHT.*

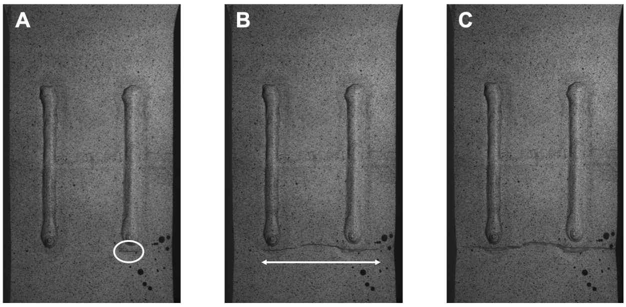

Figure 4.13: *Fracture of specimen with cross weld speed 20 mm/s, with PWHT.*

4.2.5 Cross weld speed 22 mm/s

The specimen without PWHT experienced an increase of 15 MPa in ultimate tensile strength compared to the the reference specimen, and only a small decrease in yield strength. The specimen with PWHT shows a significant increase in ultimate tensile strength of approximately 19 MPa, as well as a slight increase in yield strength compared to the PWHT reference specimen. The elongation prior to fracture for the specimen with PWHT is 4.7 % which is significantly larger than the reference specimen.

Figure 4.14 shows how the strain field changes during deformation. The specimen without PWHT experience strain concentration in the HAZ and the first crack is initiated between the two cross welds on one side of the weld. The crack propagates along the HAZ as seen in Figure 4.15. The specimen with PWHT, however,

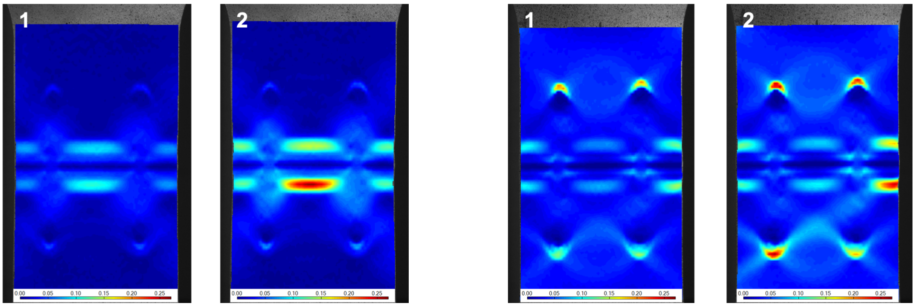

(a) *(b)*

Figure 4.14: *Evolution of principal strain localization during tensile testing of specimens with cross weld speed 22 mm/s (a) without PWHT and (b) with PWHT.*

experience strain concentration at several places; both in the HAZ and at the tips of the cross welds. The first visible crack is observed at the tip of one of the cross weld, while another crack occurs in the HAZ close to the edge. The crack then propagates between the two cracks, followed by the final fracture, as seen in Figure 4.16.

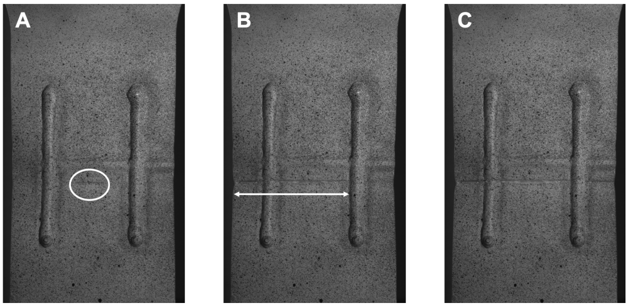

Figure 4.15: *Fracture of specimen with cross weld speed 22 mm/s, without PWHT.*

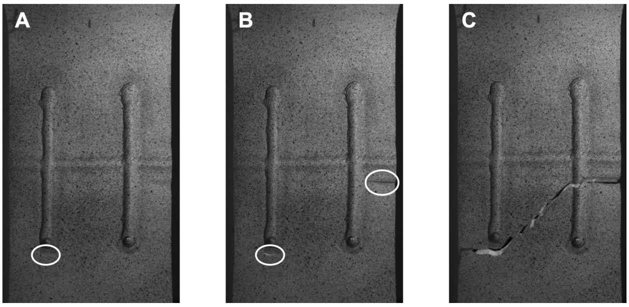

Figure 4.16: *Fracture of specimen with cross weld speed 22 mm/s, with PWHT.*

4.2.6 Cross weld speed 26 mm/s

Compared to the reference specimen, the 26mm/s cross weld specimen without PWHT exhibit an increase in ultimate tensile strength and a small decrease in yield strength. The specimen with PWHT shows a behavior similar to the specimen 22 mm/s cross weld, with a large increase in ultimate tensile strength, a slight increase in yield strength and 4.7 % elongation prior to fracture.

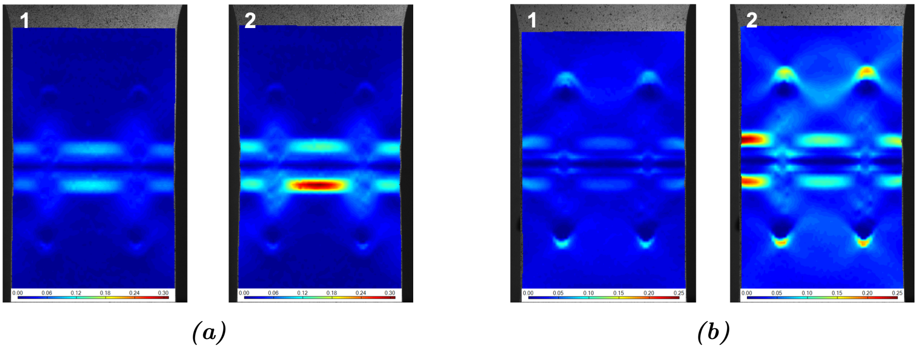

(a) *(b)*

Figure 4.17: *Evolution of principal strain localization during tensile testing of specimens with cross weld speed 26 mm/s (a) without PWHT and (b) with PWHT.*

Figure 4.17 shows how the strain localizes during tensile testing. Necking and fracture occur in the HAZ between two cross welds for the specimen without PWHT, as seen in Figure 4.17a and 4.18. Strain localizes in several places for the specimen with PWHT, similar to the 22 mm/s cross welded specimen with PWHT. Figure 4.17b shows how the strain localizes in the lowest strength region of the HAZ, only interrupted by the cross welds, and outside the tips of the cross welds. The first crack occurs at the edge of the specimen in the HAZ and fractures along this line, as shown in Figure 4.19.

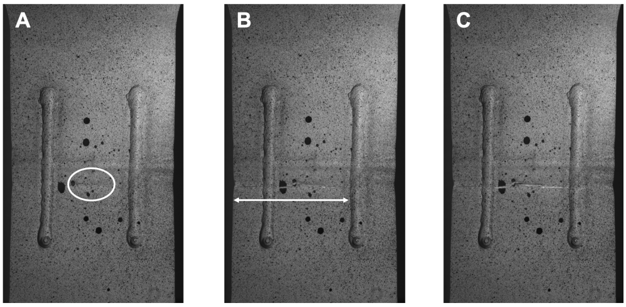

Figure 4.18: *Fracture of specimen with cross weld speed 26 mm/s, without PWHT.*

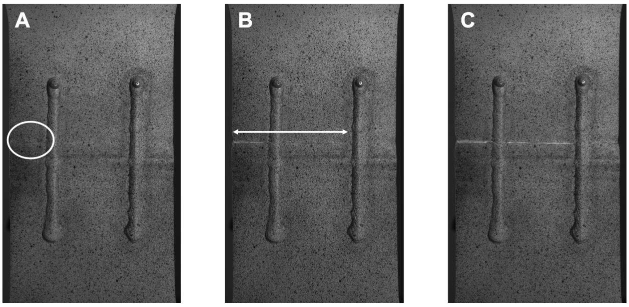

Figure 4.19: *Fracture of specimen with cross weld speed 26 mm/s, with PWHT.*

4.3 Results of longitudinal laser

4.3.1 Hardness profiles

The hardness measurements of the welded specimens with longitudinal laser 8.5 mm from the weld center are presented in this section. The laser passed on each side of the weld on both the upper surface and the lower surface. Figure 4.20, 4.21, and 4.22 shows hardness profiles along the cross-sections of the laser treated welded specimens. The positions of the laser treatment are indicated by the blue semicircles, while the location of the measurements are indicated by black dotted lines on the cross-section illustration.

The hardness profile of the specimen with 2000 W laser treatment is given in Figure 4.20. The measurements in Figure 4.20b show that the specimen with laser is similar to the reference specimen without laser at 1.8 mm beneath the surface, which indicates that the laser did not change the properties in the middle of the sheet. The PWHT increased strength close to the fusion zone similar to what is observed for the weld without laser (see Figure 4.3 in Section 4.1.2). The measurements at 0.8 mm from the surface (Figure 4.20a) show similar behavior as the measurements at 1.8 mm, except for the hardness values at 9 mm from weld center. This is 0.5 mm from the applied laser. At this position, the specimen with laser treatment and without PWHT experiences a drop in hardness, while the measurements without laser remain unaffected. The specimen with both laser and PWHT show an increased hardness value at this position.

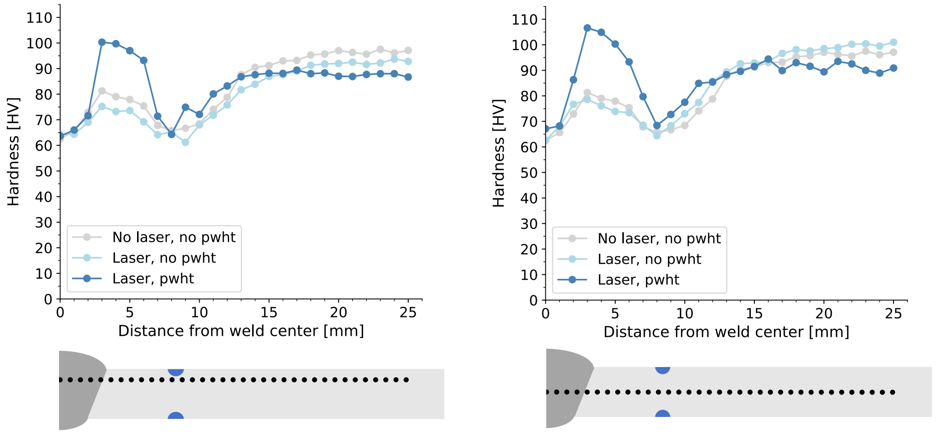

(a) *(b)*

Figure 4.20: *Hardness profiles at positions beneath the surface of (a) 0.8 mm and (b) 1.8 mm of specimens with 2000 W longitudinal laser.*

The hardness profiles of the sheet with 2200 W laser treatment is plotted in Figure 4.21. The profiles of 1.8 mm beneath the surface, as shown in Figure 4.21b seems relatively unaffected by the laser. The curve of the specimen with laser and without PWHT shows a decrease in the region 3-5 mm from the weld center, which could be due to the laser heat cycle. The measurements at 0.8 mm shown in Figure 4.21a shows the expected drop at 8-9 mm from weld center with an increase in hardness close to the fusion zone. This zone of lower hardness is wider for these measurements than for the measurements 1.8 mm beneath the surface. A slight drop is observed at 12 mm from the weld center corresponding to 3.5 mm from the laser position. The PWHT increased the hardness further in the zone close to the fusion zone with similar increase as the observed in Figure 4.3 in Section 4.1.2.

The laser power of 2600 W caused notable changes in the hardness profile, as seen from Figure 4.22. There is a significant drop in hardness at about 12-13 mm from the weld center. This corresponds to about 3-4 mm from the laser position, and a similar effect is observed at the other side of the laser closer to the weld at 5 mm from weld center. These changes in the hardness profile are observable where the laser caused significant melting, as seen in Figure H.1 in Appendix 8.

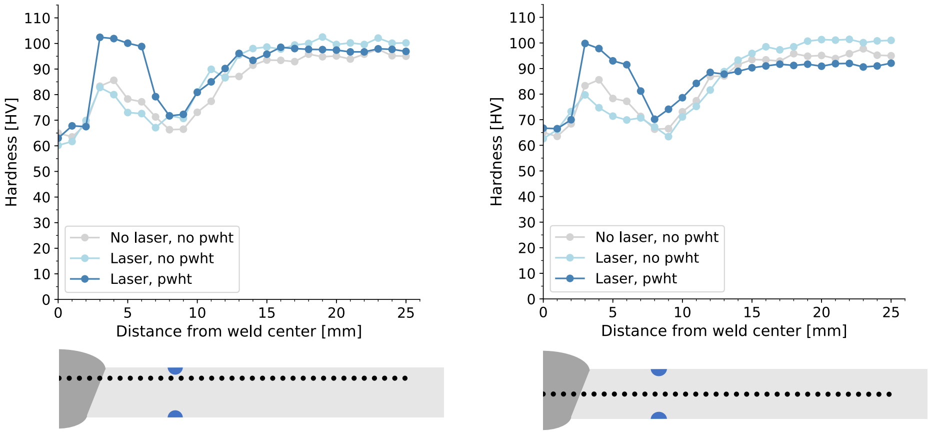

(a) *(b)*

Figure 4.21: *Hardness profiles at positions beneath the surface of (a) 0.8 mm and (b) 1.8 mm of specimens with 2200 W longitudinal laser.*

The measurements at both 0.8 mm and 1.8 mm beneath the surface crossed the melted region, which explains the wide region of reduced hardness around the laser position.

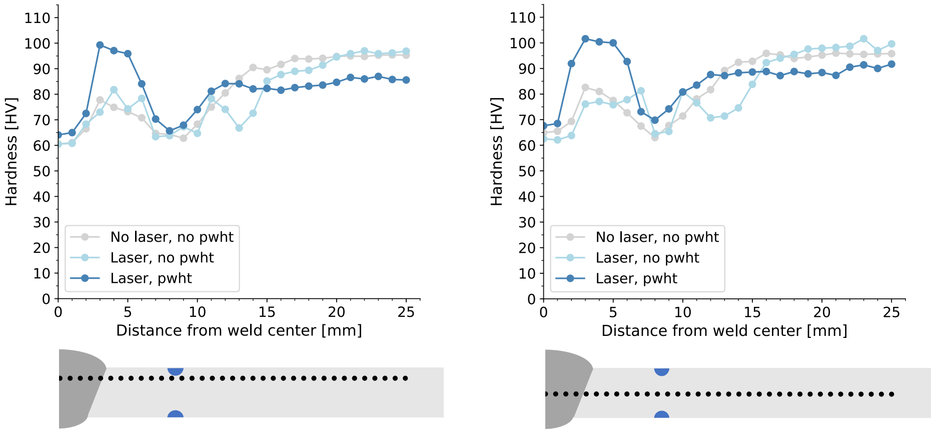

(a) *(b)*

Figure 4.22: *Hardness profiles at positions beneath the surface of (a) 0.8 mm and (b) 1.8 mm of specimens with 2600 W longitudinal laser.*

4.3.2 Tensile test results

The results from the tensile testing of the welded sheets with laser in the HAZ parallel to the weld, are plotted in stress-strain curves below. Firstly, the reference specimens are presented in Figure 4.23. Then, the stress-strain curves of the specimens with laser and PWHT are given in Figures 4.24, 4.25 and 4.26 for the laser powers of 2000 W, 22000 W and 2600 W respectively. The reference specimen results are plotted separately as they were tested with extensometers, while the ones with laser were not. The main focus of comparison is the ultimate tensile strength, since properties such as yield strength and elongation are not directly comparable due to the difference in test set-up.

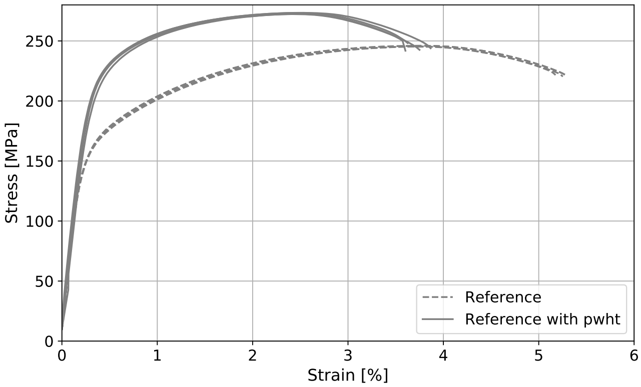

Figure 4.23: *Stress-strain curve of reference specimens with and without PWHT, where there are four specimens of each.*

Figure 4.23 shows the tensile test results for the reference specimens. The welded specimens without PWHT yielded at an average stress of 173.9 MPa and obtained an average ultimate tensile strength of 245.9 MPa. The PWHT resulted in a decrease in elongation, but a significant increase in both yield strength and ultimate tensile strength with average values of 228.5 MPa and 272.9 MPa respectively.

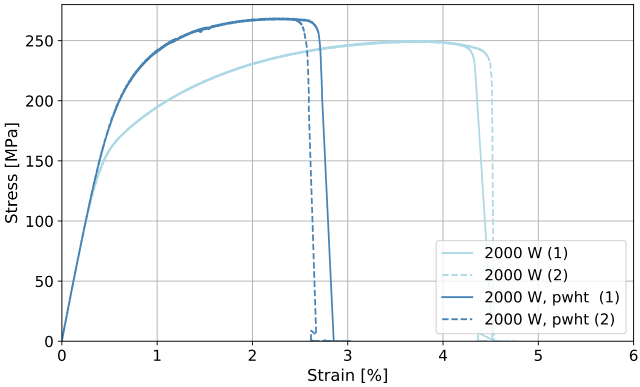

Figure 4.24: *Stress-strain curve of specimens with 2000 W longitudinal laser treatment in HAZ.*

Figure 4.24 shows the stress-strain curve of a GMA welded sheet with 2000 W laser treatment and PWHT. The specimens with laser and without PWHT show a small increase in ultimate tensile strength of 4 MPa and withstands less deformation after the point of necking compared to the reference specimen. The PWHT increased strength and reduced the ductility significantly, similarly to the reference specimens. However, the ultimate tensile strength is lower, and a larger decrease in elongation is observed.

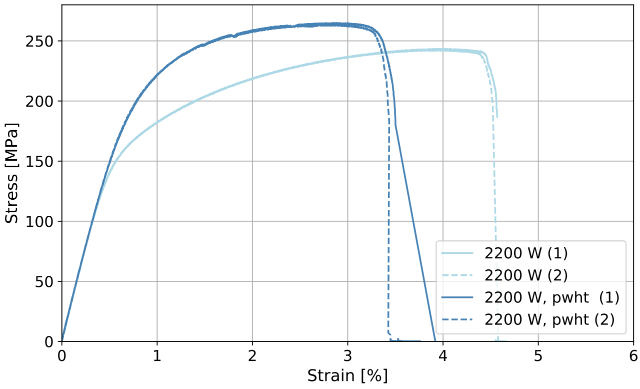

Figure 4.25: *Stress-strain curve of specimens with 2200 W longitudinal laser treatment in HAZ.*

In Figure 4.25, the stress-strain curves of sheets with 2200 W laser treatment are plotted. There is a clear difference for the specimens with and without PWHT, with increased strength and reduces ductility. The laser treated specimens both with and without PWHT exhibit lower ultimate tensile strength compared to their respective references.

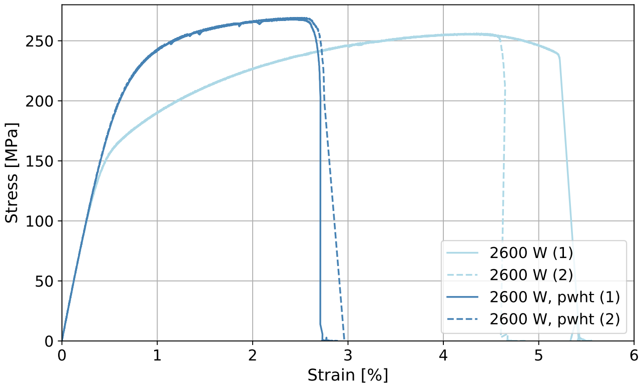

Figure 4.26: *Stress-strain curve of specimens with 2600 W longitudinal laser treatment in HAZ.*

The stress-strain curve of specimens with laser treatment of 2600 W is presented in Figure 4.26. The specimens with laser and PWHT show similar behavior of the specimen with 2000 W laser treatment, hence slightly lower strength than the reference. The laser treated specimen without PWHT, however, obtains an ultimate tensile strength increase of 10 MPa compared to the reference specimen. Both specimens obtained similar strength values with a large elongation prior to fracture. One of the two specimens fractured at 14 mm from the weld center, which corresponds to the drop in hardness observed in Figure 4.22.

To summarize the results of the longitudinal laser treatment in HAZ, the tensile properties obtained by the stress-strain curves are given in Table 8 in Appendix H. The average ultimate tensile strengths obtained for the different specimens are given in Table 6. The PWHT generally increased the strength and reduced the ductility of all specimens regardless of laser treatment, and all specimens except one, fractured in the minimum level HAZ at approximately 8-9 mm from weld center.

Table 6: *The average ultimate tensile strength, R_{UTS}, of specimens with laser treatment in HAZ.*

Description	Average ultimate tensile strength [MPa]
Reference	245.9
Reference, pwht	272.9
2000 W	250.0
2000 W, pwht	268.6
2200 W	243.0
2200 W, pwht	264.2
2600 W	256.0
2600 W, pwht	268.8

4.4 Results of laser pattern

4.4.1 Hardness profiles

The hardness profiles over the cross-section of the welded sheet with laser pattern are shown in Figure 4.27. The 2000 W laser pattern was applied to both the upper and the lower surface, and the hardness is measured at three locations over the thickness of the sheets, at 0.8 mm, 1.8 mm and 2.8 mm below the surface of the 3.6 mm thick sheets. This is indicated by the black dotted lines, and the blue semicircles illustrate the positions of the laser lines.

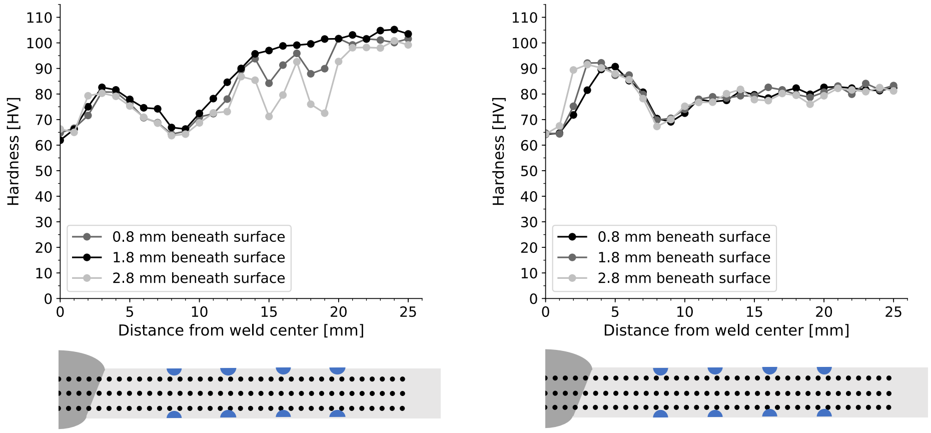

(a) ***(b)***

Figure 4.27: *Hardness profiles of specimens with laser pattern, where (a) is without PWHT and (b) is with PWHT.*

Figure 4.27a shows the hardness profile of a specimen without PWHT. The hardness profile measured along the center of the thickness, 1.8 mm below the surface, is unaffected by the laser and shows similar behavior as the weld without laser in Figure 4.3. A drop in hardness due to the three outer laser lines is observed 0.8 mm and 2.8 mm below the surface, while the remaining hardness profile is similar to the hardness along the middle of the thickness. The laser pattern on the lower surface of the sheet resulted in a larger hardness reduction than the ones on the upper surface of the sheet.

The hardness profile of the specimen with PWHT is shown in Figure 4.27b. The reduction in hardness due to the laser is less apparent here, but the overall base material hardness is reduced significantly. The lowest hardness in the HAZ at 8 mm from the weld center is slightly higher but is still the lowest hardness. It should be noted that the PWHT for the specimen with the laser pattern was not conducted together with the other specimens with PWHT in this report. The significant decrease in base material hardness indicates that overaging occurred to a greater extent than the other PWHT specimens, and this is further discussed in Chapter 5.

4.4.2 DIC tensile test results

The stress-strain curve of the specimens with laser pattern are plotted in Figure 4.28. The specimen without PWHT obtains similar strength levels as the reference specimens but improved elongation at fracture. The specimen with PWHT shows an even larger increase in elongation and fractured at 3.3 %. However, no increase in ultimate tensile strength is observed and the yield strength is reduced slightly.

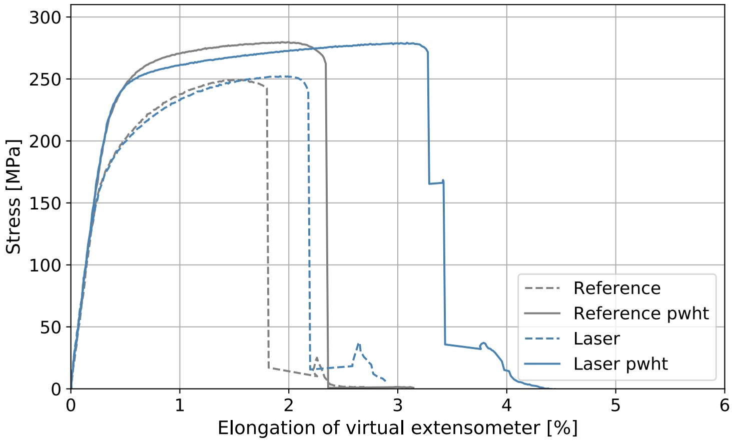

Figure 4.28: *Stress-strain curves of specimens with laser pattern.*

The evolution of principal strain shows that the strain localizes in the HAZ on both sides of the weld for both specimens, as seen in Figure 4.29. For the specimen without PWHT, the deformation is large in the minimum level HAZ over the entire width of the specimen and is not interrupted by the laser pattern. This is evident from the fracture propagation in Figure 4.30a, which shows how the first and final rupture occurs.

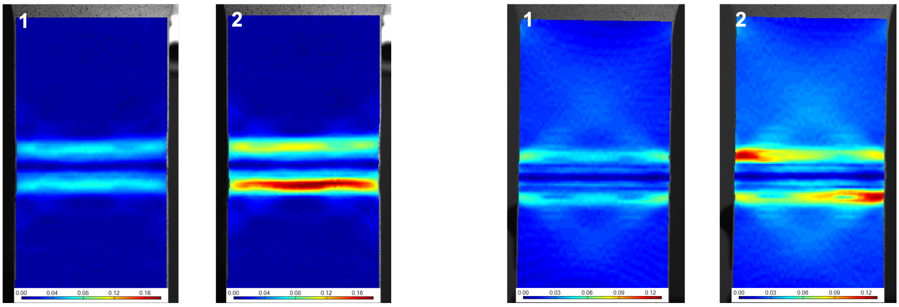

(a) *(b)*

Figure 4.29: *Evolution of principal strain localization during tensile testing of specimens with laser pattern, where (a) is without PWHT and (b) is with PWHT.*

Figure 4.29b shows how the strain localizes in the HAZ by the edges of the specimen on both sides for the specimen with PWHT. The pattern of the laser is visible as blue lines in the strain field, which means less deformation occurred in this area. The first crack is initiated along the right edge of the specimen, as indicated by the white circle in Figure 4.30b. Then the crack grows rapidly along the HAZ before the final fracture occurs.

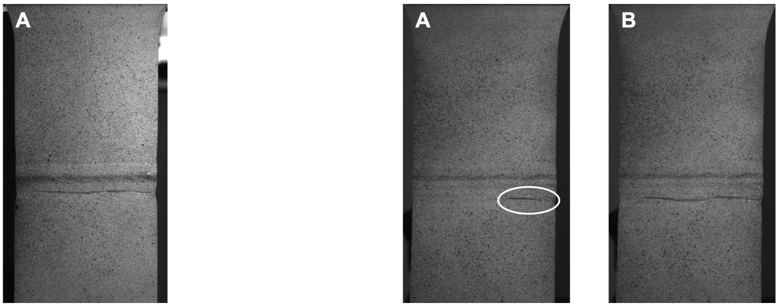

(a) *(b)*

Figure 4.30: *Crack propagation during tensile testing of specimens with laser pattern, where (a) is without PWHT and (b) is with PWHT.*

4.5 Predictions and simulations

4.5.1 Thermal cycle of welding

The peak temperature at different distances from the weld center was calculated for several arc efficiency factors of the welding process. These predictions are plotted against the thermocouple values measured during welding in Figure 4.32. The efficiency factor, η, for the peak temperature predictions that best comply with the measured data is 0.7 as seen from the continuous blue line the figure. The continuous line represents the values estimated by Rosenthal medium thick plate solution, while the points are maximum temperatures measured by thermocouples. The efficiency factor of η =0.7 is a realistic estimate as the efficiency factor for GMA welding on aluminium is usually between 0.7 and 0.85 [28]. Figure 4.31 shows the predicted thermal cycles plotted together with the measured thermocouple cycles. The fit of the estimated curve compared to the measured temperature is considered adequate, and η =0.7 was chosen for further temperature estimations in this thesis.

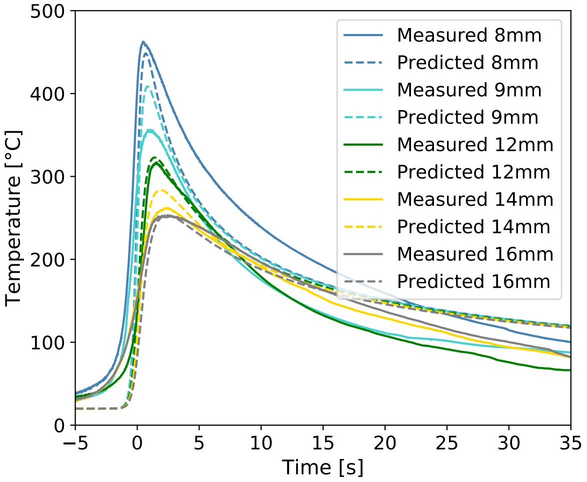

Figure 4.31: *Predicted and measured thermal cycles for single pass GMA weld with v = 10 mm/s and q_0 = 3221 W at different distances form the weld center.*

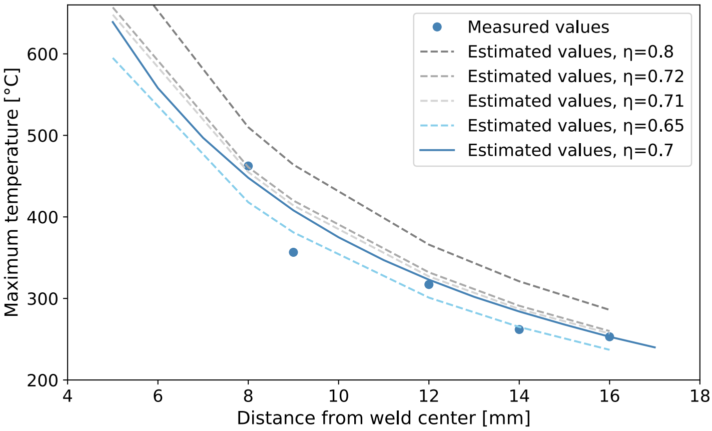

Figure 4.32: *Predicted peak temperatures with several efficiency factors plotted together with measured thermocouple data.*

4.5.2 Hardness profiles predicted by NaMo

Figure 4.33 shows the hardness values predicted by NaMo plotted together with the measured hardness profile of a weld with the same welding parameters. Each point in the curve corresponds to a simulation based on the calculated temperature history for that specific position in the cross-section area. The simulations were tuned to match the base material strength before any additional heat cycles due to weld, laser of PWHT were added.

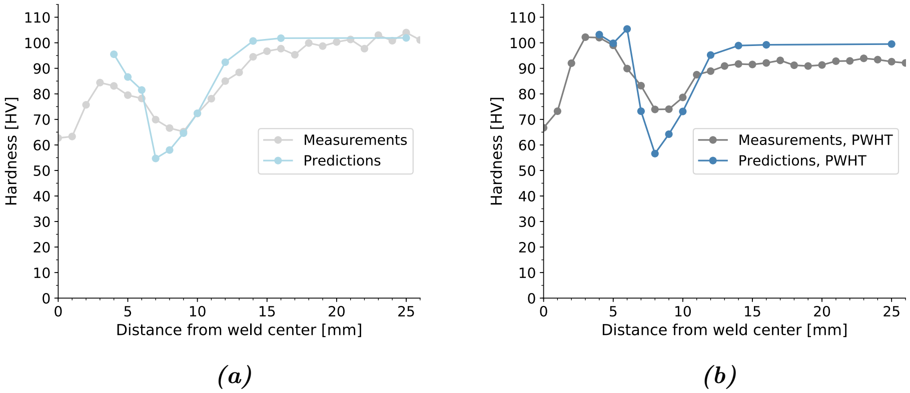

(a) *(b)*

Figure 4.33: *Comparison of measured and predicted hardness profiles of welded specimens, where (a) is without PWHT and (b) is with PWHT.*

The prediction curves for hardness both with and without PWHT, Figure 4.33b and 4.33a respectively, follow the measured hardness profile with an increase outside the fusion zone followed by a large drop before increasing until base material hardness is reached. According to Figure 4.33a, NaMo predicts the drop due to the thermal cycle of welding to be at 7 mm from the weld center with a larger decrease in hardness compared to the measured values. The natural aging between the drop and the fusion line is slightly overestimated, while the extent of the HAZ is precisely predicted. For the simulations with PWHT in Figure 4.33b, the aging is accurately predicted, but the hardness drop is overestimated. The width of the HAZ is accurately simulated, while the base material hardness is slightly overestimated.

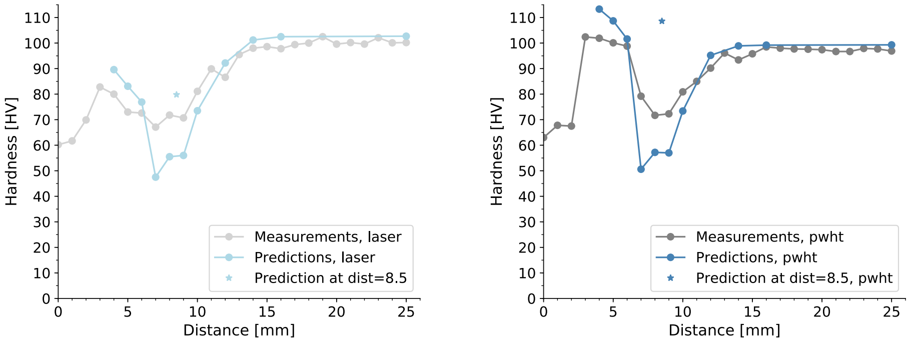

(a) *(b)*

Figure 4.34: *Comparison of measured and predicted hardness profiles welded specimens with 2200 W longitudinal laser treatment in HAZ, where (a) is without PWHT and (b) is with PWHT.*

Predicted and measured data of the HAZ with 2200W laser treatment 8.5 mm from weld center are plotted together in Figure 4.34 for comparison. All estimated peak temperatures and hardness values for each simulation are given in Table 7 in Appendix E. The lowest hardness in the HAZ is in a region at 7-9 mm from the heat source. Both simulations with and without PWHT predicts a large reduction due to the thermal cycle of the laser, with an additional drop at 7 mm. The measured hardness profile without PWHT (Figure 4.34a) additionally indicates a reduction at 5 mm and 12 mm from the weld center which corresponds to 3.5 mm from the laser center on each side. This effect is not registered for the predicted hardness profile and not for the specimen with PWHT in Figure 4.34b. However, the simulations at 8.5 mm from weld center, i.e., at the position of the laser, predicts a large increase in hardness similar to the aging close to the fusion line. This effect is predicted for both cases with and without PWHT but is not observed in measurements.

5 Discussion

5.1 Introductory remarks

In the following chapter, relevant findings and results are discussed. Firstly, the degradation of mechanical properties in the joining gas metal arc weld are assessed. Then, the results of mechanical testing regarding the local heat treatments are evaluated, where important findings are highlighted and possible explanations are discussed. Lastly, the accuracy of predicted values regarding both temperature and hardness estimations are evaluated.

5.2 Mechanical properties of the weld

5.2.1 Degradation of properties in the HAZ

The hardness profiles in Figure 4.3 in Section 4.1.2 show a characteristic behavior of welded 6082-T6 alloys. The hardness is overall lower in the HAZ than the base material hardness as expected. The increased hardness outside the fusion zone is due to natural aging. This occurs in the region where the temperature during was sufficiently high to cause full reversion of the strengthening β'' particles which allows for reprecipitation by aging. Even more strength is regained by artificial aging during the post weld heat treatment as evident from the hardness profile. The lowest hardness observed for the weld with weld speed 16 mm/s is 65.2 HV at 9 mm from weld center, which corresponds to about 64% of the base material hardness, thus a significant reduction. The hardness values can be translated into an equivalent ultimate tensile strength by Eq.2.12, which gives a minimum tensile strength value that is 69% of the base material strength. This is slightly higher than the expected reduction factor, ρ_{HAZ}, of 0.65 as suggested for GMA welding of Al-Mg-Si alloys [13], as stated in Chapter 2. The PWHT mainly increased the strength in the HAZ region with Mg and Si in solid solution, but the lowest level hardness does experience a small increase as well.

5.2.2 Strength of reference specimens

The tensile tests perpendicular to the weld were conducted with two different tensile specimens with regards to geometry and dimensions. Due to this, a direct comparison of the different local heat treatments (eg. laser and cross welds) are not recommended. However, the relative changes in material properties compared to reference specimens of equal dimension are highly relevant to account for the possible of effects of these treatments.

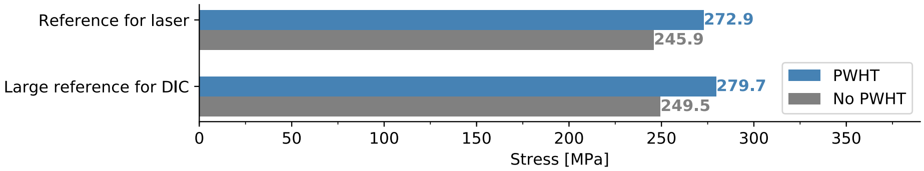

Figure 5.1: *Comparison of the ultimate tensile strengths of the reference specimens from the two different tensile test set-ups. The value for the reference for laser is based on an average of four specimens.*

The maximum stress level observed is valid for comparison between the different specimens and test set-ups. The reference specimens used for the DIC testing and the reference specimens for the laser treatment show similar characteristics. Figure 5.1 shows the ultimate tensile strength of the two different tensile test specimens side by side. As seen from the bar plot, the two specimens without PWHT exhibited a tensile strength just below 250 MPa, where the larger specimen reached a maximum at a few MPs higher. The same trend is evident for the specimens with PWHT, where the larger specimen reaches a higher maximum at 279.7 MPa compared to 272.9 MPa. This could be a result of several factors, such as differences in weld quality or the large difference in specimen size. The latter is considered more likely, as the welding parameters are equal and the sheets are from the same extruded profile with equal thermomechanical history. The cross-section area of the DIC specimens is five times larger than the smaller specimens. The thickness is 3.6 mm for both, which means the geometry is very different. Since the HAZ consists of regions of varying strength levels, it can change how the specimen deforms. This affects where and when strain localization and necking occurs, which again influences global load-bearing capacities. This is why each local heat treatment is only compared to its specific reference of equal geometry.

5.3 Effect of local heat treatments

5.3.1 Cross welds

In the following section, the effect of the local heat treatment by cross welds is evaluated. Firstly, the specimens with cross welds and without PWHT are discussed based on their properties compared to the reference specimen and each other. Then, the effect of the PWHT on the cross welded specimens is considered. Bar plots are used to illustrate the improvements and differences in mechanical properties, and possible explanations are discussed.

Mechanical properties

All cross welded specimens yields at lower stress compared to the reference, as seen from the grey bars in Figure 5.2. The specimens with the slowest welding speeds (18 mm/s and 20 mm/s) suffers from a larger reduction in yield strength than the specimens with cross weld speeds of 22 mm/s and 26 mm/s. This indicates that the heat generated during the cross welding process causes an reduction of the yield strength whereas slower welding speeds implies a larger decrease. This could be because slower speeds increases the exposure time of critical temperatures and results in a larger HAZ and possibly lower strength in this region. This is evident from the hardness profiles in Figure 4.4 in Section 4.1.2 where the extent of the HAZ from welding speed 14 mm/s is significantly larger than for the welding speed of 18 mm/s. Thus, the larger area of softening can be an explanation of the lower yield strength values observed for the slower cross weld speeds.

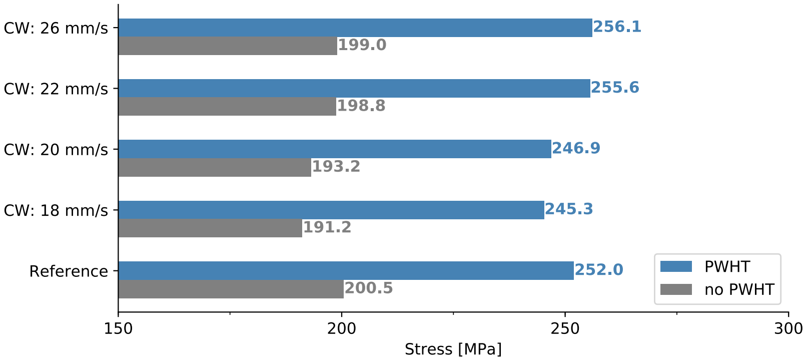

Figure 5.2: *Comparison of yield strength for specimens for cross welds of different welding speeds with or without post weld heat treatment (PWHT).*

Although the cross welds generally have a negative effect on the yield strength, the ultimate tensile strength is increased for all cross welded specimens compared to the reference specimen. The grey bars in Figure 5.3 shows the ultimate tensile strength of the different cross welded specimens. The ultimate tensile strength varies from 259.6 MPa to 264.4 MPa corresponding to an increase of 10-15 MPa. This is considered a significant strength increase that shows the effect of cross welds. This is likely due to the reinforcement by the increased welds beads of the cross welds and the aging reaction (reprecipitation) close to the cross welds causing a strength increase in this area. This indicates that the overall strengthening effect of the cross welds predominates the softening in the HAZ made by the cross welds when it comes to the ultimate tensile strength. All the specimens with cross welds experience larger elongation during tensile testing, as seen from Figure 5.4. This means increased ductility due to the cross welds since the specimens' resistance to plastic deformation is increased.

The two faster weld speeds (22 mm/s and 26 mm/s) show better properties than the lower weld speeds, both with regards to yield and ultimate tensile strength. All cross welded specimens experienced a large increase in percent elongation at

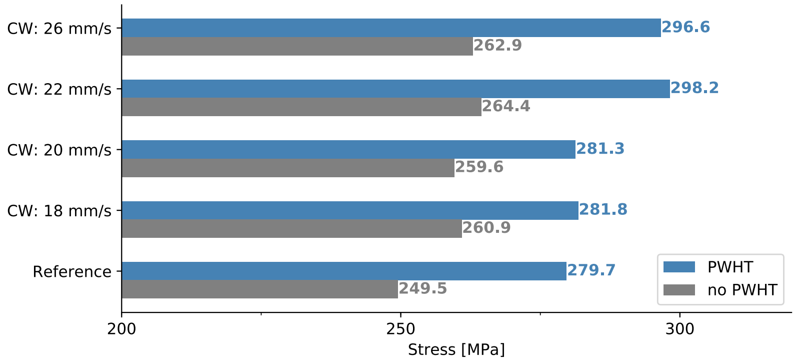

Figure 5.3: *Comparison of ultimate tensile strength for specimens for cross welds of different welding speeds with or without post weld heat treatment (PWHT).*

fracture, as seen in Figure 5.4, but the impact of welding speed is not clear regarding elongation. The increase in elongation can likely be explained by the same effects that resulted in lower yield strength values, where the softening effects of the cross welds' heat affected zones allow for more deformation prior to fracture.

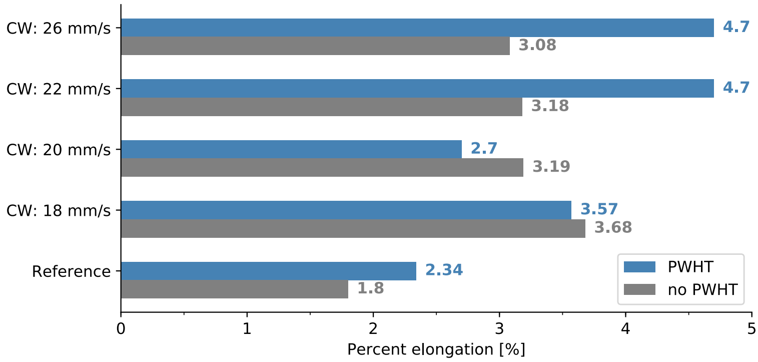

Figure 5.4: *Comparison of percent elongation at fracture for specimens for cross welds of different welding speeds with or without post weld heat treatment (PWHT).*

The PWHT generally resulted in a significant increase in both yield and ultimate tensile strength for all specimens, with an increase in yield strength of more than 50 MPa and a 20-30 MPa increase in ultimate tensile strength compared to similar specimens without PWHT. This is evident from Figure 5.2 and 5.3. To account for the effects of the cross weld, the further comparison is done with respect to the reference specimen with PWHT. The specimens with 18 and 20 mm/s cross weld speeds experience a decrease, while the specimens with welding speed of 22 and 26 mm/s show a slight increase compared to the reference. However, not by more than a few MPas. This indicates that the effect of PWHT in combination with cross welds is minor when it comes to yield strength, but has a slightly better effect on the specimens with faster cross weld speeds. It is evident from Figures 5.3 and 5.4 that the specimens faster cross weld speeds of 22 and 26 mm/s with PWHT experienced the best overall improvement of properties with an increase of more than 15 MPa in UTS and almost 2.4 % in elongation when compared to the PWHT reference specimen.

Strain localization and fracture location

The cross welds change the geometry of the HAZ, as shown in Figure 5.5 where the extent of the HAZ and the lowest level HAZ is illustrated. This causes strain to localize in several different locations during tensile testing for the different specimens, as shown in the Figures showing strain evolution and crack propagation in Section 4.2. All specimens without PWHT fractured along the minimum strength level in the HAZ where the crack initiated in the center of the specimen, e.g., between the two cross welds on one side of the weld (see point B in Figure 5.5). For some of the specimens subjected to the PWHT, the fracture location shifted out of the HAZ and fractured along the cross weld tips about 35 mm from the center of the joining weld (point A Figure 5.5). This indicates that the reinforcement of the cross welds is increased by the additional post weld heat treatment which reprecipitation of β''-particles in a region close to the cross weld beads similar to whats observed in the hardness profile of the joining GMA welds, e.g., Figure 4.3 in Section 4.1.2. This causes strengthening of a larger area and results in different deformation behavior. The strain does not localize in the HAZ between the cross welds, but rather in the HAZ at the tips of the cross welds, which now is the points of lowest strength in the specimen.

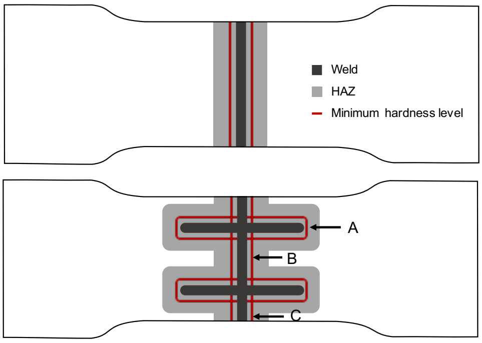

Figure 5.5: Illustration showing the HAZ and minimum hardness level due to the welds, where A, B, and C indicate locations of crack initiation.

The reduction in strength at the tips of the cross welds is less for the faster cross weld speeds of 22 mm/s and 26 mm/s, while still gaining the strength increase. This results in increased global strength compared to the specimens with slower cross weld speeds. The specimen with cross weld speed of 22 mm/s obtained the best mechanical properties. For this specimen strain localizes in several locations, including the cross weld tips and the HAZ as shown in Figure 4.14b in Chapter 4. The first crack occurred at the tip of one cross weld (point A in Figure 5.5), just before a new crack appeared the HAZ of the joining weld at the edge of the specimen (point C in Figure 5.5). This indicates that the strength of these regions is similar, causing competing regions for strain localization. This postpones necking and promotes more plastic deformation before the maximum stress level is reached, thus resulting in higher elongation at fracture and increased strength. The large improvements in both strength and ductility confirm the predictions by H. G. Fjær [31], and show that cross welds could be a valid method for improving mechanical properties of welds. However, these results are based on tensile loading perpendicular to the weld for extruded sheets with one specific specimen geometry. The results are promising, but more extensive testing and optimization of the method is required before this could be applied to industrial applications.

5.3.2 Longitudinal laser

The results from the tensile testing and hardness measurements of the specimens with longitudinal laser treatment are discussed in this section. As the tensile specimens were tested without extensometer, the elastic properties of the specimens could be inaccurate. Thus, the ultimate tensile strength is the main results used for comparison of the effect of laser treatment. The relative differences of the stress strain curves gives an indication of the behavior of the specimens. Figure 5.6 shows the comparison of the ultimate tensile strength of the laser treated specimens. The specimens with PWHT showed increased strength and lower elongation at fracture compared to specimen without PWHT. Compared to the reference specimen with PWHT, all laser treated specimens experienced decreased ultimate tensile strength, indicating that the laser had a negative effect when combined with PWHT. It is therefore concluded that the PWHT does not benefit from the laser treatments presented in this thesis.

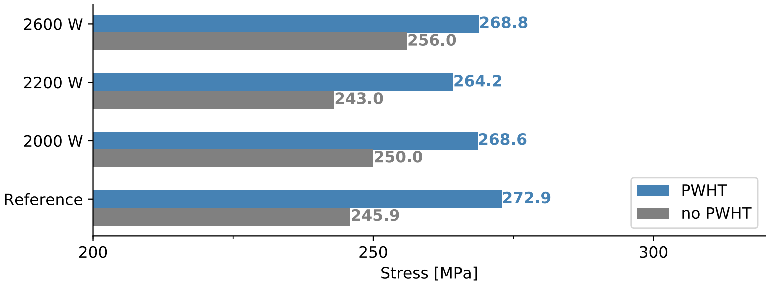

Figure 5.6: *Comparison of ultimate tensile strength of specimens with longitudinal laser.*

The strength results regarding laser powers are not consistent, as the 2000 W and 2600 W treatments show increased strength, while the specimens with 2200 W laser treatment experience a reduction. The specimen with 2600 W laser treatment exhibited the largest increase of 9 MPa in UTS, along with increased elongation. Melting due to the laser is observed on the surface of these specimens to a varying extent, and the increased strength and elongation indicates that the heat has been sufficient to change the global properties of the specimen. For one of the 2600 W specimens, the fracture did not occur in the HAZ of the weld (8.5 mm from weld center), but further out at approximately 14 mm from weld center. This corresponds to the position of the lasers' HAZ, which is observable from the hardness profile in Figure 4.22 in Section 4.3.1. The other specimen with the same laser treatment fractured in the weld HAZ 8.5 mm from weld center, but obtained similar strength level. Since this specimen fractured at a higher strength than the specimens without laser, this could indicate that the minimum strength level of the weld HAZ is increased by the laser, or that the changes in the HAZ cause strain to distribute and localize in a different manner which increases the global strength of the specimen.

5.3.3 Laser pattern

It is evident from the hardness plots in Figure 4.27 in Section 4.4.1 that the laser treatment has changed the hardness profile of the weld cross-section close to the surfaces. The measurements along the center of the thickness seem fairly unaffected by the laser lines, which indicates that the heat of the laser can only change the microstructure close to the surfaces. The large drop in hardness along the lower surface of the sheet is likely because these laser lines were added after the laser on the upper surface, which means the temperature of the sheet was higher initially.

The PWHT of the specimen with laser pattern was conducted independently from the rest of the post weld heat treatments, and the hardness profiles presented in Figure 4.27 show a significant drop in base material hardness of almost 20 HV. This decrease is larger than the other post weld heat treated specimens which indicates that the temperature was likely higher than 220°C. During the heat treatment, there was a discrepancy between the thermocouples attached to the specimen and the temperature indicator of the oven. The correspondence of these temperature indicators was tested before the heat treatment was conducted with a difference of only a few degrees Celsius. However, during the actual treatment of the specimens, this discrepancy increased to about 15 °C. The thermocouple temperature was held at the treatment temperature of 220 °C, but due to the large decrease in hardness, the actual temperature was likely higher. Despite the wrong temperature, the PWHT did cause reprecipitation of strengthening particles and increased the hardness of the HAZ, but not to the same extent as for the other specimens in this report.

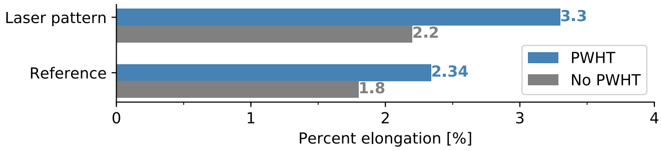

Figure 5.7: *Percent elongation at fracture for specimens with laser pattern compared to reference specimens.*

The strength level of the laser treated specimen PWHT remains similar to the reference, while the ductility is significantly improved as seen from Figure 5.8 and 5.7. This improvement in ductility could be due to the altered HAZ geometry causing the strain to distribute differently. This is evident from the strain fields during deformation in Figure 4.29b in Section 4.4, since the laser pattern is visible as darker regions at the DIC strain field. The ductility is increased for the specimen without PWHT as well, but not to the same extent, indicating that the effect of the laser pattern has not been large enough to alter the HAZ geometry significantly. The strain field in Figure 4.29a in Section 4.4 confirms this. However, a small strength increase is observed. It is not clear whether this is due to differences in weld quality or caused by the laser pattern. Based on the results from the tensile test of specimens with laser lines in the HAZ at 8.5 mm from weld center, the laser power might have been too low to cause significant changes. A laser power of 2600 W rather than 2000 W, could have a larger impact on strength and ductility and be beneficial in such a laser pattern.

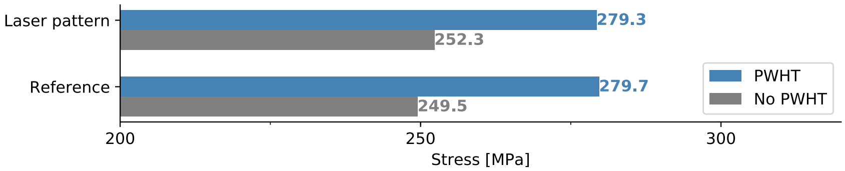

Figure 5.8: *Ultimate tensile strength for specimens with laser pattern compared to reference specimens.*

5.4 Predictions and simulations

5.4.1 Validation of peak temperature predictions and thermal cycles

Figure 4.31 shows a comparison between the measured thermal cycle during welding and the predicted cycle of equal input parameters. The predictions with the Rosenthals medium thick plate solution are considered to represent the thermal cycles adequately, with an accurate representation of the heating rate and peak temperatures. The measured temperature indicates a slower cooling rate immediately after the peak temperature is reached, which is due to the simplifying assumptions of the Rosenthals medium thick plate solution. The predicted thermal cycles with an efficiency factor of η=0.7 were chosen based on the conformity of measured and predicted peak temperatures, as shown in Figure 4.32 in Section 4.5.1. This correspondence is illustrated in Figure 5.9, which shows the predicted peak temperatures plotted against the measured data. It is evident that there is a good correlation between the predicted and measured data, which is why the predictions were considered adequate for the predictive analysis using the NaMo model in this thesis.

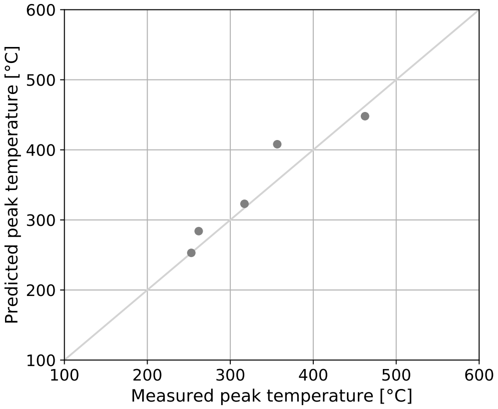

Figure 5.9: *Comparison between the measured and predicted (η=0.7) peak temperatures during welding. The grey line shows where measured temperatures are equal predicted temperatures.*

Figure 2.13b in Chapter 2 shows that the lowest hardness level of welded 6082-T6 corresponds to a peak temperature of approximately 430°C. Hardness profiles are plotted together with the predicted peak temperature values in Figure 5.10 for data observed in this thesis. As seen from Figure 5.10, the lowest hardness level is observed at a distance of 8-9 mm from weld center which corresponds to peak temperatures of 448 and 408°C respectively. Similar correspondence between the peak temperatures and hardness profiles was observed by Myhr and Grong [36].

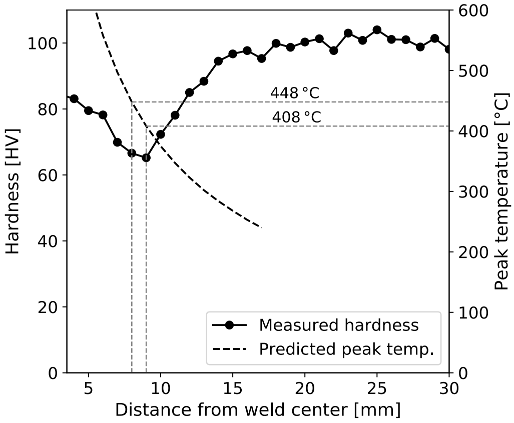

Figure 5.10: *Measured hardness profile from welding process and corresponding peak temperatures.*

5.4.2 Evaluation of hardness predictions

The results of the NaMo simulations presented in Figures 4.33a, 4.33b, 4.34a and 4.34b in Section 4.5 show that the extent of the HAZ is predicted precisely by NaMo in all cases. In general, all the predicted hardness profiles follows the measured profiles accurately, regarding the position of increased and decreased, although the hardness drops are overestimated.

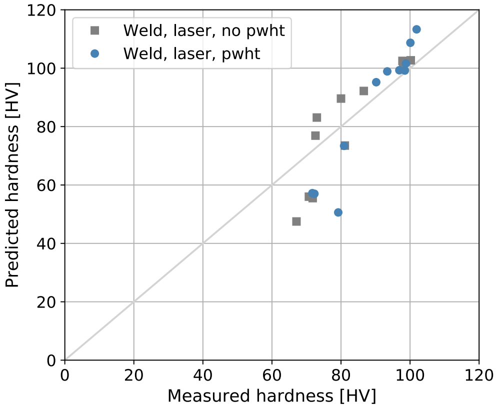

Figure 5.11: *Comparison between the measured and predicted hardness of welded specimens with 2200 W longitudinal laser. The grey line shows where measured temperatures are equal predicted temperatures.*

Figure 5.11 show the correspondence between the predicted and measured data for weld and laser treatment, and the results are satisfactory both with and without the PWHT. The higher hardness values are generally well described by the NaMo model, while the lower hardness is underestimated compared to the measurements. However, conclusions can not be drawn on whether the model overestimated the aging response and the drop in hardness due to the weld thermal cycle, based on this single comparison to empirical data. More experimental data is needed in order to investigate this deviation of the predicted hardness in this region.

The simulations in Figure 4.34 in Section 4.5 show that the hardness just beneath the laser at 8.5 mm from weld center should experience a large increase as the laser temperature theoretically reached a value of 538°C. This temperature is predicted by Rosenthal medium thick plate solution at a position 0.8 mm beneath the 2200 W longitudinal laser. This temperature level is high enough to reverse precipitates, thus increase the aging potential in this region. However, measurements indicate that this effect is not achieved. An explanation to this is that the temperature never reached this predicted peak level. Due to the point heat source assumption, the laser power is concentrated at one single point in the predictions. Since the spot size of the laser was 3 mm, this assumption does not hold for predicted values close to the heat source. This suggests that the actual peak temperature was lower than the predicted value at this exact point, and thus not high enough to facilitate the aging predicted by the simulations.

6 Conclusion

6.1 Summary and conclusions

The post weld heat treatment increased the ultimate tensile strength by 25-30 MPa, while the local heat treatments generally improved ductility. However, large strength improvements are observed as well. The most relevant results from the mechanical testing are presented below:

1. All specimens with cross welds show increased ultimate tensile strength of more than 10 MPa, and fracture strains are increased by over 70%. However, the yield strength values are not improved. The two faster welding speeds of 22 mm/s and 26 mm/s show the most significant improvements in both strength and ductility. Additionally, these cross weld speeds resulted in the largest effect of the PWHT, where the ultimate tensile strength is 47 MPa higher than the untreated reference specimen, while the fracture strain is increased by over 120%. The combination of PWHT and cross weld speed of 22 mm/s causes competing regions for strain localization. Thus several locations of necking occur, which results in significant strength and ductility improvements.
2. For the specimens with longitudinal laser in HAZ, the highest laser power of 2600W showed the largest improvements in mechanical properties. The ultimate tensile strength was increased by 9 MPa, and the fracture location shifted out of the lowest level HAZ for one of the specimens, which indicates competing zones of deformation. However, further investigation of this method is required to conclude on the effects.
3. The 2000 W laser pattern has a positive effect on ductility, but the laser power is likely too weak to give any significant strengthening effect, although a small increase in tensile strength of 3 MPa is observed. The PWHT did not benefit from the laser pattern regarding strength, but ductility was significantly improved by the combination of laser pattern and PWHT.

There is an excellent agreement between peak temperatures predicted by Rosenthal medium thick plate solutions and thermocouple measurements. Simulations using the predictive model NaMo slightly overestimated the reduction in the lowest level HAZ and the strength increase close to the fusion zone. The model predicts the extent of the HAZ precisely and the overall correspondence with measured data regarding the shape of the hardness profile is very good.

6.2 Recommendations for further work

The method of applying cross welds to improve global strength properties should be explored further to find the optimal weld speed and pattern of the cross welds. Results of this present report indicate an optimal cross weld speed of 22 mm/s. The PWHT increases the strength contributions of the cross welds enough to shift the strain localization out of the HAZ, but this does not occur for the specimen without PWHT. It is therefore recommended to decrease the spacing between the cross welds. Hardness measurements over the cross-section of a cross weld are suggested to determine the extent of the increased strength around the cross weld due to aging, and the optimized spacing between cross welds can be found.

The specimens with 2600 W laser showed the most promising results with increased strength and elongation, while the samples with lower laser power did not show significant improvements. The effects of different laser power, as well as the position and pattern of the laser treatment, should be further tested to find an optimal treatment for a significant increase in mechanical properties. One suggestion would be to apply the laser treatment of 2600 W in the same pattern as presented in this thesis. Predictive models, e.g., the NaMo model as presented in this thesis, could be used to simulate the hardness response to different heat treatments and find an optimized heat input for local heat treatment. Finite element analysis is recommended for finding an optimized pattern of this local heat treatment.

Other heating technologies could be considered, as well. The possibility of using induction for the local heat treatment of welded specimens should be explored. A local post weld heat treatment of stainless steel welds using a robot and an induction heating system are studied by E. Boudreault et al. [42]. The heat distribution is controlled by moving an induction pancake coil in a specific pattern, where the finite element simulations are used to calculate the optimal path for the coil. Although this method is optimized for reducing residual stresses in stainless steel welds, the analogy should be applicable for the local heating of the Al-Mg-Si welds to facilitate reprecipitation of strengthening particles, similar to the local heat treatments in this present thesis.

References

[1] J. R. Davis, *Aluminum and aluminum alloys*, ser. ASM specialty handbook. Materials Park, OH: ASM International, 1993.

[2] W. Miller, L. Zhuang, J. Bottema, A. Wittebrood, P. De Smet, A. Haszler, and A. Vieregge, “Recent development in aluminium alloys for the automotive industry,” *Materials Science and Engineering: A*, vol. 280, no. 1, pp. 37–49, 2000.

[3] K. Stanford, “Lightweighting boosts vehicle safety,” *Aluminium International Today*, vol. 30, no. 6, pp. 10–12, 2017.

[4] C. Marioara, S. Andersen, J. Jansen, and H. Zandbergen, “Atomic model for GP-zones in a 6082 Al-Mg-Si system,” *Acta materialia*, vol. 49, no. 2, pp. 321–328, 2001.

[5] P. K. Saha, *Aluminum extrusion technology.* Materials Park, OH: Asm International, 2000.

[6] G. Edwards, K. Stiller, G. Dunlop, and M. Couper, “The precipitation sequence in al–mg–si alloys,” *Acta materialia*, vol. 46, no. 11, pp. 3893–3904, 1998.

[7] Ø. Grong, *Metallurgical modelling of welding*, 2nd ed., ser. Materials modelling series. London: Institute of Materials, 1997.

[8] V. Malin, “Study of metallurgical phenomena in the HAZ of 6061-T6 aluminum welded joints,” *Welding Journal-Including Welding Research Supplement*, vol. 74, no. 9, pp. 305–318, 1995.

[9] O. R. Myhr and Ø. Grong, “Novel modelling approach to optimisation of welding conditions and heat treatment schedules for age hardening Al alloys,” *Science and Technology of Welding and Joining*, vol. 14, no. 4, pp. 321–332, 2009.

[10] S. B. Gjertsen, “Mechanical properties after welding and post weld heat treatment of a 6082 aluminium alloy,” Master’s thesis, Norwegian University of Science and Technology, Trondheim, 2018.

[11] A. Hamarsnes, “Mechanical properties of welded 6082-T6 aluminium alloy with transverse cross welds,” 2018, unpublished thesis.

[12] Ø. Grong, *Sveisemetallurgi.* Trondheim: Universitetet i Trondheim, Norges tekniske høgskole, Metallurgisk institutt, 1990.

[13] F. M. Mazzolani, *Aluminium Structural Design*, ser. International Centre for Mechanical Sciences, Courses and Lectures,. Vienna: Springer Vienna, 2003, vol. 443.

[14] D. S. Thompson, "Metallurgical factors affecting high strength aluminum alloy production," *Metallurgical Transactions A*, vol. 6, no. 4, pp. 671–683, 1975.

[15] B. Rinderer, "The metallurgy of homogenisation," *Materials Science Forum*, vol. 693, pp. 264–275, 2011.

[16] S. K. Fjeldbo, Y. Li, K. Marthinsen, and T. Furu, "Through-process sensitivity analysis on the effect of process variables on strength in extruded al–mg–si alloys," *Journal of Materials Processing Tech.*, vol. 212, no. 1, pp. 171–180, 2012.

[17] R. Lumley, *Fundamentals of aluminium metallurgy: production, processing and applications*, ser. Woodhead Publishing Series in Metals and Surface Engineering. Oxford: Woodhead, 2011.

[18] S. Pogatscher, H. Antrekowitsch, H. Leitner, T. Ebner, and P. Uggowitzer, "Mechanisms controlling the artificial aging of al–mg–si alloys," *Acta Materialia*, vol. 59, no. 9, pp. 3352–3363, 2011.

[19] Ø. Grong, "Recent advances in solid-state joining of aluminum," *Welding journal*, vol. 91, no. 1, pp. 26–33, 2012.

[20] W. D. Callister, *Materials science and engineering*, 9th ed. Hoboken, N.J: Wiley, 2015.

[21] W. F. Hosford, *Mechanical behavior of materials.* Cambridge University Press, New York, 2005.

[22] O. R. Myhr, Ø. Grong, and K. O. Pedersen, "A combined precipitation, yield strength, and work hardening model for Al-Mg-Si alloys," *Metallurgical and Materials Transactions A: Physical Metallurgy and Materials Science*, vol. 41, no. 9, pp. 2276–2289, 2010.

[23] O. R. Myhr, "Combined precipitation, yield strength and work hardening models for Al-Mg-Si alloys," Jun. 2017, unpublished.

[24] G. Gottstein, *Physical foundations of materials science.* Berlin: Springer, 2004.

[25] H. Guo, J. Hu, and H. Tsai, "Formation of weld crater in gmaw of aluminum alloys," *International Journal of Heat and Mass Transfer*, vol. 52, no. 23, pp. 5533–5546, 2009.

[26] G. Mathers, *The welding of aluminium and its alloys*, ser. Woodhead Publishing Series in Welding and Other Joining Technologies. Cambridge, England: Woodhead publishing, 2002.

[27] O. R. Myhr and Ø. Grong, "Dimensionless maps for heat flow analyses in fusion welding," *Acta metallurgica et materialia*, vol. 38, no. 3, pp. 449–460, 1990.

[28] N. Christensen, V. Davies, and K. Gjermundsen, “Distribution of temperatures in arc welding,” *Brit. Weld. J.*, vol. 12, no. 2, pp. 54–75, 1965.

[29] O. R. Myhr, Ø. Grong, H. G. Fjær, and C. D. Marioara, “Modelling of the microstructure and strength evolution in Al-Mg-Si alloys during multistage thermal processing,” *Acta Materialia*, vol. 52, no. 17, pp. 4997–5008, 2004.

[30] H. G. Fjær, “Improved strength of a welded aluminium structure by a modification of the haz geometry,” 2017, unpublished.

[31] H. G. Fjær, “A suggestion for an «armoured weld»,” 2018, unpublished.

[32] W. Koechner, *Solid-State Laser Engineering*, ser. Springer Series in Optical Sciences. New York, NY: Springer New York, 2006, vol. 1.

[33] M. Merklein, W. Böhm, and M. Lechner, “Tailoring Material Properties of Aluminum by Local Laser Heat Treatment,” *Physics Procedia*, vol. 39, pp. 232–239, 2012.

[34] M. Geiger, M. Merklein, and U. Vogt, “Aluminum tailored heat treated blanks,” *Production Engineering*, vol. 3, no. 4-5, pp. 401–410, 2009.

[35] O. R. Myhr and Ø. Grong, “Process modelling applied to 6082-T6 aluminium weldments—I. Reaction kinetics,” *Acta Metallurgica et Materialia*, vol. 39, no. 11, pp. 2693–2702, 1991.

[36] O. R. Myhr and Ø. Grong, “Process modelling applied to 6082-T6 aluminium weldments—II. Applications of model,” *Acta Metallurgica et Materialia*, vol. 39, no. 11, pp. 2703–2708, 1991.

[37] T. Furu and O. R. Myhr, “Method for the optimisation of product properties and production costs of industrial processes,” US Patent 20 150 178 656, 2015.

[38] O. R. Myhr, R. Østhus, J. Søreide, and T. Furu, “A Novel Methodology for Optimization of Properties, Costs and Sustainability of Aluminium Extrusions,” *Materials Science Forum*, vol. 877, pp. 625–632, 2016.

[39] O. R. Myhr and Ø. Grong, “Modelling of non-isothermal transformations in alloys containing a particle distribution,” *Acta Materialia*, vol. 48, no. 7, pp. 1605–1615, 2000.

[40] O. R. Myhr, Ø. Grong, and S. J. Andersen, “Modelling of the age hardening behavior of Al-Mg–Si alloys,” *Acta Materialia*, vol. c, pp. 65–75, 2001.

[41] O. R. Myhr, Ø. Grong, and C. Schäfer, “An Extended Age-Hardening Model for Al-Mg-Si Alloys Incorporating the Room-Temperature Storage and Cold Deformation Process Stages,” *Metallurgical and Materials Transactions A: Physical Metallurgy and Materials Science*, vol. 46, no. 12, pp. 6018–6039, 2015.

[42] E. Boudreault, B. Hazel, J. Côté, and S. Godin, “In situ post-weld heat treatment on martensitic stainless steel turbine runners using a robotic induction heating process to control temperature distribution,” *IOP Conference Series: Earth and Environmental Science*, vol. 22, 2014.

Appendices

A Finite element analysis (FEA) results

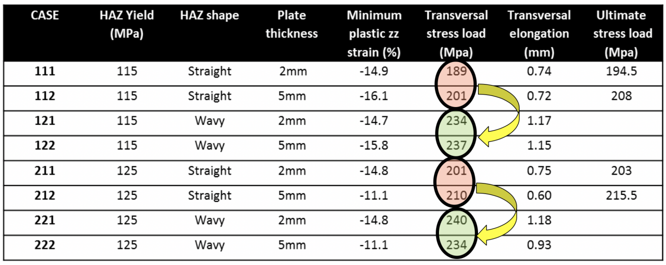

CASE	HAZ Yield (MPa)	HAZ shape	Plate thickness	Minimum plastic zz strain (%)	Transversal stress load (Mpa)	Transversal elongation (mm)	Ultimate stress load (Mpa)
111	115	Straight	2mm	-14.9	189	0.74	194.5
112	115	Straight	5mm	-16.1	201	0.72	208
121	115	Wavy	2mm	-14.7	234	1.17	
122	115	Wavy	5mm	-15.8	237	1.15	
211	125	Straight	2mm	-14.8	201	0.75	203
212	125	Straight	5mm	-11.1	210	0.60	215.5
221	125	Wavy	2mm	-14.8	240	1.18	
222	125	Wavy	5mm	-11.1	234	0.93	

Figure A.1: *Table summarizing the results from finite element simulataions of straight and bulged HAZ shape, where stress and elongation are presented for two different plate thicknesses and HAZ yield strength values. Copied from [31]*

B Material certificate

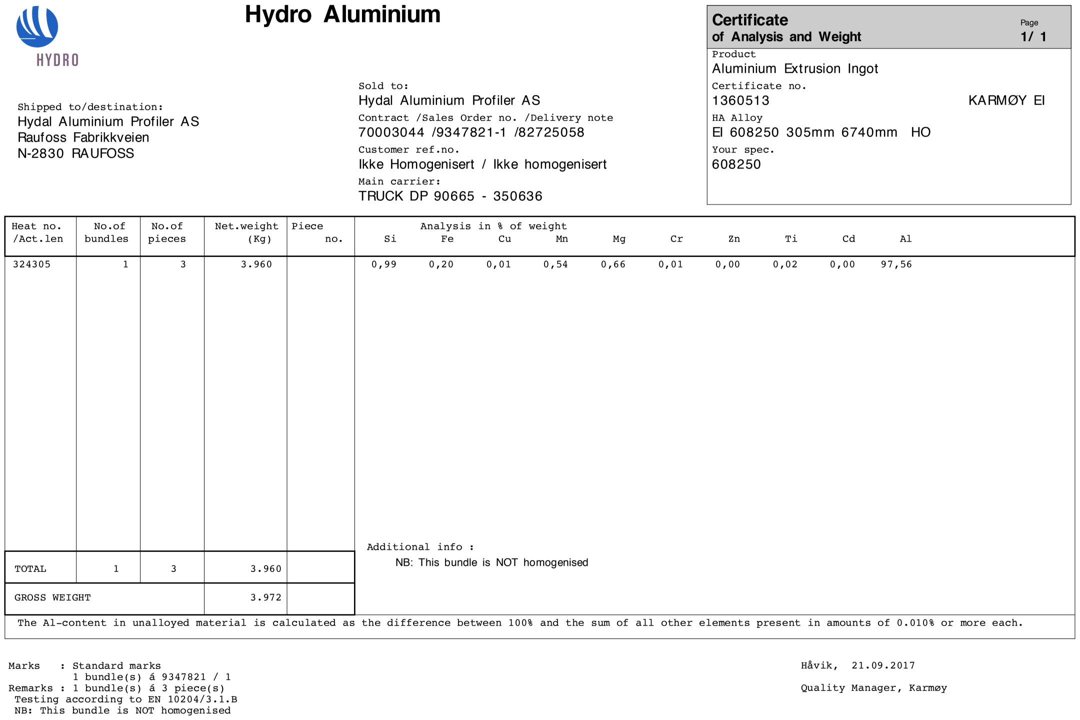

Hydro Aluminium

Certificate
of Analysis and Weight

Page
1/ 1

Product
Aluminium Extrusion Ingot
Certificate no.
1360513 KARMØY EI
HA Alloy
EI 608250 305mm 6740mm HO
Your spec.
608250

Shipped to/destination:
Hydal Aluminium Profiler AS
Raufoss Fabrikkveien
N-2830 RAUFOSS

Sold to:
Hydal Aluminium Profiler AS
Contract /Sales Order no. /Delivery note
70003044 /9347821-1 /82725058
Customer ref.no.
Ikke Homogenisert / Ikke homogenisert
Main carrier:
TRUCK DP 90665 - 350636

Heat no. /Act.len	No.of bundles	No.of pieces	Net.weight (Kg)	Piece no.	Analysis in % of weight Si	Fe	Cu	Mn	Mg	Cr	Zn	Ti	Cd	Al
324305	1	3	3.960		0,99	0,20	0,01	0,54	0,66	0,01	0,00	0,02	0,00	97,56
TOTAL	1	3	3.960											
GROSS WEIGHT			3.972											

Additional info :
NB: This bundle is NOT homogenised

The Al-content in unalloyed material is calculated as the difference between 100% and the sum of all other elements present in amounts of 0.010% or more each.

Marks : Standard marks
1 bundle(s) á 9347821 / 1
Remarks : 1 bundle(s) á 3 piece(s)
Testing according to EN 10204/3.1.B
NB: This bundle is NOT homogenised

Håvik, 21.09.2017
Quality Manager, Karmøy

Figure B.1: *Material certificate*

C Tensile test specimens

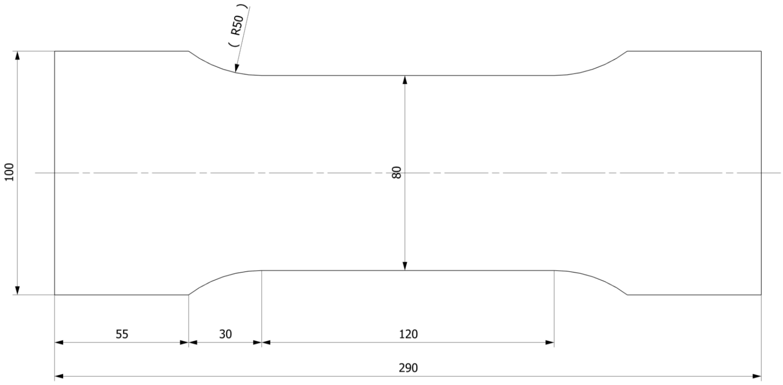
(R50)
100
80
55
30
120
290

Figure C.1: *Specimen for DIC tensile testing of sheets with cross welds.*

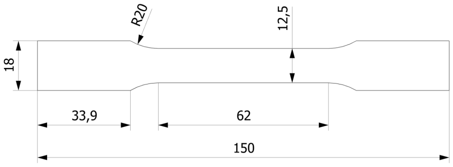
R20
12,5
18
33,9
62
150

Figure C.2: *Specimen for tensile test of sheets with longitudinal laser in minimum level HAZ.*

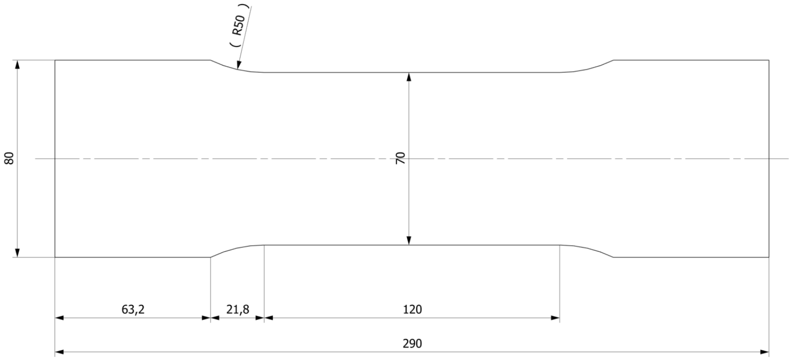
(R50)
80
70
63,2
21,8
120
290

Figure C.3: *Specimen for DIC tensile testing of sheets laser pattern.*

D NaMo inputs

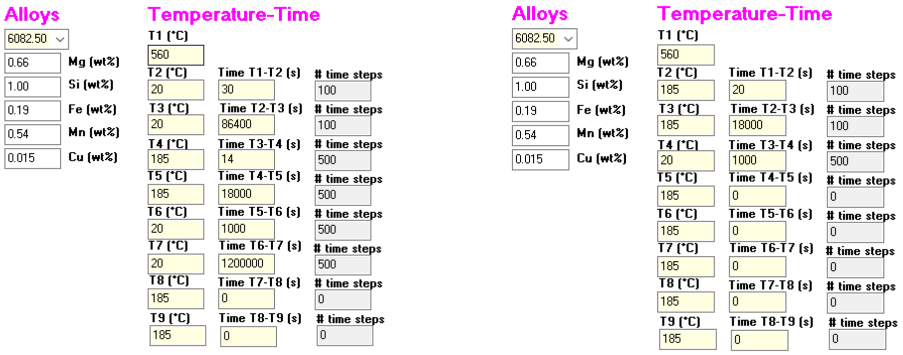

(a)

Alloys

6082.50	
0.66	Mg (wt%)
1.00	Si (wt%)
0.19	Fe (wt%)
0.54	Mn (wt%)
0.015	Cu (wt%)

Temperature-Time

T1 (°C)	560				
T2 (°C)	20	Time T1-T2 (s)	30	# time steps	100
T3 (°C)	20	Time T2-T3 (s)	86400	# time steps	100
T4 (°C)	185	Time T3-T4 (s)	14	# time steps	500
T5 (°C)	185	Time T4-T5 (s)	18000	# time steps	500
T6 (°C)	20	Time T5-T6 (s)	1000	# time steps	500
T7 (°C)	20	Time T6-T7 (s)	1200000	# time steps	500
T8 (°C)	185	Time T7-T8 (s)	0	# time steps	0
T9 (°C)	185	Time T8-T9 (s)	0	# time steps	0

(b)

Alloys

6082.50	
0.66	Mg (wt%)
1.00	Si (wt%)
0.19	Fe (wt%)
0.54	Mn (wt%)
0.015	Cu (wt%)

Temperature-Time

T1 (°C)	560				
T2 (°C)	185	Time T1-T2 (s)	20	# time steps	100
T3 (°C)	185	Time T2-T3 (s)	18000	# time steps	100
T4 (°C)	20	Time T3-T4 (s)	1000	# time steps	500
T5 (°C)	185	Time T4-T5 (s)	0	# time steps	0
T6 (°C)	185	Time T5-T6 (s)	0	# time steps	0
T7 (°C)	185	Time T6-T7 (s)	0	# time steps	0
T8 (°C)	185	Time T7-T8 (s)	0	# time steps	0
T9 (°C)	185	Time T8-T9 (s)	0	# time steps	0

Figure D.1: *NaMo input for hardness predictions (a) before simplification and (b) after simplification of the thermal history.*

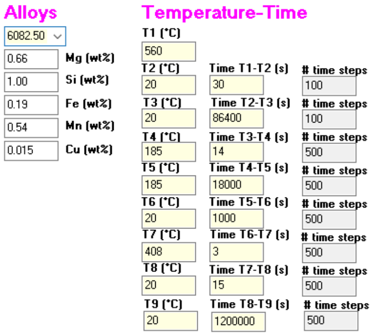

Alloys

6082.50	
0.66	Mg (wt%)
1.00	Si (wt%)
0.19	Fe (wt%)
0.54	Mn (wt%)
0.015	Cu (wt%)

Temperature-Time

T1 (°C)	560				
T2 (°C)	20	Time T1-T2 (s)	30	# time steps	100
T3 (°C)	20	Time T2-T3 (s)	86400	# time steps	100
T4 (°C)	185	Time T3-T4 (s)	14	# time steps	500
T5 (°C)	185	Time T4-T5 (s)	18000	# time steps	500
T6 (°C)	20	Time T5-T6 (s)	1000	# time steps	500
T7 (°C)	408	Time T6-T7 (s)	3	# time steps	500
T8 (°C)	20	Time T7-T8 (s)	15	# time steps	500
T9 (°C)	20	Time T8-T9 (s)	1200000	# time steps	500

Figure D.2: *NaMo input for hardness predictions of welded sheet 9 mm from weld center at the upper surface (through thickness depth = 0).*

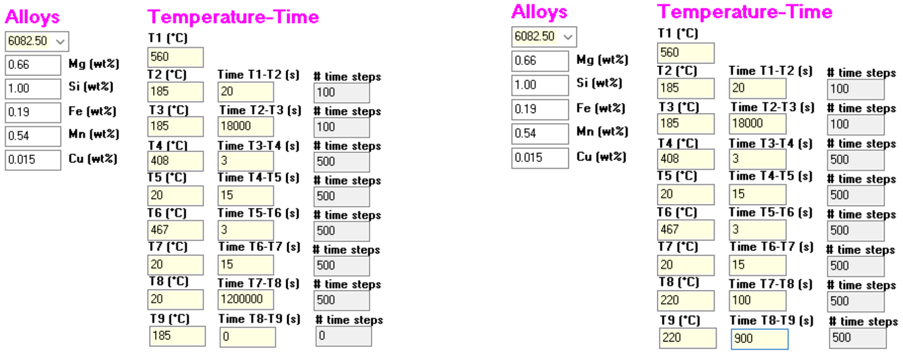

(a)

6082.50

Mg (wt%): 0.66
Si (wt%): 1.00
Fe (wt%): 0.19
Mn (wt%): 0.54
Cu (wt%): 0.015

T1 (°C): 560
T2 (°C): 185 | Time T1-T2 (s): 20 | # time steps: 100
T3 (°C): 185 | Time T2-T3 (s): 18000 | # time steps: 100
T4 (°C): 408 | Time T3-T4 (s): 3 | # time steps: 500
T5 (°C): 20 | Time T4-T5 (s): 15 | # time steps: 500
T6 (°C): 467 | Time T5-T6 (s): 3 | # time steps: 500
T7 (°C): 20 | Time T6-T7 (s): 15 | # time steps: 500
T8 (°C): 20 | Time T7-T8 (s): 1200000 | # time steps: 500
T9 (°C): 185 | Time T8-T9 (s): 0 | # time steps: 0

(b)

6082.50

Mg (wt%): 0.66
Si (wt%): 1.00
Fe (wt%): 0.19
Mn (wt%): 0.54
Cu (wt%): 0.015

T1 (°C): 560
T2 (°C): 185 | Time T1-T2 (s): 20 | # time steps: 100
T3 (°C): 185 | Time T2-T3 (s): 18000 | # time steps: 100
T4 (°C): 408 | Time T3-T4 (s): 3 | # time steps: 500
T5 (°C): 20 | Time T4-T5 (s): 15 | # time steps: 500
T6 (°C): 467 | Time T5-T6 (s): 3 | # time steps: 500
T7 (°C): 20 | Time T6-T7 (s): 15 | # time steps: 500
T8 (°C): 220 | Time T7-T8 (s): 100 | # time steps: 500
T9 (°C): 220 | Time T8-T9 (s): 900 | # time steps: 500

Figure D.3: *NaMo input for hardness predictions of welded sheet with 2200 W laser 9 mm from weld center 0.8 mm from the upper surface (through thickness depth = 0.8), where (a) is without PWHT and (b) is with PWHT of 220° C/15min.*

E Temperature calculations and corresponding NaMo output

Table 7: *Predicted temperatures for NaMo inputs.*

Distance from weld center [mm]	Laser peak temp. [°C]	Weld peak temp. [°C]	Predicted hardness with PWHT [HV]	Predicted hardness without PWHT [HV]
4	153	755	113.3	89.6
5	177	639	108.7	83.1
6	215	558	101.6	76.9
6.5	247	526	86.7	63
7	292	497	50.6	47.5
7.5	364	471	52	53.6
8	467	448	57.2	55.5
8.5	538	428	108.6	79.8
9	467	408	57	56
9.5	364	391	67.9	68.3
10	292	375	73.4	73.5
10.5	247	360	80.4	79.6
12	177	323	95.2	92.2
14	137	284	98.9	101.2
16	114	253	99.2	102.5
25	-	-	99.3	102.7

F Stress-strain plot of all DIC tensile specimens

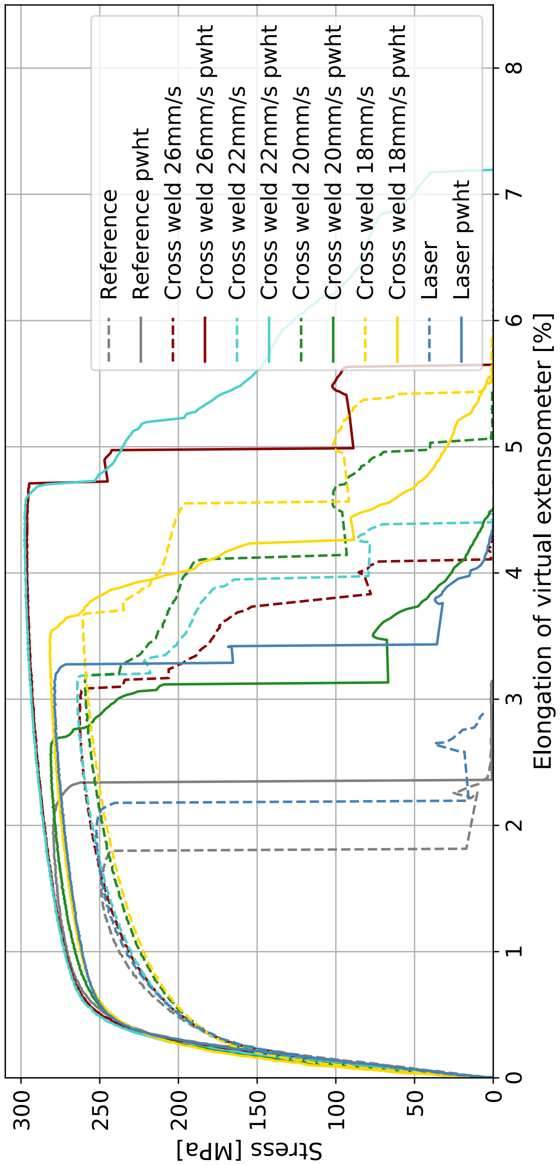

Figure F.1: *Stress-strain curves of all specimens tested with DIC.*

G Fractured DIC tensile specimens

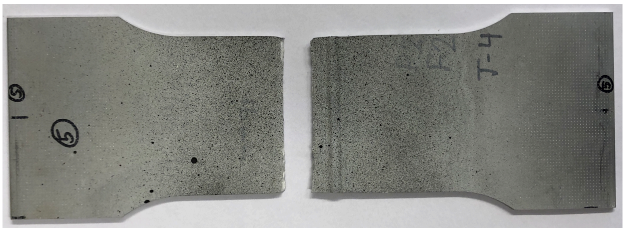

Figure G.1: *Fractured reference specimen, without PWHT.*

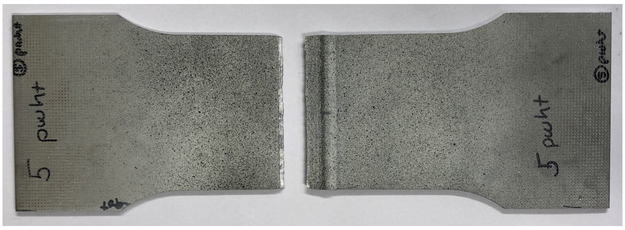

Figure G.2: *Fractured reference specimen, with PWHT.*

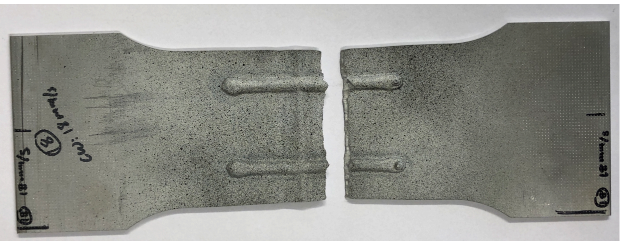

Figure G.3: *Fractured specimen with cross weld speed 18 mm/s, without PWHT.*

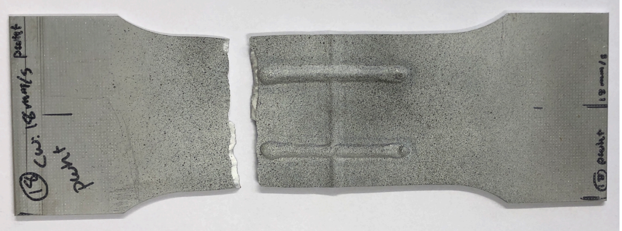

Figure G.4: *Fractured specimen with cross weld speed 18 mm/s, with PWHT.*

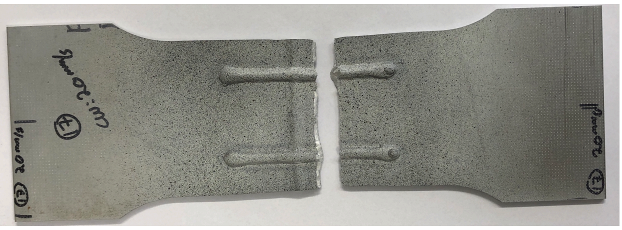

Figure G.5: *Fractured specimen with cross weld speed 20 mm/s, without PWHT.*

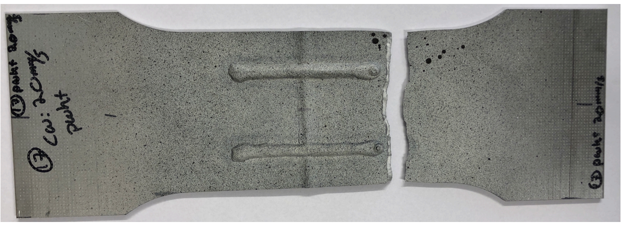

Figure G.6: *Fractured specimen with cross weld speed 20 mm/s, with PWHT.*

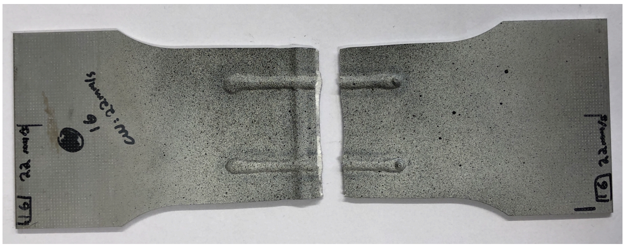

Figure G.7: *Fractured specimen with cross weld speed 22 mm/s, without PWHT.*

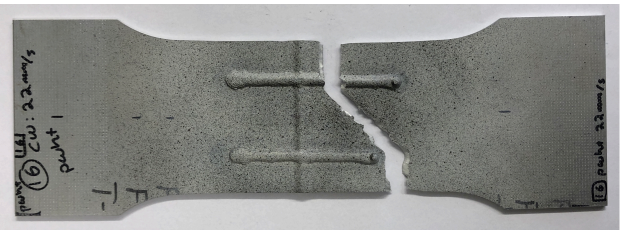

Figure G.8: *Fractured specimen with cross weld speed 22 mm/s, with PWHT.*

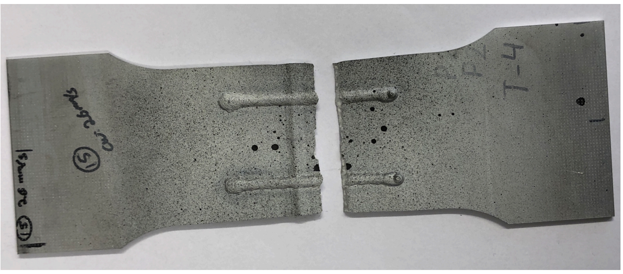
cw: 26mm/s
15
T-4

Figure G.9: Fractured specimen with cross weld speed 26 mm/s, without PWHT.

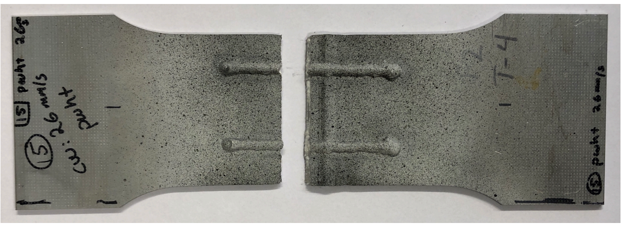
cw: 26 mm/s
pwht
15
T-4
pwht 26 mm/s

Figure G.10: Fractured specimen with cross weld speed 26 mm/s, with PWHT.

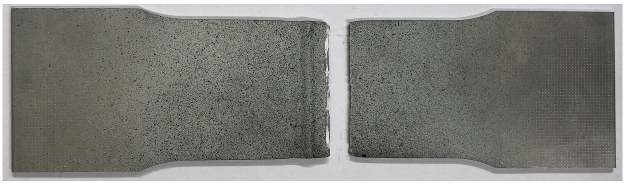

Figure G.11: Fractured specimen with laser pattern, without PWHT.

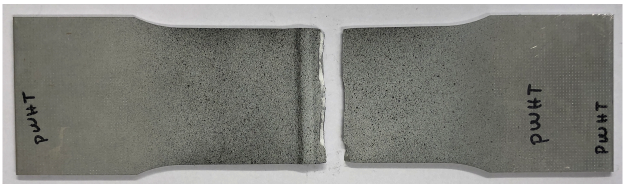
PWHT
PWHT
PWHT

Figure G.12: Fractured specimen with laser pattern, with PWHT.

H Longitudinal laser in HAZ

H.1 Tensile results

Table 8: *Tensile properties from tensile testing of samples with laser in HAZ. Yield strength are excluded for the samples with laser as they were tested without extensometers.*

Description	Yield strength [MPa]	Ultimate tensile strength [MPa]
Reference, 1	171.3	245.4
Reference, 2	173.5	245.3
Reference, 3	174.8	246.0
Reference, 4	175.9	247.0
Reference, P1, pwht	230.5	273.4
Reference, P2, pwht	229.1	273.4
Reference, P3, pwht	227.4	272.3
Reference, P4, pwht	227.0	272.4
2000 W, 1	-	250.1
2000 W, 2	-	249.9
2000 W, 1, pwht	-	268.5
2000 W, 2, pwht	-	268.7
2200 W, 1	-	243.3
2200 W, 2	-	242.7
2200 W, 1, pwht	-	264.9
2200 W, 2, pwht	-	263.4
2600 W, 1	-	255.8
2600 W, 2	-	256.1
2600 W, 1, pwht	-	268.2
2600 W, 2, pwht	-	269.3

H.2 Fractured tensile specimens

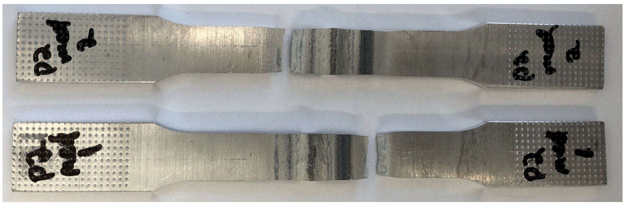

Figure H.1: *Fractured specimens with longitudinal laser of 2600 W, without PWHT.*

I Risk assessment

NTNU	Hazardous activity identification process	Prepared by	Number	Date
HSE		HSE section	HMSRV2601E	09.01.2013
		Approved by		Replaces
		The Rector		01.12.2006

Unit: Department of Mechanical and Industrial Engineering **Date: 01.02.2018**

Line manager:

Participants in the identification process (including their function)**: Geir Ringen (supervisor), Anne Hamarsnes (student)**

Short description of the main activity/main process: Master project for student Anne Hamarsnes. Characterization of welded aluminium with manipulation of HAZ geometry.

Is the project work purely theoretical? (YES/NO): NEI *Answer "YES" implies that supervisor is assured that no activities requiring risk assessment are involved in the work. If YES, briefly describe the activities below. The risk assessment form need not be filled out.*

Signatures: *Responsible supervisor:* Geir Ringen *Student:* Anne Hamarsnes

ID nr.	Activity/process	Responsible person	Existing documentation	Existing safety measures	Laws, regulations etc.	Comment
1	Metallography lab	AH	Room Card	Room card, first aid kit, eye shower		
1a	Usage of grinding and polishing machines	AH	Room Card	First aid kit, gloves		
1b	Usage of chemicals	AH	Room Card	First aid kit, eye shower, gloves, safety goggles		
1c	Usage of cutting machine	AH	Room Card	First aid kit, eye shower, gloves, safety goggles		
2	Lab for tensile testing	Lab technician	Machine´s user manual	Safety goggles		
2a	Use of tensile test machine	Lab technician	Machine´s user manual	Safety goggles		
2b	Use of deburring tools	AH	Machine´s user manual	Safety goggles, first aid kit.		

NTNU	Risk assessment	Prepared by	Number	Date
		HSE section	HMSRV2603E	04.02.2011
		Approved by		Replaces
HSE/KS		The Rector		01.12.2006

Unit: Department of Mechanical and Industrial Engineering **Date: 01.02.2018**

Line manager:

Participants in the identification process (including their function)**: Geir Ringen (supervirsor), Anne Hamarsnes (student)**

Short description of the main activity/main process: Master project for student Anne Hamarsnes. Characterization of welded aluminium with manipulation of HAZ geometry.

Signatures: *Responsible supervisor:* Geir Ringen *Student:* Anne Hamarsnes

Activity from the identification process form	**Potential undesirable incident/strain**	**Likelihood:**	**Consequence:**			**Risk Value (human)**	**Comments/status Suggested measures**
		Likelihood (1-5)	Human (A-E)	Environment (A-E)	Economy/ material (A-E)		
Usage of grinding and polishing machines	Friction burns on fingers/hands	4	A	A	B	A4	Wear gloves. Locate first aid kit. User manual.
	Fire	2	C	C	D	C2	Locate fire extinguisher, fire blankets and exits.
Usage of chemicals	Exposure to chemical fumes	3	A	C	B	A3	Training and planning. First aid kit. Use of fume hood.
	Chemical burns on skin	3	B	A	A	B3	Training and planning. User manual. Use of fume hood.
	Chemicals in eyes	2	B	A	B	B2	Training and planning. User manual. Use of fume hood.
Usage of cutting machine	Smaller cutting injury	4	A	A	B	A4	Training and planning. User manual. Locate first aid kit.
	Severe cutting injury	1	D	A	A	D1	Training and planning. User manual. Locate first aid kit.
	Fire	2	C	C	D	C2	Locate fire extinguisher, fire blankets and exits.
Use of deburring tools	Smaller cutting injury	3	A	A	A	A3	Wear gloves, first aid kit.

Likelihood, e.g.:

1. *Minimal*
2. *Low*
3. *Medium*
4. *High*
5. *Very high*

Consequence, e.g.:

- *A. Safe*
- *B. Relatively safe*
- *C. Dangerous*
- *D. Critical*
- *E. Very critical*

Risk value (each one to be estimated separately):
Human = Likelihood x Human Consequence
Environmental = Likelihood x Environmental consequence
Financial/material = Likelihood x Consequence for Economy/materiel

NTNU	Risk assessment	Prepared by	Number	Date
		HSE section	HMSRV2603E	04.02.2011
		Approved by		Replaces
HSE/KS		The Rector		01.12.2006

Potential undesirable incident/strain

Identify possible incidents and conditions that may lead to situations that pose a hazard to people, the environment and any materiel/equipment involved.

Criteria for the assessment of likelihood and consequence in relation to fieldwork

Each activity is assessed according to a worst-case scenario. Likelihood and consequence are to be assessed separately for each potential undesirable incident. Before starting on the quantification, the participants should agree what they understand by the assessment criteria:

Likelihood

Minimal 1	Low 2	Medium 3	High 4	Very high 5
Once every 50 years or less	Once every 10 years or less	Once a year or less	Once a month or less	Once a week

Consequence

Grading	Human	Environment	Financial/material
E **Very critical**	May produce fatality/ies	Very prolonged, non-reversible damage	Shutdown of work >1 year.
D **Critical**	Permanent injury, may produce serious serious health damage/sickness	Prolonged damage. Long recovery time.	Shutdown of work 0.5-1 year.
C **Dangerous**	Serious personal injury	Minor damage. Long recovery time	Shutdown of work < 1 month
B **Relatively safe**	Injury that requires medical treatment	Minor damage. Short recovery time	Shutdown of work < 1week
A **Safe**	Injury that requires first aid	Insignificant damage. Short recovery time	Shutdown of work < 1day

The unit makes its own decision as to whether opting to fill in or not consequences for economy/materiel, for example if the unit is going to use particularly valuable equipment. It is up to the individual unit to choose the assessment criteria for this column.

Risk = Likelihood x Consequence

Please calculate the risk value for “Human”, “Environment” and, if chosen, “Economy/materiel”, separately.

About the column ”Comments/status, suggested preventative and corrective measures”:

Measures can impact on both likelihood and consequences. Prioritise measures that can prevent the incident from occurring; in other words, likelihood-reducing measures are to be prioritised above greater emergency preparedness, i.e. consequence-reducing measures.

NTNU	Risk matrix	prepared by	Number	Date
		HSE Section	HMSRV2604	8 March 2010
		approved by	Page	Replaces
HSE/KS		Rector	4 of 4	9 February 2010

MATRIX FOR RISK ASSESSMENTS at NTNU

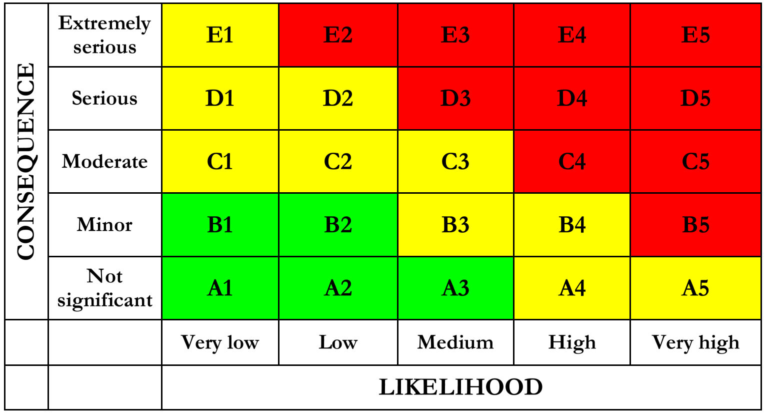

CONSEQUENCE						
	Extremely serious	🟨 E1	🟥 E2	🟥 E3	🟥 E4	🟥 E5
	Serious	🟨 D1	🟨 D2	🟥 D3	🟥 D4	🟥 D5
	Moderate	🟨 C1	🟨 C2	🟨 C3	🟥 C4	🟥 C5
	Minor	🟩 B1	🟩 B2	🟨 B3	🟨 B4	🟥 B5
	Not significant	🟩 A1	🟩 A2	🟩 A3	🟨 A4	🟨 A5
		Very low	Low	Medium	High	Very high
		LIKELIHOOD				

Principle for acceptance criteria. Explanation of the colours used in the risk matrix.

Colour		Description
Red	🟥	Unacceptable risk. Measures must be taken to reduce the risk.
Yellow	🟨	Assessment range. Measures must be considered.
Green	🟩	Acceptable risk Measures can be considered based on other considerations.